RL894

FULL-WAVE CHARACTERIZATION OF HIGH-FREQUENCY NONPLANAR INTERCONNECTS

Andrew George Engel, Jr.

January, 1993

RL-894 = RL-894

FULL-WAVE CHARACTERIZATION OF HIGH-FREQUENCY NONPLANAR INTERCONNECTS

by

Andrew George Engel, Jr.

A dissertation submitted in partial fulfillment
of the requirements for the degree of
Doctor of Philosophy
(Electrical Engineering)
in The University of Michigan
1993

Doctoral Committee:

Associate Professor Linda P. B. Katehi, Chairperson
Associate Professor Eduard Harabetian
Associate Professor Gabriel M. Rebeiz
Associate Professor John L. Volakis
Research Scientist Jack R. East

To Dawn,
to my parents,
and, of course, to the Twins, for winning it twice

ACKNOWLEDGEMENTS

First and foremost, I thank my advisor, Professor Linda Katehi, for her support during my career as a graduate student. Her insight, ideas, expertise, enthusiasm, and encouragement are reflected throughout this work. I am also grateful for her material contributions, such as my research assistantship, the numerous opportunities to attend and participate in conferences, and the use of a desktop workstation.

I also thank the rest of my Doctoral Committee for their review of this dissertation, participation in my Final Examination, and constructive suggestions.

At one time or another, many of my fellow students have contributed to this work. I especially thank Dr. Norman L. VandenBerg for the many discussions, the contribution of several invaluable software tools (including the plotting utilities which were used extensively in this work), and for the support and friendship over the years. I thank Dr. William P. Harokopus and Mr. Daniel C. Ross, who have been great friends as well as technical contributors. In addition, Dr. Nihad I. Dib, Dr. George V. Eleftheriades, Dr. T. Emilie Vandeventer and Mr. Thomas M. Weller all made significant contributions. I am also indebted to many others, too numerous to mention, for the many technical (and some not-so-technical) conversations.

The responsible organizations and people must be recognized for their financial support. The University of Michigan's Department of Electrical Engineering and Computer Science granted a Benton fellowship for my first year in graduate school. Professors G. I. Haddad and Linda Katehi provided a three-year fellowship from the Army Research Office under the University Research Initiative (URI) program, contract number DAAL03-87-K-0007. Support for the final 18 months of my graduate student career (as well as secondary support throughout the entire five-and-a-half years) came from the Army Research Office, the NASA Center for Space Terahertz Technology, and the Radiation Laboratory. Additional support came in the form of a student grant from the International Society for Hybrid Microelectronics Educational Foundation.

Last, but certainly not least, I thank my parents for their continuous encouragement and support since February 9, 1961; and Ms. Dawn R. Von Thurn for her faith in me, her wonderful influence on my life, and for everything else since February 3, 1990.

TABLE OF CONTENTS

CHAPTER

LIST OF FIGURES

Figure

LIST OF TABLES

Table

LIST OF APPENDICES

Appendix

CHAPTER I

INTRODUCTION

1.1 Motivation and Objectives

As monolithic and VLSI circuits are designed to perform multiple functions at heightened frequencies, increased complexity through the use of nonplanar interconnects is inevitable. Although there exist some common nonplanar circuit elements, such as air-bridges, via holes and transitions, interconnects have generally been considered planar due to the proliferation of microstrip and coplanar waveguide. Not to be ignored is the nonplanar nature of a wide variety of monolithic and VLSI interconnects, and a broad class of structures (of which the planar interconnects are a subset) can be defined. These *nonplanar interconnects* include *strip-ridge* structures, which consist of conducting strips suspended by dielectric ridges and/or a substrate above a ground plane in close proximity to other conductors on other ridges and localized superstrates, and *monolithic dielectric waveguides*, which are dielectric strips either raised above or embedded in a substrate. The following examples show how nonplanar interconnects are utilized over a wide range of frequencies and applications.

Consider first the range of 100 GHz–2.0 THz, where progress has been made in the development of narrow-beam, high-resolution antennas which are essential for intelligent computer control guidance, command systems for space applications, and sensors which operate in optically opaque media [73, 76]. Since these systems require that the generated

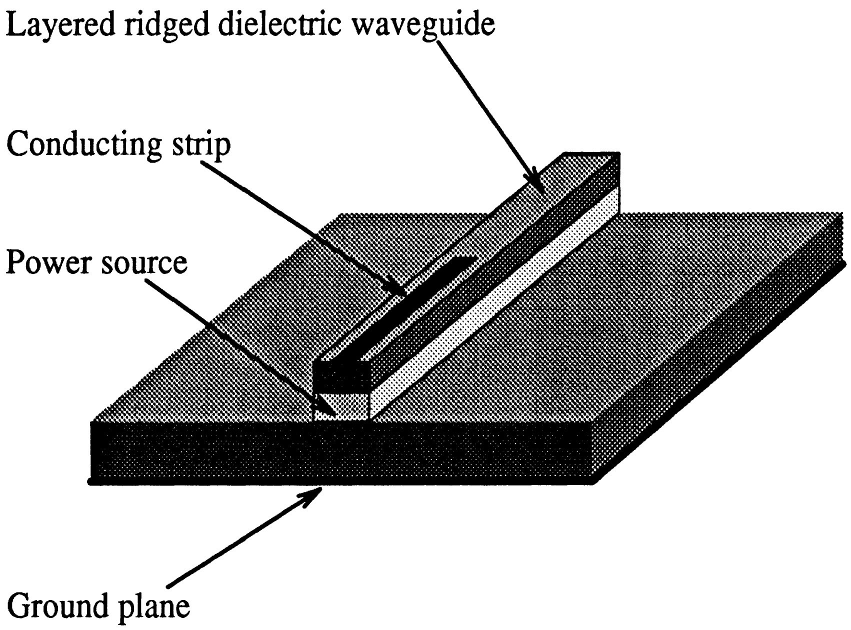

Figure 1.1: A transition from a power source to a ridged dielectric waveguide. The ridge is shown with two layers.

THz-power be guided to the antenna front-end through complex feeding networks, the design and construction of low-loss monolithic transmission lines are critical. There are two typical approaches for the design of these transmission lines. The first approach extends the use of planar conductors in monolithic millimeter-wave technology to higher frequencies. However, the excellent performance of planar circuit elements such as loads, transitions, junctions at frequencies up to 100 GHz is not easily duplicated at higher frequencies because ohmic and radiation losses become unacceptably high. The second approach, which extends optical techniques to lower frequencies, is hindered by three factors. First, many optical materials are incompatible with the semiconducting materials which are needed for active devices. Second, phenomena such as nonlinear wave characteristics dominate optical waves but are not present at terahertz frequencies. Third, certain phenomena, such as radiation and electromagnetic coupling, are ignored at optical frequencies but are not negligible at terahertz frequencies. In view of these limitations, an alternate approach is appropriate, and one suitable transmission line is the monolithic dielectric waveguide proposed in chapter V of this thesis (figure 1.1). This type of waveguide, although it links coplanar integrated circuit elements, consists of a dielectric ridge on or embedded in a substrate and therefore belongs in the class of nonplanar interconnects. When these waveguides are integrated with power sources (such as active devices), or when these waveguides are used to form passive circuit components (such as a power combiner), short lengths of conductor can be used to minimize radiation. A transition between a power source and a dielectric waveguide has the configuration displayed in figure 1.1.

Nonplanar interconnects also have applications in high-speed VLSI structures which carry narrow pulses with small rise times. When increased packing density without increased crosstalk is a concern, structures such as a microstrip on a finite substrate and ground plane or coupled multilevel microstrip with an inhomogeneous intermediate layer might be employed (figure 1.2). Since the microwave and millimeter-wave frequency components of the pulses can be significant, accurate high-frequency characterization of the interconnects is essential if dispersion effects on pulse propagation are to be correctly predicted.

Another use for nonplanar interconnects is in integrated traveling-wave optical modulator structures, where microwave signals are used to control the permittivity of optical waveguides [70] and nonplanar variations of these structures can lead to improved performance. A possible integrated modulator structure (figure 1.3) consists of an intrinsic GaAs guiding layer for the optical signal; p- and n-$\mathrm{Al}_{0.025}\mathrm{Ga}_{0.975}\mathrm{As}$ layers for top and bottom cladding; a 250μm n^+-GaAs substrate; and two conducting strips which guide the microwave signal. The modulator bandwidth depends inversely on the difference between the optical and microwave indices of refraction [3], but the microwave index of refraction

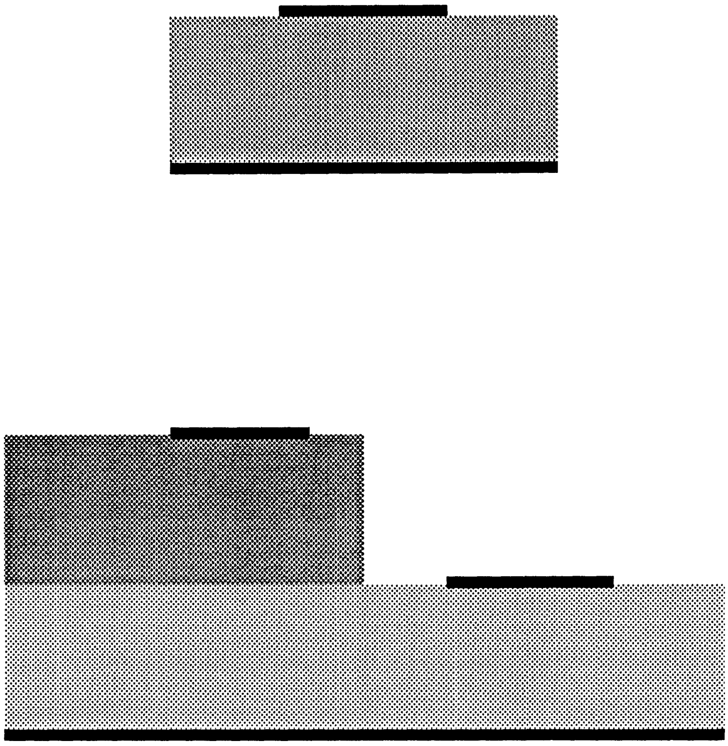

Figure 1.2: Shown in cross-section, two examples of nonplanar interconnects: microstrip on a finite width substrate and ground plane, and coupled multilevel microstrip with an inhomogeneous intermediate layer.

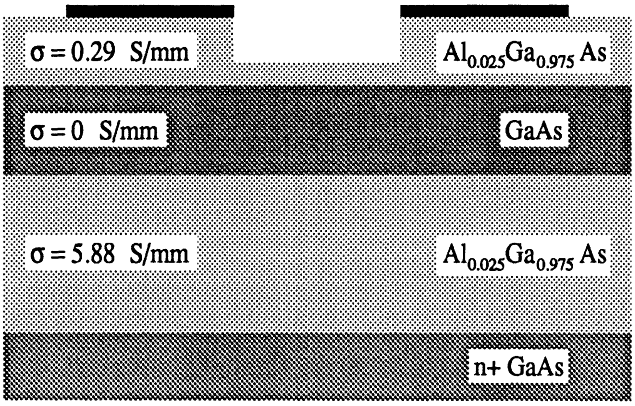

Figure 1.3: Cross-section of an electro-optic modulator with an etched groove to improve the bandwidth.

is considerably larger than the optical index of refraction. The bandwidth can be widened by adding the etched groove between the two electrodes, thereby decreasing the microwave index of refraction and also minimizing the attenuation in the microwave signal [87]. A related structure is an interferometric light modulator which has an optical waveguide integrated beneath each conducting strip and an etched groove between the two optical waveguides to suppress the optical coupling [33].

The above examples provide motivation for the introduction, development and application of techniques which are able to characterize a multitude of nonplanar interconnect structures. With these methods, the need for empirical characterization can be greatly reduced, resulting in substantial reductions in fabrication costs and design cycle time. Given these incentives, the objectives of this thesis are:

- the creation of a comprehensive set of accurate and general methods for the analysis and design of nonplanar interconnects, and
- the use of these tools in the investigation of a wide variety of these interconnects,

which might be employed anywhere in the microwave–THz frequency ranges on monolithic and VLSI structures.

The first step toward the accomplishment of these goals is the choice of an appropriate approach to the analysis.

1.2 Techniques for the Analysis of Nonplanar Interconnects

Methods for the characterization of interconnects belong to one of three categories: quasi-static, dispersion or full-wave models. Quasi-static models assume TEM propagation, and solve the time-invariant Maxwell's equations. Dispersion models provide information about the frequency variation of the electrical performance with a semi-empirical approach. Full-wave models solve the time-varying Maxwell equations, and rigorously account for high-frequency effects such as electromagnetic coupling and propagation losses. The quasi-static and dispersion models are only valid at low frequencies or over limited frequency ranges. As the complexity and operating frequency of interconnect structures increase, the fields become increasingly non-TEM and full-wave analysis is required for wideband, accurate characterization. Furthermore, since both strip-ridge structures and dielectric waveguides are considered in this work, two analysis methods are required.

Since the early 1980's, the characterization of strip-ridge structures has been addressed several times. Quasi-static methods such as an integral equation formulation [66, 67] and the rectangular boundary division method [89, 90] have considered an open microstrip on a finite dielectric and shielded microstrip near a chip edge, respectively. In addition, full-wave mode-matching techniques have been applied to the analysis of a conducting strip on a ridge with a layered substrate (microslab^{TM} waveguide) [91, 92], transverse wave propagation on FET structures [38], and a variety of quasi-planar structures involving conductors on finite-width substrates [75]. The method of lines [74, 87] has been employed to characterize electro-optic modulator structures, a microstrip on a ridged substrate, a microstrip near a chip edge, microslab, and slow-wave MIS microstrip/coplanar lines with inhomogeneously doped substrates. In addition, finite element [61], finite difference [8, 14], transmission-line matrix (TLM) [39], boundary integral [65] and generalized integral equation (GIE) [79] techniques can be applied to structures with conducting strips in the presence of inhomogeneous dielectrics.

Although strip-ridge structures have not been typically characterized by the class of integral equation techniques which solve directly for the currents on the conducting strips, nonplanar analysis based on these techniques is possible. In this work, a hybrid full-wave integral equation-mode matching (IEMM) technique is developed and applied to the study of nonplanar strip-ridge structures in both the frequency and time domains. The IEMM method is distinct from other combinations of integral equation and mode matching techniques in that the mode matching is performed in the longitudinal plane. Mode matching associated with integral equation methods is typically along one transverse direction, as in the case when structures have layered substrates and superstrates and there is a simple one-to-one correspondence between the modes in each layer [19, 45, 78], or in a transverse plane, as in the case when a current source in a waveguide or cavity is adjacent to another waveguide with a different cross-section [23].

The primary reason for developing the IEMM technique is that it analytically decouples a structure into two parts, namely, the conducting strips and the supporting dielectrics. The integral equation portion of the formulation solves the conductor problem, and the mode matching portion solves the dielectric problem. The decoupling of the two problems is exploited when the IEMM method is applied to a class of three-dimensional structures in which the uniformity of the dielectric support structure along the longitudinal direction is preserved. When these structures are analyzed, the integral equation is efficiently solved with the method of moments for any configuration of conductors on a given dielectric support structure.

Another advantage of the IEMM method is that it requires discretization of only the conducting strips, and this area is usually a small portion of the structure which is characterized. In contrast, many of the other applicable techniques need to discretize the entire volume of the structure for three-dimensional implementation.

Suitable analysis techniques for dielectric waveguides include the aforementioned finite element, finite difference, TLM, boundary integral, GIE and mode matching techniques. Because the latter method is a natural complement to the IEMM method and very few modes are necessary for accurate results, an appropriate version of the mode matching method [17, 52, 68] is chosen for this work.

1.3 Overview

The analysis techniques have been selected and must now be developed and implemented so that various nonplanar interconnects can be characterized.

The IEMM and mode matching methods are detailed in chapter II. The integral equation, the determination of the Green's function with mode matching, and the solution of the integral equation with the method of moments and Galerkin's technique are discussed with respect to three-dimensional structures. The two-dimensional IEMM method and the associated propagation constant and characteristic impedance calculations are then described, and the mode matching method is briefly reviewed.

Chapter III addresses the translation of the theory into a set of functional computer-aided modeling tools. The first part of the chapter is a discussion of computational considerations, including the solution of the transcendental equations associated with the IEMM and mode matching methods, matrix storage and inversion, the calculation of the propagation constants of two-dimensional structures, convergence issues, and the efficiency of the code. The second part, validation, contains examples of the many comparisons with independent experimental and numerical results which ensured that accurate results were obtained.

Strip-ridge structures for use in VLSI applications and monolithic microwave, millimeter-wave, and sub-millimeter-wave integrated circuits are characterized in the frequency and time domains with the two-dimensional IEMM method in chapter IV. The specific time domain analysis technique, which uses the IEMM results for the propagation constant and characteristic impedance as functions of frequency, is first described. The bulk of the chapter is then devoted to studies of coupled microstrip on ridges, coupled microstrip with an etched groove, microstrip with finite substrate and ground plane, coupled multilevel microstrip with a finite intermediate dielectric layer, and an electro-optic modulator structure with an etched groove.

In chapter V, low-loss monolithic sub-millimeter-wave and terahertz dielectric waveguides are proposed and characterized. The waveguides are constructed from materials and structures which are available in monolithic technology so that the use of the waveguides in integrated circuits is possible. The dimensions of the waveguides are on the order of a fraction of a guided wavelength, so that the new structures can be used not only as transmission lines, but also as passive circuit elements such as inductors and couplers. Since the proposed structures have properties similar to conventional microstrip elements, the structures are able to provide both low-loss feeding networks and highly efficient radiating elements for arrays. Examples are designed for specific frequencies in the 0.3–2.0 THz and 0.1–0.3 THz ranges, and propagation in each of the waveguides is characterized over relevant frequency ranges by applying the mode-matching technique.

An important aspect of integrating the new waveguides in monolithic circuits is the design of an active device-to-waveguide transition, and this topic is addressed in chapter VI. The transition consists of a short length of conductor on top of the ridged waveguide (figure 1.1) in a shielded environment. The shielding structure can support higher order modes which have significant effects on the electrical performance. While these modes are considered, a simple method for determining the transition's circuit model from IEMM and mode matching results is implemented and the electrical performance of the transition is studied as frequency and conductor width are varied.

The concluding remarks in chapter VII summarize the major results and suggest extensions of this work. The IEMM method is evaluated; both the advantages of the technique and possibilities for further improvement are discussed. Consideration is given to several nonplanar interconnect structures which were not addressed in this work, but are nonetheless useful and easily characterized by the IEMM method. Finally, the further development of layered ridged dielectric waveguides and strip-ridge structures for use in sub-millimeter-wave and terahertz monolithic integrated circuits is previewed.

CHAPTER II

THE INTEGRAL EQUATION-MODE MATCHING AND MODE MATCHING TECHNIQUES

The methods which have been chosen to characterize nonplanar interconnects in this thesis are the IEMM and mode matching techniques. The IEMM method was developed especially for the analysis of strip-ridge structures, and its complexity warrants the in-depth description provided in the majority of this chapter. Conversely, the well-established mode matching method is applied to the modeling of dielectric waveguides, and the last section of this chapter is sufficient for a brief review.

2.1 Introduction to the IEMM Technique

Unlike other integral equation techniques, the IEMM technique is appropriate for the analysis of a broad class of nonplanar structures. The hybrid nature of the IEMM technique allows for the analytical decoupling of a nonplanar structure into its constituent conducting strips and supporting dielectrics. Independent of the geometry of the conducting strips, the dielectric support structure is taken into account by the mode matching portion of the technique, and the integral equation can then be efficiently solved with the method of moments for any configuration of conductors.

The IEMM technique is applied by modeling a general structure as a rectangular cavity with conducting strips supported by dielectric layers which contain rectangular step-inhomogeneities (figure 2.1). The cavity is further divided into adjacent sections of layered parallel-plate waveguide. A spatial domain electric field integral equation is solved with a Green's function-method of moments approach. The Green's function is determined by replacing the conducting strips with a point source of current and employing mode-matching to apply the boundary conditions at the interfaces between the parallel-plate waveguides. The boundary conditions on the conducting strips are enforced by solving the electric field integral equation with the method of moments. In this chapter, the system of equations which stems from the application of the method of moments to the integral equation is derived with the three-dimensional IEMM method. The two-dimensional IEMM method and the associated propagation constant and characteristic impedance calculations are also described. Subsequent chapters discuss how the results from the two-dimensional IEMM method are used to determine the coupling coefficient and pulse propagation characteristics, and how the currents on a discontinuous conducting strip in a three-dimensional structure are used to determine the associated circuit model.

2.2 The General Structure

The general structure contains rectangular step inhomogeneities and conducting strips, as shown in figure 2.1. The structure is uniform along the z-axis for $0 < z < c$. The outer walls of the cavity are perfect electric conductors. Along the y-axis, the structure is divided into J *sections*[1] at $y = b^{(j)}$, $j = 1, 2, \ldots, J-1$. For simplicity, figure 2.1 is drawn with only three sections. The width of the j^{th} section is $d^{(j)} = b^{(j)} - b^{(j-1)}$. The j^{th} section is divided into I *layers* along the x-axis at $x = a^{(ij)}$, $i = 1, 2, \ldots, I-1$. The value of I varies depending on the section index j. The width of the i^{th} layer in the j^{th} section is $h^{(ij)} = a^{(ij)} - a^{(i-1,j)}$. Each layer is isotropic with permittivity $\epsilon^{(ij)}$ and permeability $\mu^{(ij)}$,

---

[1] The word "section" is used to denote both a section of the structure and a section of this thesis, and the symbol "j" is used both as an index for the section of the structure and as the imaginary number $(0, 1)$. The context will always clearly indicate the intended meaning.

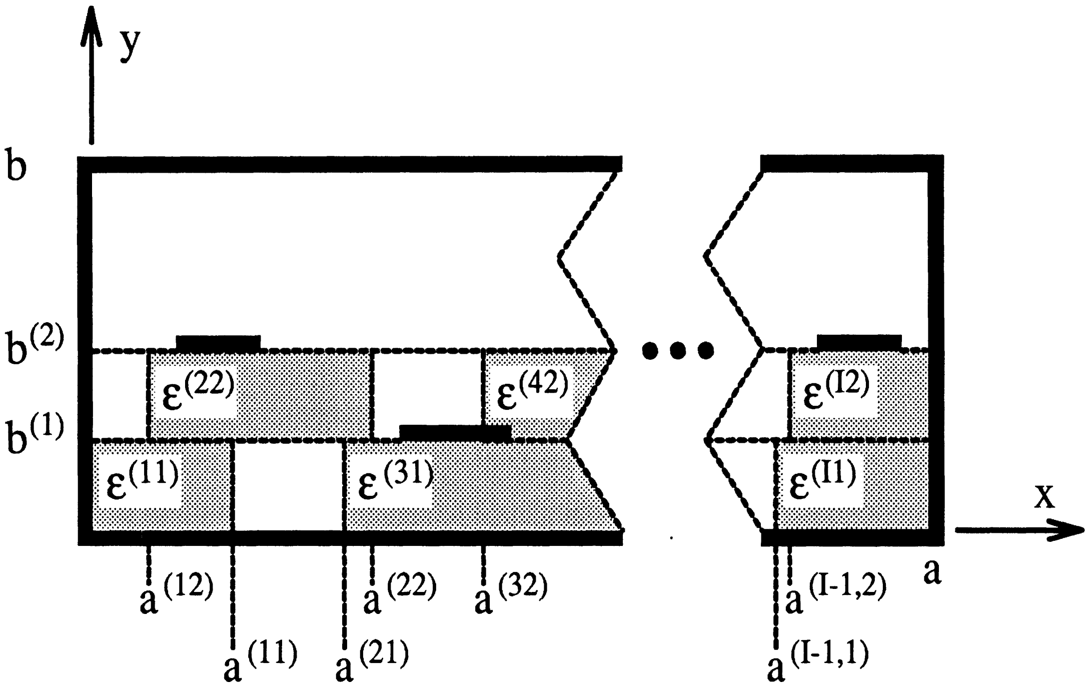

Figure 2.1: General structure for the IEMM analysis. A structure with three sections is shown; any number of sections may be used.

and all structures in this work have $\mu^{(ij)} = \mu_o$. Dielectric losses are taken into account with complex values of permittivity, e.g., $\epsilon^{(ij)} = \epsilon_o(\epsilon_r'^{(ij)} - j\epsilon_r''^{(ij)}) = \epsilon_o\epsilon_r'^{(ij)}(1 - j\tan\delta^{(ij)})$. The structure contains a total of N_c conducting strips. This work considers only strips that are located parallel to the x-axis; have negligible thicknesses (y-dimensions are zero); are of uniform width (x-dimensions of each conductor is independent of z); and are narrow with respect to guided wavelength. The last condition means that the transverse current on the strips is neglected, and only the longitudinal (i.e., $\hat{z}$-directed) current is significant. All of the limitations on the conducting strips can be removed by appropriately altering the formulation.

2.3 The Electric Field Integral Equation

The fields of the structure are determined by solving the electric field integral equation in the spatial domain. The integral equation is derived [15, ch. 2] from the time-harmonic

Maxwell's equations

$$\nabla \times \bar{E} = -j\omega\bar{B} \tag{2.1}$$

$$\nabla \times \bar{H} = j\omega\epsilon\bar{D} + \bar{J} \tag{2.2}$$

$$\nabla \cdot \bar{D} = \rho \tag{2.3}$$

$$\nabla \cdot \bar{B} = 0 \tag{2.4}$$

$$\nabla \cdot \bar{J} = -j\omega\rho \tag{2.5}$$

in conjunction with the constitutive relations

$$\bar{D} = \epsilon\bar{E} \tag{2.6}$$

$$\bar{B} = \mu\bar{H} \tag{2.7}$$

A time dependence of $e^{j\omega t}$ has been assumed and suppressed. The vector wave equation for the electric field $\bar{E}$ is derived by taking the curl of the first of Maxwell's equations and inserting the second into the result:

$$\nabla \times \nabla \times \bar{E} - k^2\bar{E} = -j\omega\mu\bar{J} \tag{2.8}$$

where $k = \omega\left(\epsilon\mu\right)^{1/2}$ is the wavenumber of the material. The electric field dyadic Green's function $\overline{\overline{G}}_E(\bar{r},\bar{r}')$ is the solution of the dyadic version of the above equation with a delta-function excitation:

$$\nabla \times \nabla \times \overline{\overline{G}}_E - k^2\overline{\overline{G}}_E = \overline{\overline{I}}\delta(\bar{r} - \bar{r}') \tag{2.9}$$

By using the above wave equations, Green's second vector-dyadic theorem [71] and appropriate identities, the integral equation is written as

$$\begin{aligned} \bar{E}(\bar{r}') &= -j\omega\mu \iiint_V \bar{J}(\bar{r}) \cdot \overline{\overline{G}}_E(\bar{r},\bar{r}')dV \\ &+ \oiint_S \left[(\hat{n} \times \nabla \times E(\bar{r})) \cdot \overline{\overline{G}}_E(\bar{r},\bar{r}') + (\hat{n} \times \bar{E}(\bar{r})) \cdot \left(\nabla \times \overline{\overline{G}}_E(\bar{r},\bar{r}')\right)\right] dS \end{aligned} \tag{2.10}$$

The volume V is enclosed by the cavity, and the surface S is the surface of the cavity walls. Since the walls of the cavity are perfectly conducting, the tangential electric field $\hat{n} \times \bar{E}$ is zero on S and the second term in the surface integral is zero. The Green's function obeys the same boundary conditions as $\bar{E}$ and the first term in the surface integral is also zero. Reciprocity can be used to show that

$$\bar{J}(\bar{r}) \cdot \overline{\overline{G}}_E(\bar{r},\bar{r}') \;=\; \overline{\overline{G}}_E(\bar{r}',\bar{r}) \cdot \bar{J}(\bar{r}) \tag{2.11}$$

After the primed and unprimed coordinate systems have been exchanged so that the notation is in agreement with convention, the electric field integral equation is

$$\bar{E}(\bar{r}) \;=\; -j\omega\mu \iiint_{V'} \overline{\overline{G}}_E(\bar{r},\bar{r}') \cdot \bar{J}(\bar{r}')\, dV' \tag{2.12}$$

Since the currents $\bar{J}$ are present only in the conducting strips, integrating over the volume of the structure is equivalent to integrating over the volumes of the conducting strips.

2.4 The Green's Function

The Green's function is the electric field when the conducting strips are replaced with a current point source at $\bar{r}'(x', y', z')$. A convenient form of the Green's function is derived by considering each section of the structure as a section of layered parallel plate waveguide and relating the fields in different sections through mode-matching.

2.4.1 Eigenfunction Expansion of the Fields in a Parallel-Plate Waveguide with Dielectric Layers

An individual section of the structure is regarded as a parallel-plate waveguide with layer interfaces in the yz-plane. The fields away from the point source obey the homogeneous wave equation

$$\nabla^2 \bar{E} + k^2 \bar{E} = 0 \tag{2.13}$$

The fields are conveniently expressed by TE$_x$ and TM$_x$ modes, and solutions to the wave equation are generated using vector potentials $\bar{A} = a_x(x, y, z)\hat{x}$ and $\bar{F} = f_x(x, y, z)\hat{x}$ via

$$\bar{E} = -j\omega\bar{A} + \frac{1}{j\omega\epsilon\mu}\nabla\nabla\cdot\bar{A} + \frac{1}{\epsilon}\nabla\times\bar{F} \tag{2.14}$$

$$\bar{H} = \frac{1}{\mu}\nabla\times\bar{A} + j\omega\bar{F} - \frac{1}{j\omega\epsilon\mu}\nabla\nabla\cdot\bar{F} \tag{2.15}$$

Since the structure is rectangular, the x-, y- and z-dependencies of a_x and f_x are separable into functions X, Y and Z. Away from the source, linear combinations of each of these functions satisfy the scalar homogeneous wave equation, and each function has an associated separation parameter (eigenvalue) [35]. The separation parameters satisfy the dispersion (separation) equation, so that only two of the separation parameters may be chosen independently. In a given layer, a_x and f_x are therefore expressed as infinite sums with two indices:

$$f_x^{(ij)}(x, y, z) = \sum_{l,n}^{\infty} \frac{1}{N_{ln}^{(j)E}} X_l^{(ij)E}(x)\, Y_{ln}^{(j)E}(y)\, Z_n^E(z) \tag{2.16}$$

$$a_x^{(ij)}(x, y, z) = \sum_{l,n}^{\infty} \frac{1}{N_{ln}^{(j)M}} X_l^{(ij)M}(x)\, Y_{ln}^{(j)M}(y)\, Z_n^M(z) \tag{2.17}$$

In practice, the sums are truncated, and the next chapter discusses how many terms in each sum are required for convergence. The fields are normalized by the factors $N_{ln}^{(j)E}$ and $N_{ln}^{(j)M}$, which are defined in the discussion of the mode-matching procedure (section 2.4.3). The superscripts i and j indicate the layer and section of the structure. The superscripts E and M refer to TE$_x$ and TM$_x$ fields; when neither of these superscripts is present, the statement or equation applies to both TE$_x$ and TM$_x$ fields. The subscripted summation indices l and n on the functions X, Y and Z indicate that the X- and Z-eigenvalues have been chosen to be independent and the Y-eigenvalues have been chosen to be dependent. The separation parameters associated with the functions $X_l^{(ij)}$, $Y_{ln}^{(j)}$ and Z_n are $k_{xl}^{(ij)}$, $k_{yln}^{(j)}$ and k_{zn}, respectively. The dispersion equation is

$$\left(k_{xl}^{(ij)}\right)^2 + \left(k_{yln}^{(j)}\right)^2 + \left(k_{zn}\right)^2 = \left(k^{(ij)}\right)^2 \tag{2.18}$$

where $k^{(ij)} = \omega(\epsilon^{(ij)}\mu^{(ij)})^{1/2}$ is the wavenumber of layer ij. Since the tangential $\bar{E}$ and $\bar{H}$ fields must be continuous at all interfaces, $k_{xl}^{(ij)}$ varies from layer to layer, $k_{yln}^{(j)}$ varies from section to section and k_{zn} has no dependence on position. The superscripts on each of the eigenvalues reflect the dependencies on position.

The x-, y-, and z-dependencies of $f_x^{(ij)}$ and $a_x^{(ij)}$ are solutions of the scalar wave equation. As indicated by the superscript, the function $X_l^{(ij)}$ varies from layer to layer in each section. In the i^{th} layer of the j^{th} section, the x-dependencies are

$$X_l^{(ij)E}(x) = A_l^{(ij)E}\cos k_{xl}^{(ij)E}(x - a^{(ij)}) + B_l^{(ij)E}\sin k_{xl}^{(ij)E}(x - a^{(ij)}) \tag{2.19}$$

$$X_l^{(ij)M}(x) = A_l^{(ij)M}\cos k_{xl}^{(ij)M}(x - a^{(ij)}) + B_l^{(ij)M}\sin k_{xl}^{(ij)M}(x - a^{(ij)}) \tag{2.20}$$

The constants $A_l^{(ij)}$, $B_l^{(ij)}$ and the eigenvalues $k_{xl}^{(ij)}$ are determined by the boundary conditions at the layer interfaces (section 2.4.2). The y-dependencies of the fields in a given section consist of infinite sums of plane waves. For convenience in the application of the boundary conditions and the subsequent expression of the Green's function, the y-dependence of the fields in the section which contains the current source is separated into two parts by

$$Y_{ln}^{(j)} = Y_{Pln}^{(j)} + Y_{Sln}^{(j)} \tag{2.21}$$

where $Y_{Pln}^{(j)}$ and $Y_{Sln}^{(j)}$ represent the primary and secondary fields. The primary fields consist of plane waves leaving the source in the $\pm y$-direction, i.e.,

$$\left.\begin{aligned} Y_{Pln}^{<(j)E}(y,y') &= C_{Pln}^{<(j)E}\exp(jk_{yln}^{(j)E}(y-y')) \\ Y_{Pln}^{<(j)M}(y,y') &= C_{Pln}^{<(j)M}\exp(jk_{yln}^{(j)M}(y-y')) \end{aligned}\right\} \quad y < y' \tag{2.22}$$

$$\left.\begin{aligned} Y_{Pln}^{>(j)E}(y,y') &= -C_{Pln}^{>(j)E}\exp(-jk_{yln}^{(j)E}(y-y')) \\ Y_{Pln}^{>(j)M}(y,y') &= C_{Pln}^{>(j)M}\exp(-jk_{yln}^{(j)M}(y-y')) \end{aligned}\right\} \quad y > y' \tag{2.23}$$

The secondary fields satisfy the homogeneous wave equation in all regions and consist of plane waves traveling in both directions, i.e.,

$$Y^{(j)E}_{Sln}(y) = \left\{ \begin{array}{ll} \left. \begin{array}{l} C^{(j)E}_{ln} \exp(-jk^{(j)E}_{yln}(y - b^{(j-1)})) \\ \quad +D^{(j)E}_{ln} \exp(jk^{(j)E}_{yln}(y - b^{(j-1)})) \end{array} \right\} & y < y' \\ \left. \begin{array}{l} -C^{(j)E}_{ln} \exp(-jk^{(j)E}_{yln}(y - b^{(j)})) \\ \quad +D^{(j)E}_{ln} \exp(jk^{(j)E}_{yln}(y - b^{(j)})) \end{array} \right\} & y > y' \end{array} \right. \tag{2.24}$$

$$Y^{(j)M}_{Sln}(y) = \left\{ \begin{array}{ll} \left. \begin{array}{l} C^{(j)M}_{ln} \exp(-jk^{(j)M}_{yln}(y - b^{(j-1)})) \\ \quad +D^{(j)M}_{ln} \exp(jk^{(j)M}_{yln}(y - b^{(j-1)})) \end{array} \right\} & y < y' \\ \left. \begin{array}{l} C^{(j)M}_{ln} \exp(-jk^{(j)M}_{yln}(y - b^{(j)})) \\ \quad +D^{(j)M}_{ln} \exp(jk^{(j)M}_{yln}(y - b^{(j)})) \end{array} \right\} & y > y' \end{array} \right. \tag{2.25}$$

$C^{<(j)E}_{Pln}$, $C^{<(j)M}_{Pln}$, $C^{>(j)E}_{Pln}$, $C^{>(j)M}_{Pln}$, $C^{(j)E}_{ln}$, $D^{(j)E}_{ln}$, $C^{(j)M}_{ln}$ and $D^{(j)M}_{ln}$ are referred to as *mode amplitudes* and are determined from the boundary conditions at the source and the section interfaces (sections 2.4.3–2.4.5). The eigenvalues $k^{(j)}_{yln}$ are determined from the dispersion equation (equation 2.18) after $k^{(ij)}_{xl}$ and k_{zn} are known. From the uniformity of the cavity in the z-direction and the boundary conditions at $z = 0$ and $z = c$, the z-dependence in all sections is deduced to be

$$Z^E_n(z) = \cos k_{zn}(z - c) \tag{2.26}$$

$$Z^M_n(z) = \sin k_{zn}(z - c) \tag{2.27}$$

where $k_{zn} = n\pi/c$.

2.4.2 The x-Dependence in Each Section

Application of the boundary conditions at each layer interface and at the upper and lower conducting walls determines the x-dependence of the fields in each layer in a given section. In addition, these boundary conditions generate transcendental equations for the x-directed wavenumbers.

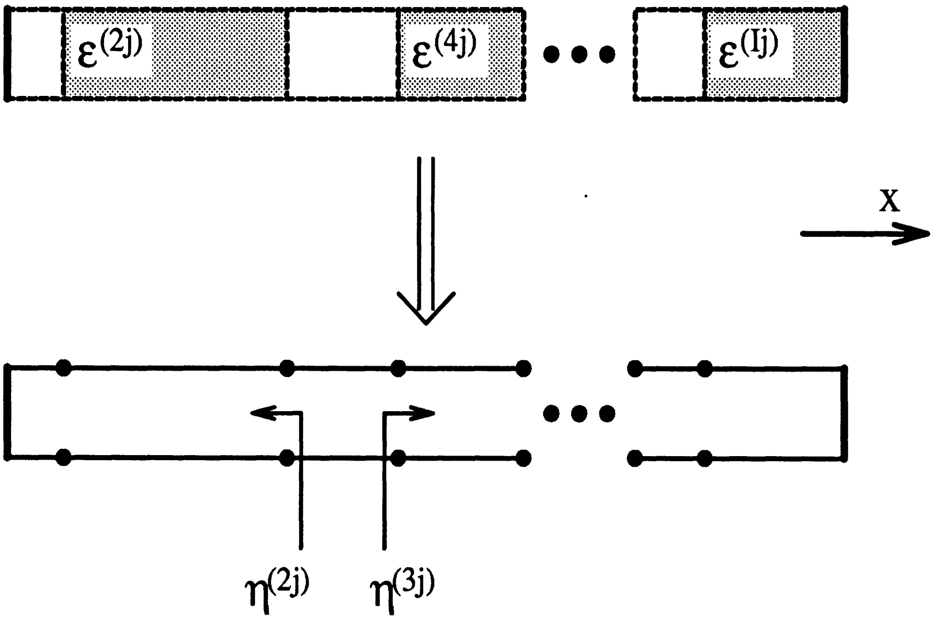

Figure 2.2: The boundary conditions at the layer interfaces in the j^{th} section form a transmission line problem.

The modes on each side of a given interface are related on a one-to-one basis [15, ch. 6] (figure 2.2). In the i^{th} section of the j^{th} layer, the boundary conditions on the TE$_x$ fields are

$$\left.\frac{E_{yln}^{(ij)E}}{H_{zln}^{(ij)E}}\right|_{x=a^{(ij)}} = \frac{\omega\mu^{(ij)}}{k_{xl}^{(ij)E}}\,\eta_l^{(ij)E} \tag{2.28}$$

$$\left.\frac{E_{yln}^{(ij)E}}{H_{zln}^{(ij)E}}\right|_{x=a^{(i-1,j)}} = \frac{\omega\mu^{(i-1,j)}}{k_{xl}^{(i-1,j)E}}\,\eta_l^{(i-1,j)E} \tag{2.29}$$

where $\eta_l^{(ij)E}$ is the normalized "wave impedance" of the l^{th} mode in region ij.

Applying the boundary condition at $x = a^{(ij)}$ and using equations 2.16, 2.19, 2.24 and 2.26 to evaluate the potential $f_x^{(ij)}$ gives

$$A_l^{(ij)E} = j\eta_l^{(ij)E} B_l^{(ij)E} \tag{2.30}$$

By combining the boundary condition at $x = a^{(i-1,j)}$ and the previous result, a familiar transmission line equation is found to relate $\eta_l^{(i-1,j)E}$ and $\eta_l^{(ij)E}$ by

$$\eta_l^{(i-1,j)E} = \frac{\mu^{(ij)}}{\mu^{(i-1,j)}} \frac{k_{xl}^{(i-1,j)E}}{k_{xl}^{(ij)E}} \left(\frac{\eta_l^{(ij)E} + j \tan k_{xl}^{(ij)E} h^{(ij)}}{1 + j\eta_l^{(ij)E} \tan k_{xl}^{(ij)E} h^{(ij)}} \right) \tag{2.31}$$

Since the walls of the cavity are perfect conductors, the impedances $\eta_l^{(Ij)E}$ and $\eta_l^{(0j)E}$ at the top and bottom walls are equal to zero. Repeated use of equation 2.31 gives $\eta_l^{(ij)E}$ for all i in terms of $k_{xl}^{(ij)E}$, and a transcendental equation for $k_{xl}^{(ij)E}$ stems from transverse resonance and the dispersion relation of equation 2.18. The solution of the transcendental equation is discussed in the next chapter. The x-dependence in each layer is completely determined by enforcing the continuity of the y-component of the TE$_x$ electric field at $x = a^{(i-1,j)}$. Substituting for $f_x^{(ij)}$ and $f_x^{(i-1,j)}$ and using the results for $A_l^{(ij)E}$ and $\eta_l^{(i-1,j)E}$ gives

$$\begin{aligned} B_l^{(i-1,j)E} &= \\ &\frac{\epsilon^{(i-1,j)}\mu^{(i-1,j)}k_{xl}^{(ij)E}}{\epsilon^{(ij)}\mu^{(ij)}k_{xl}^{(i-1,j)E}} \left(\cos k_{xl}^{(ij)E} h^{(ij)} + j\eta_l^{(ij)E} \sin k_{xl}^{(ij)E} h^{(ij)}\right) B_l^{(ij)E} \end{aligned} \tag{2.32}$$

Therefore, $A_l^{(ij)E}$ and $B_l^{(ij)E}$ for all layers i in the j^{th}-section are known in terms of one unknown. This unknown is taken to be $B_l^{(Ij)E}$, where the superscript Ij denotes the top layer of the j^{th}-section. The definition $B_l^{(Ij)E} \equiv 1$ allows $B_{ln}^{(Ij)E}$ to be absorbed into the constants $C_{ln}^{(j)E}$ and $D_{ln}^{(j)E}$. Similar relations hold for $A_l^{(ij)M}$, $B_l^{(ij)M}$, and $\eta_l^{(ij)M}$:

$$B_l^{(ij)M} = -j\eta_l^{(ij)M} A_l^{(ij)M} \tag{2.33}$$

$$\eta_l^{(i-1,j)M} = \frac{\epsilon^{(i-1,j)}}{\epsilon^{(ij)}} \frac{k_{xl}^{(ij)M}}{k_{xl}^{(i-1,j)M}} \left(\frac{\eta_l^{(ij)M} + j \tan k_{xl}^{(ij)M} h^{(ij)}}{1 + j\eta_l^{(ij)M} \tan k_{xl}^{(ij)M} h^{(ij)}} \right) \tag{2.34}$$

$$A_{ln}^{(i-1,j)M} = \frac{\mu^{(i-1,j)}}{\mu^{(ij)}} \left(\cos k_{xl}^{(ij)M} h^{(ij)} + j\eta_l^{(ij)M} \sin k_{xl}^{(ij)M} h^{(ij)}\right) A_{ln}^{(ij)M} \tag{2.35}$$

Again, the impedances of the walls at $x = 0$ and $x = a$ are $\eta_l^{(0j)M} = \eta_l^{(Ij)M} = 0$, and $\eta_l^{(ij)M}$ and a transcendental equation for $k_{xl}^{(ij)M}$ is determined; also, $A_l^{(ij)M}$ and $B_l^{(ij)M}$ are known in terms of $A_l^{(Ij)M}$, and the definition $A_l^{(Ij)M} \equiv 1$ allows $A_l^{(Ij)M}$ to be absorbed into the constants $C_{ln}^{(j)M}$ and $D_{ln}^{(j)M}$.

2.4.3 Mode-Matching at Section Interfaces

The basic approach for satisfying the boundary conditions at the section interfaces is mode-matching [17, 52, 68]. A transmission matrix can theoretically be used to relate the fields at $y = b^{(j)}$ to the fields at $y = 0$, but the number of modes necessary for convergence combined with the distances involved cause numerical instability[2]. A numerically stable approach modifies the classical mode-matching matrix to a generalized scattering matrix [47, 48, 63, 64]. At each interface, three conditions may be enforced: the continuity of the tangential E-field; the continuity of the tangential H-field; and the conservation of complex power. The scattering matrix is derived by enforcing any two of these three conditions [55]. None of the three conditions is computationally advantageous, so the choice of which two conditions are to be enforced at the section interfaces is arbitrary.

The continuity of the tangential E- and H-fields are selected as the two conditions to be enforced, and the modes are matched by multiplying each boundary condition equation by appropriate testing functions and integrating. At $y = b^{(j)}$, the chosen boundary conditions are expressed as

$$\sum_{ln}^{\infty} E_{xln}^{(j)M} = \sum_{ln}^{\infty} E_{xln}^{(j+1)M} \tag{2.36}$$

$$\sum_{l}^{\infty} H_{xln}^{(j)E} = \sum_{ln}^{\infty} H_{xln}^{(j+1)E} \tag{2.37}$$

$$\sum_{ln}^{\infty} \left(E_{zln}^{(j)E} + E_{zln}^{(j)M}\right) = \sum_{ln}^{\infty} \left(E_{zln}^{(j+1)E} + E_{zln}^{(j+1)M}\right) \tag{2.38}$$

$$\sum_{ln}^{\infty} \left(H_{zln}^{(j)E} + H_{zln}^{(j)M}\right) = \sum_{ln}^{\infty} \left(H_{zln}^{(j+1)E} + H_{zln}^{(j+1)M}\right) \tag{2.39}$$

If the testing functions are orthogonal in some manner to the fields, the above equations will be simplified because some of the infinite summations will be eliminated. Derived in appendix A, the orthogonal properties of the fields are determined from the general

---

[2] The stability of the transmission matrix formulation depends on the ability of the computer to represent the fields' y-dependence, i.e., the quantity $\exp(\pm jk_{yln}^{(j)} d^{(j)})$. As l and n increase, the imaginary part of $k_{yln}^{(j)}$ becomes large and the exponential nature of the y-dependence can cause numerical over- and underflows.

reciprocity principle for a source-free waveguide with perfectly conducting walls [15, ch. 6]. In a transverse (xy) plane, the TE$_x$ modes are orthogonal to each other, as are the TM$_x$ modes, and the TE$_x$ modes are also orthogonal to the TM$_x$ modes; in a longitudinal (xz) plane, the orthogonality is limited in that the TE$_x$ modes are not orthogonal to the TM$_x$ modes. The latter case corresponds to this application of mode matching, and the orthogonality properties are

$$\int_0^c \int_0^a \bar{E}_{tln}^{(j)E} \times \bar{H}_{tl'n'}^{(j)E} \cdot \hat{y}\, dx\, dz = N_{xln}^{(j)E} N_{zn}^{E}\, \delta_{ll'}\, \delta_{nn'} \tag{2.40}$$

$$\int_0^c \int_0^a \bar{E}_{tln}^{(j)M} \times \bar{H}_{tl'n'}^{(j)M} \cdot \hat{y}\, dx\, dz = N_{xln}^{(j)M} N_{zn}^{M}\, \delta_{ll'}\, \delta_{nn'} \tag{2.41}$$

$$\int_0^c \int_0^a \bar{E}_{tln}^{(j)E} \times \bar{H}_{tln'}^{(j)M} \cdot \hat{y}\, dx\, dz = N_{xln}^{(j)EM} N_{zn}^{EM}\, \delta_{nn'} \tag{2.42}$$

$$\int_0^c \int_0^a \bar{E}_{tln}^{(j)M} \times \bar{H}_{tln'}^{(j)E} \cdot \hat{y}\, dx\, dz = N_{xln}^{(j)ME} N_{zn}^{ME}\, \delta_{nn'} \tag{2.43}$$

where $\bar{E}_{tln}^{(j)}$ and $\bar{H}_{tln}^{(j)}$ are the fields in the xz-plane; $\delta_{ll'}$ and $\delta_{nn'}$ are Kronecker deltas; $N_{xln}^{(j)E}$, $N_{xln}^{(j)M}$, $N_{xln}^{(j)EM}$, and $N_{xln}^{(j)ME}$ are the values of the integrals over x; and N_{zn}^{E}, N_{zn}^{M}, N_{zn}^{EM}, and N_{zn}^{ME} are the values of the integrals over z. These equations are valid even if the materials in the structure are lossy. Multiplying equations 2.36–2.39 by $H_{l'n'z}^{M}$, $E_{l'n'x}^{E}$, $H_{l'n'z}^{E}$ and $H_{l'n'x}^{M}$, integrating over the xz-plane, and manipulating the resulting system of equations determines the interface scattering matrix.

Various normalizations are applied in conjunction with the use of scattering matrices. For example, when scattering matrices are used to relate modal quantities in circuit analysis, the modes are typically normalized so that each mode propagates 1 unit of power. Consequently, the scattering matrix is symmetric and independent of the characteristic impedances of the transmission lines at the ports [16]. Such symmetry can greatly reduce computation time, so a similar normalization scheme is commonly employed when generalized scattering matrices are used in mode matching formulations [9, 10, 23, 58]. The propagating modes again carry 1 unit of power, and the evanescent modes carry $\pm j$ unit of power. In general, this normalization is possible if all modes are orthonormal [24]. Other normalization conditions which lead to a symmetric imaginary impedance matrix for a lossless structure are given in [37].

Although a symmetric scattering matrix $[S]$ is desirable for the IEMM method, no such normalization could be found. Since the mode matching is performed in a longitudinal plane, the TE_x modes are not orthogonal to the TM_x modes (equations 2.42–2.43); unfortunately, the conclusion in [24] is not valid under these circumstances. The asymmetry of $[S]$ raises questions about reciprocity, since in circuit analysis reciprocity dictates that the scattering matrix be symmetric. Reciprocity is not violated by the asymmetry; as discussed earlier, reciprocity has been proven for a general inhomogeneous waveguide with perfectly conducting walls. The symmetry of $[S]$ depends in part on the normalization, and a normalization which symmetrizes the scattering matrix might still exist; further research is necessary in this area. In this work, the normalization is performed in accordance with the field orthogonality properties, and, although the scattering matrices are not symmetric, the normalization does improve the matrix condition numbers. The choices for the normalization factors $N_{ln}^{(j)E}$ and $N_{ln}^{(j)M}$ are determined by equations 2.40–2.41:

$$N_{ln}^{(j)E} = \left(N_{xl}^{(j)E} N_{zln}^{E}\right)^{1/2} \tag{2.44}$$

$$N_{ln}^{(j)M} = \left(N_{xl}^{(j)M} N_{zln}^{M}\right)^{1/2} \tag{2.45}$$

where

$$N_{xln}^{(j)E} = -k_{yln}^{(j)E}\left((k^{(ij)})^2 - (k_{xl}^{(ij)E})^2\right)\int_0^a \frac{(X_l^{(ij)E}(x))^2}{\epsilon^{(ij)}\mu^{(ij)}\omega\epsilon^{(ij)}}\,dx \tag{2.46}$$

$$N_{zn}^{(j)E} = \int_0^c (Z_n^E(z))^2 dz \tag{2.47}$$

$$N_{xln}^{(j)M} = -k_{yln}^{(j)M}\left((k^{(ij)})^2 - (k_{xl}^{(ij)M})^2\right)\int_0^a \frac{(X_l^{(ij)M}(x))^2}{\epsilon^{(ij)}\mu^{(ij)}\omega\mu^{(ij)}}\,dx \tag{2.48}$$

$$N_{zn}^{(j)M} = \int_0^c (Z_n^M(z))^2 dz \tag{2.49}$$

(Note that from the dispersion relation (equation 2.18),

$$(k^{(ij)})^2 - (k_{xl}^{(ij)})^2 = k_{zn}^2 - (k_{yln}^{(j)})^2 \tag{2.50}$$

so that this quantity does not vary with x and is not included in the integrals of equations 2.46 and 2.48.)

The scattering matrices are defined by the equations

$$\begin{bmatrix} L^{(j)}D^{(j)} \\ C^{(j+1)} \end{bmatrix} = \left[S^{(j)}\right] \begin{bmatrix} L^{(j)-1}C^{(j)} \\ D^{(j+1)} + \Lambda^{(j+1)}(b^{(j)} - y')\,C_P^{<(j+1)} \end{bmatrix} \quad b^{(j)} < y' \tag{2.51}$$

$$\begin{bmatrix} L^{(j+1)}C^{(j+1)} \\ D^{(j)} \end{bmatrix} = \left[S^{(j)}\right] \begin{bmatrix} L^{(j+1)-1}D^{(j+1)} \\ C^{(j)} + \Lambda^{(j)-1}(b^{(j)} - y')\,C_P^{>(j)} \end{bmatrix} \quad b^{(j)} > y' \tag{2.52}$$

where

$$L^{(j)\pm 1} = \operatorname{diag}\{\exp(\pm jk_{yln}^{(j)}d^{(j)})\} \tag{2.53}$$

$$\Lambda^{(j)\pm 1}(d) = \operatorname{diag}\{\exp(\pm jk_{yln}^{(j)}d)\} \tag{2.54}$$

The elements of the interface scattering matrices $S^{(j)}$ are given in appendix B. $C^{(j)}$, $D^{(j)}$, $C^{(j+1)}$, and $D^{(j+1)}$ are vectors which contain the secondary field mode amplitudes and $C_P^{<(j+1)}$ and $C_P^{>(j)}$ are vectors which contain the primary field mode amplitudes. The primary fields are included in the boundary conditions via the vectors C_P; by definition, $C_P^{(j)} = 0$ unless section j contains the source.

2.4.4 Boundary Conditions at the Source

The boundary conditions at the source ($y = y'$) are satisfied by the primary fields, and the primary field mode amplitudes $C_{Pln}^{<(j)}$ and $C_{Pln}^{>(j)}$ are thereby explicitly determined. The procedure followed in determining $C_{Pln}^{<(j)}$ and $C_{Pln}^{>(j)}$ is similar to that in [57]. As discussed in section 2.2, each conducting strip has only a longitudinal ($\hat{z}$) current component, so only a longitudinal current source is considered. The source can be replaced with an equivalent layer of surface current [72] in the xz-plane at $y = y'$, and the boundary conditions at this layer are

$$
\begin{aligned}
E_x^< &= E_x^> && (2.55)\\
E_z^< &= E_z^> && (2.56)\\
H_x^> - H_x^< &= -\delta(x-x')\delta(z-z') && (2.57)\\
H_z^< &= H_z^> && (2.58)
\end{aligned}
$$

Use of the orthogonality relations (equations 2.40–2.43) and the property of the delta-function that

$$\int_0^a f(x)\delta(x-x')dx = f(x') \qquad 0 < x' < a \tag{2.59}$$

gives expressions for the primary field mode amplitudes:

$$
\begin{aligned}
C_{Pln}^{<(j)E} &= C_{Pln}^{>(j)E} = \frac{j\omega\, N_{ln}^{(j)E}\, X_l^{(ij)E}(x')\, Z_n^E(z')}{2\epsilon^{(ij)}\left((k^{(ij)})^2 - (k_{xl}^{(ij)E})^2\right) I_0^E(l)\, I_{zn}} && (2.60)\\
C_{Pln}^{<(j)M} &= C_{Pln}^{>(j)M} = -\frac{I_{zn}^{EM}\, N_{ln}^{(j)M}}{jk_{yln}^{(j)M}} \sum_{l'}^{\infty} \frac{C_{Pl'n}^{<(j)E}}{N_{l'n}^{(j)E}} I_4^{EM}(l',l) && (2.61)
\end{aligned}
$$

where

$$
\begin{aligned}
I_{zn} &= \int_0^c (Z_n^E(z))^2 dz\\
&= \int_0^c \cos^2 k_{zn}(z-c)\, dz = \begin{cases} \dfrac{c}{2} & k_{zn} \neq 0 \\ c & k_{zn} = 0 \end{cases} && (2.62)
\end{aligned}
$$

and $I_0^E(l)$, $I_4^{EM}(l',l)$ and I_{zn}^{EM} are coupling integrals which are defined in appendix B.

The truncation of the sum in equation 2.61 depends on the section of the structure in which the primary field mode amplitudes are determined. In most cases, each conductor in the structure is placed on an interface between two sections of the structure (figure 2.1). When the Green's function is calculated, one of these two sections must be chosen as the "source section," i.e., the section which contains the source. For example, in figure 2.1, either section 2 or 3 might be chosen as the source section for the upper two conductors, and either section 1 or 2 might be chosen for the lower conductor. In a homogeneous section (i.e., a section with only one layer), the TE$_x$ fields are orthogonal to the TM$_x$ fields, and the integral $I_4^{EM}(l',l)$ is nonzero only when $l = l'$. In this case, consistent with the Green's function of an empty parallel plate waveguide, the summation in equation 2.61 has only one term. In an inhomogeneous (multilayered) section, the TE$_x$ fields are not orthogonal to the TM$_x$ fields, and the summation requires enough terms for it to converge. When the conductors are at a section interface between an inhomogeneous and a homogeneous section, it is therefore numerically convenient to choose the homogeneous section as the one which is to contain the source. In this work, all structures have a homogeneous section as the source section, so truncation of the sum is not considered.

2.4.5 Relating the Fields of the Individual Parallel-Plate Waveguide Sections

In order to relate the fields in all sections, reflection coefficient matrices are defined for waves at the interfaces between sections. At the interface $y = b^{(j-1)}$, in the j^{th} section, when $y < y'$, and when section j does not contain the source (so that the primary fields are zero), the reflection coefficient matrix $\Gamma^{<(j)}$ relates the secondary field mode amplitude vectors $C^{(j)}$ and $D^{(j)}$ by

$$C^{(j)} = \Gamma^{<(j)} D^{(j)} \tag{2.63}$$

This equation and the definition of the interface scattering matrix in equations 2.51–2.52 are combined to give

$$\Gamma^{<(j+1)} = S_{22}^{(j)} + S_{21}^{(j)} \left(-S_{11}^{(j)} + \left(L^{(j)-1} \Gamma^{<(j)} L^{(j)-1} \right)^{-1} \right)^{-1} S_{12}^{(j)} \tag{2.64}$$

Similarly, at the interface $y = b^{(j)}$, in the j^{th} section, when $y > y'$, and when section j does not contain the source, the reflection coefficient matrix $\Gamma^{>(j)}$ relates the secondary field mode amplitudes by

$$D^{(j)} = \Gamma^{>(j)} C^{(j)} \tag{2.65}$$

so that

$$\Gamma^{>(j)} = S_{22}^{(j)} + S_{21}^{(j)} \left(-S_{11}^{(j)} + \left(L^{(j+1)-1} \Gamma^{>(j+1)} L^{(j+1)-1} \right)^{-1} \right)^{-1} S_{12}^{(j)} \tag{2.66}$$

Since the ends of the waveguide at $y = 0$ and $y = b$ are perfectly conducting walls,

$$\Gamma^{<(1)} = \Gamma^{>(J)} = -I \tag{2.67}$$

where I is the identity matrix. Repeated use of equations 2.63 and 2.65 gives $\Gamma^{<(j)}$ and $\Gamma^{>(j)}$ for the section which contains the source.

When the reflection coefficient equations are applied at the boundaries of the section which contains the source, the primary fields must be taken into account. The section which contains the source is divided into two regions at $y = y'$, and $C_{ln}^{<(j)}$ and $D_{ln}^{<(j)}$ are the mode amplitudes for $y < y'$ and $C_{ln}^{>(j)}$ and $D_{ln}^{>(j)}$ are the mode amplitudes for $y > y'$. These mode amplitudes are related by

$$C^{<(j)} = L^{(j)} C^{>(j)} \tag{2.68}$$

$$D^{<(j)} = L^{(j)-1} D^{>(j)} \tag{2.69}$$

and, from the reflection coefficient matrix definitions (equations 2.63 and 2.65) with nonzero primary fields,

$$C^{<(j)} = \Gamma^{<(j)} \left(D^{<(j)} + \Lambda^{(j)} (b^{(j-1)} - y') C_P^{<(j)} \right) \tag{2.70}$$

$$D^{>(j)} = \Gamma^{>(j)} \left(C^{>(j)} + \Lambda^{(j)} (y' - b^{(j)}) C_P^{>(j)} \right) \tag{2.71}$$

From equations 2.68-2.71, the expressions for $C^{>(j)}$ and $D^{<(j)}$ are

$$C^{>(j)} = \left(I - L^{(j)-1} \Gamma^{<(j)} L^{(j)-1} \Gamma^{>(j)} \right)^{-1} L^{(j)-1} \Gamma^{<(j)}$$

$$\left(L^{(j)-1}\Gamma^{>(j)}\Lambda^{(j)}(y'-b^{(j)})+\Lambda^{(j)}(b^{(j-1)}-y')\right) C_P^{\lessgtr(j)} \tag{2.72}$$

$$D^{<(j)} = \left(I-L^{(j)-1}\Gamma^{>(j)}L^{(j)-1}\Gamma^{<(j)}\right)^{-1} L^{(j)-1}\Gamma^{>(j)}$$

$$\left(L^{(j)-1}\Gamma^{<(j)}\Lambda^{(j)}(b^{(j-1)}-y')+\Lambda^{(j)}(y'-b^{(j)})\right) C_P^{\lessgtr(j)} \tag{2.73}$$

The secondary field mode amplitudes are determined from equations 2.72 and 2.71 when the fields are required for $y < y'$, or from equations 2.73 and 2.70 when the fields are required for $y > y'$. (The fields, and hence the Green's function, must be known for either $y < y'$ or for $y > y'$ in order for the integral equation to be solved; if $y' = b^{(j)}$, the equations for $y > y'$ are simpler, and if $y' = b^{(j-1)}$, the equations for $y < y'$ are simpler. The fields must be known over the entire cross-section of the structure, i.e., for both $y < y'$ and $y > y'$, when the characteristic impedance is calculated, as shown in section 2.6.2, equation 2.98.) With the inclusion of the primary fields, the secondary field mode amplitudes $C^{(j)}_{ln}$ and $D^{(j)}_{ln}$ in the source section have been found in terms of the primary field mode amplitudes $C^{\lessgtr(j)}_{Pln}$.

2.4.6 Concise Expression for the Green's Function

The xz-, yz-, and zz-components of the Green's function are determined by substituting for A and F in equation 2.14 with the results of sections 2.4.1–2.4.5 and equating $\overline{\overline{G}}_E \cdot \hat{z} = \bar{E}$ (since these results were derived from a delta-function excitation). Since the current $\bar{J}$ has only a z-component, the integral equation requires only these three components of the Green's function:

$$G^{(j)}_{E\nu z}(x,y,z;x',y',z') = \left[U^{(j)}_{\nu 1}(x,y,z)\right]^T R^{(j)}\, U^{(j)}_2(x',y',z') \tag{2.74}$$

where $\nu = x, y, z$; $R^{(j)}$ is a matrix which depends on whether $y' < y$ or $y' > y$; the index j is determined by which section contains y'; and $U^{(j)}_{\nu 1}$ and $U^{(j)}_2$ are vectors which contain the explicit dependencies of the Green's function on (x, y, z) and (x', y', z'). Expressions for

$R^{(j)}$, $U_{\nu 1}^{(j)}$ and $U_2^{(j)}$ are given in appendix C. The matrix $R^{(j)}$ contains information about the dielectric support structure relative to section j. $R^{(j)}$ is determined for each section of a given dielectric support structure, and efficient and swift analysis is possible for any configuration of conductors which are placed on the dielectric support structure.

2.5 Method of Moments Solution to the Integral Equation

Given the x-, y- and z-dependencies of the fields which are excited by a point source, the components of the Green's function are known and the integral equation can be solved. The current distribution is described with appropriate orthonormal basis functions, and the method of moments is applied to obtain a matrix equation for the unknown current coefficients.

2.5.1 Expression of the Current with Basis Functions

An efficient and effective method of moments solution to the integral equation relies on the choice of basis functions. Accurate results can be obtained from very few terms with basis functions which closely resemble the actual currents. Relevant to the choice of basis functions are the assumptions of section 2.2, namely, that all currents on the conducting strips have only longitudinal ($\hat{z}$) current components and each conductor has uniform width with respect to z.

The x-dependence reflects the edge condition on the current. The current is singular along the longitudinal strip edges [51], and the singularity is modeled by Tschebyscheff polynomials of the first kind $T_p(x)$ weighted by an edge factor [5] (figure 2.3). The use of entire domain basis functions means that no discretization is necessary in the x-direction.

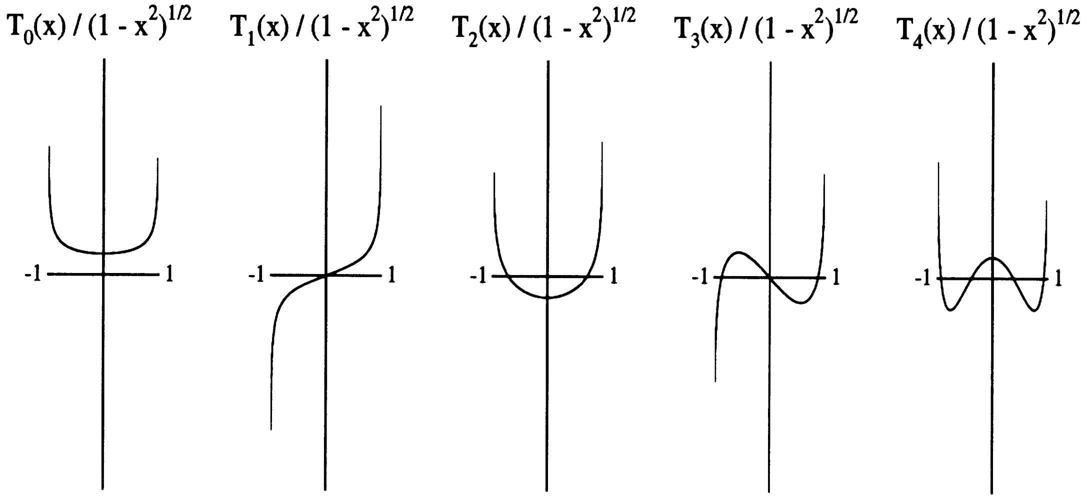

Figure 2.3: The first five weighted Tschebyscheff polynomial basis functions which describe the transverse dependence of the longitudinal current on the conducting strips.

If the m^{th} conductor has width w_{mx} and is centered at x_m, then the p^{th} basis function is

$$\Psi_{mp}(x) = \begin{cases} \dfrac{T_p\left(\frac{2(x-x_m)}{w_{mx}}\right)}{\frac{\pi w_{mx}}{2(2-\delta_{p0})}\sqrt{1-\left(\frac{2(x-x_m)}{w_{mx}}\right)^2}} & x_m - \frac{w_{mx}}{2} \le x \le x_m + \frac{w_{mx}}{2} \\ 0 & \text{otherwise} \end{cases} \tag{2.75}$$

where δ_{p0} is the Kronecker delta function. The quantity $\frac{\pi w_{mx}}{2(2-\delta_{p0})}$ normalizes the function so that

$$\int_{x_m - w_{mx}/2}^{x_m + w_{mx}/2} \left(\Psi_{mp}(x)\right)^2 \, dx = 1 \tag{2.76}$$

When the conductors are narrow and not extremely close to one another, the zeroth order basis function is sufficient to accurately describe the x-dependence. As evidenced in the validation of the method (chapter III), none of the structures in this work require higher order basis functions for accurate results; for completeness, the current is expressed as a sum of these basis functions in the remainder of this chapter.

An efficient and accurate choice for the z-dependence of the basis function is a piecewise sinusoid [69, 81] (figure 2.4). Of primary concern in the development of this method are three-dimensional structures which have finite length (z-dimension) conductors. The z-

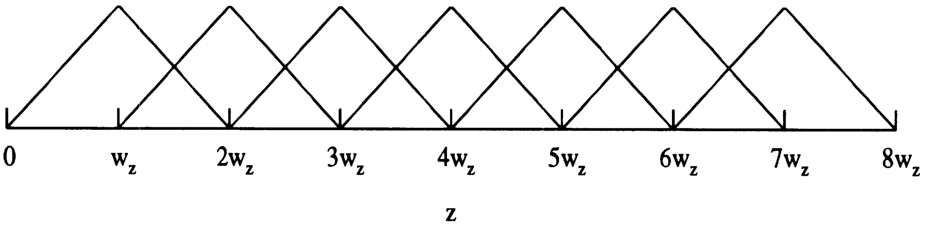

Figure 2.4: Piecewise sinusoidal basis functions which describe the longitudinal dependence of the longitudinal current on the conducting strips, shown for a uniformly discretized strip of length $8w_z$.

dependence of the current in the proximity of the end of a conductor cannot be predicted as easily as the x-dependence, hence subdomain, rather than entire domain, basis functions are used [84]. The piecewise sinusoid satisfies the edge condition on the current at the end of the strip, i.e., that the $\hat{z}$ component of current go to zero. In addition, the integrals associated with the solution of the integral equation (section 2.5.4) are easily determined and efficiently calculated when piecewise sinusoids are used. The conductors are discretized in the longitudinal direction into a total of M subsections, the m^{th} subsection has length w_{mz}, and the piecewise sinusoid is

$$\Phi_m(z) = \begin{cases} \dfrac{\sin k_s(z - z_{m-1})}{\sin k_s w_{mz}} & \text{for} \quad z_{m-1} \leq z \leq z_m \\ \dfrac{\sin k_s(z_{m+1} - z)}{\sin k_s w_{mz}} & \text{for} \quad z_m \leq z \leq z_{m+1} \end{cases} \tag{2.77}$$

where $w_{mz} = z_{m+1} - z_m$. As shown in figure 2.4, the usual choices for k_s and M cause the piecewise sinusoid to appear triangular. The parameter k_s is typically either the free space wavenumber [69] or the wavenumber of a nearby dielectric material [77]. Because of the complexity of the structures, many different materials might be in close proximity to the conductor, and k_s is therefore chosen as the maximum real part of the material wavenumbers in the structure, i.e., $\max\{Re\{k^{(ij)}\}, i = 1, I, j = 1, J\}$. The number of samples M is determined by accuracy requirements (chapter III).

The current on the m^{th} subsection is expressed in terms of the basis functions $\Psi_p(x)$

and $\Phi_m(z)$ with unknown coefficients I_{mp} as

$$\bar{J}_m(x,y,z) = \sum_{p=0}^{P} I_{mp}\, \Psi_{mp}(x)\, \delta(y-y_m)\, \Phi_m(z)\hat{z} \tag{2.78}$$

where y_m is the y-coordinate of the m^{th} subsection. The integral equation (equation 2.12) is then

$$\bar{E} = -j\omega\mu \sum_{m=1}^{M}\sum_{p=0}^{P} \iint_{S'_m} \overline{\overline{G}}_E(x,y,z;x',y_m,z') \cdot \hat{z}\, I_{mp}\, \Psi_{mp}(x')\, \Phi_m(z')\, dx'\, dz' \tag{2.79}$$

where S'_m is the area of the m'^{th} subsection.

If the conductors are not of uniform width, then the complexity of the geometry dictates that the x-dependence also be described with subsectional basis functions and that the transverse current be included in the formulation.

2.5.2 Galerkin's Method

The boundary conditions on the conducting strips are applied with Galerkin's technique. The inner products of the integral equation 2.79 with testing functions which are the same as the basis functions are expressed as

$$\iint_{S_{m'}} \hat{z} \cdot \bar{E}(x,y_{m'},z)\, \Psi_{m'p'}(x)\, \Phi_{m'}(z)\, dx\, dz = Z_{(m'p')(mp)}\, I_m$$
$$m' = 1,\ldots,M \qquad p' = 1,\ldots,P \tag{2.80}$$

where

$$Z_{(m'p')(mp)} = -j\omega\mu \iint_{S'_m}\iint_{S_{m'}} G_{Ezz}(x,y_{m'},z;x',y_m,z')$$
$$\Psi_{mp}(x')\, \Psi_{m'p'}(x)\, \Phi_m(z')\, \Phi_{m'}(z)\, dx'\, dx\, dz'\, dz \tag{2.81}$$

The only component of the Green's function which contributes to $Z_{(m'p')(mp)}$ is G_{Ezz}. The resulting matrix equation is

$$[V] = [Z]\,[I] \tag{2.82}$$

where $[V]$ is the excitation vector, $[I]$ is the vector of unknown current coefficients and $[Z]$ is the $(MP) \times (MP)$ impedance matrix with elements $Z_{(m'p')(mp)}$.

2.5.3 Excitation

A gap generator [43] is used to excite the line. The z-component of the electric field on the conductor is assumed to be non-zero across one of the subsections, and the integral on the left-hand side of equation 2.80 is therefore non-zero across this subsection. Since the information which will be extracted from the currents on the strips depends only on the relative phases of the current waves traveling in the $\pm\hat{z}$-directions (section 6.1.1), the exact value of the field in the gap is arbitrary. For convenience, the value of the excitation integral is set to 1, so that

$$[V] = [0\,0 \cdots 0\,1\,0 \cdots]^T \tag{2.83}$$

where the indexing of V is such that the "1" in the vector corresponds to the position of the gap generator on the conductor.

2.5.4 Evaluation of the Impedance Matrix Integrals

The double surface integrals associated with the impedance matrix elements are separated into single integrals over x and z.

The integrals over x are very similar to the integrals in [5]:

$$\begin{aligned}\int_{x_m - w_{mx}/2}^{x_m + w_{mx}/2} \Psi_{mp}(x) \left\{ \begin{array}{c} \cos k_x(x-a) \\ \\ \sin k_x(x-a) \end{array} \right\} dx \\ = \left\{ \begin{array}{c} \cos\left(k_x(x_m - a) + \dfrac{p\pi}{2}\right) \\ \sin\left(k_x(x_m - a) + \dfrac{p\pi}{2}\right) \end{array} \right\} (2 - \delta_{p0})\, J_p(k_x w_{mx}/2)\end{aligned} \tag{2.84}$$

where J_p is the p^{th} order Bessel function of the first kind and k_x must be constant over the range $x_m - w_{mx}/2$ and $x_m + w_{mx}/2$. Since k_x varies from layer to layer, the condition on

k_x is met in structures where a homogeneous layer is either above or below the entire width of each conducting strip. All of the structures analyzed in this thesis meet this condition; if this condition is not met, the integral in equation 2.84 must be numerically evaluated or different basis functions must be used.

The integrals over z are

$$\begin{aligned}
&\int_{z_{m-1}}^{z_{m+1}} \Phi_m(z)\, Z_n^E(z)\, dz \\
&\quad = \; w_{mz}^2 k_s \frac{\operatorname{sinc}(k_s + k_{zn})\frac{w_{mz}}{2} \operatorname{sinc}(k_s - k_{zn})\frac{w_{mz}}{2}}{\sin k_s w_{mz}} \cos k_{zn}(c - z_m) \qquad (2.85)
\end{aligned}$$

and

$$\int_{z_{m-1}}^{z_{m+1}} \Phi_m(z)\, \frac{dZ_n^M}{dz}\, dz = \int_{z_{m-1}}^{z_{m+1}} \Phi_m(z)\, Z_n^E(z)\, dz \qquad (2.86)$$

2.6 Characterization of Two-Dimensional Structures

The IEMM method has been described for three-dimensional structures, but the propagation constant and characteristic impedance of a two-dimensional structure can be determined by employing an appropriate Fourier transform of the method.

2.6.1 IEMM Method in Two Dimensions and Calculation of the Propagation Constant

In the two-dimensional case, the structure is infinite in the z-direction, and the transform and its inverse are given by

$$\tilde{A}(k_z) = \int_{-\infty}^{\infty} A(z) e^{jk_z z} dz \qquad (2.87)$$

$$A(z) = \frac{1}{2\pi} \int_{-\infty}^{\infty} \tilde{A}(k_z) e^{-jk_z z} dk_z \qquad (2.88)$$

and the associated transformed derivatives are

$$\frac{\partial \tilde{A}}{\partial z} = -jk_z \tilde{A}(k_z) \qquad (2.89)$$

The differences between the two- and three-dimensional formulations of the Green's function are detailed in appendix D.

The method of moments is again used to solve the integral equation. The transformed Green's function is

$$\tilde{\overline{\overline{G}}}_E(x,y,k_z;x',y',z') = \tilde{\overline{\overline{g}}}_E(x,y,k_z;x',y')e^{jk_zz'} \tag{2.90}$$

and the inverse transform is

$$\overline{\overline{G}}_E(x,y,z;x',y',z') = \frac{1}{2\pi}\int_{-\infty}^{\infty} \tilde{\overline{\overline{g}}}_E(x,y,k_z;x',y')e^{-jk_z(z-z')}dk_z \tag{2.91}$$

The current on the m^{th} conducting strip is

$$\bar{J}_m(x,y,z) = \sum_{p=0}^{P} I_{mp}\,\Psi_{mp}(x)\,\delta(y-y_m)\,e^{-jk_z'z}\hat{z} \tag{2.92}$$

where Ψ_{mp} are the basis functions of equation 2.75 and the current is assumed to have a propagation constant $\gamma = jk_z'$ which is equal to the propagation constant of the structure as a whole. The integral equation (from equation 2.12) is

$$\begin{aligned}
\bar{E} &= \frac{-j\omega\mu}{2\pi}\sum_{m=1}^{M}\sum_{p=0}^{P}\int_{x_m-w_{mx}/2}^{x_m+w_{mx}/2}\int_{-\infty}^{\infty}\left\{\int_{-\infty}^{\infty}\tilde{\overline{\overline{g}}}_E(x,y,k_z;x',y_m)e^{-jk_z(z-z')}dk_z\right\}\cdot\hat{z} \\
&\qquad I_{mp}\Psi_{mp}(x')e^{-jk_z'z'}\,dz'\,dx' \\
&= \frac{-j\omega\mu}{2\pi}\sum_{m=1}^{M}\sum_{p=0}^{P}\int_{x_m-w_{mx}/2}^{x_m+w_{mx}/2}\int_{-\infty}^{\infty}\left\{\int_{-\infty}^{\infty}e^{-j(k_z'-k_z)z'}dz'\right\}\tilde{\overline{\overline{g}}}_E(x,y,k_z;x',y_m)\cdot\hat{z} \\
&\qquad e^{-jk_zz}I_{mp}\Psi_{mp}(x')\,dk_z\,dx'
\end{aligned} \tag{2.93}$$

The sifting property of the Fourier transform is now applied. The integral over z' is the Dirac delta function $\delta(k_z' - k_z)$. The integral over k_z is determined by considering the integrand's branch cuts and poles, which can only stem from $\tilde{\overline{\overline{g}}}_E$. Since $\tilde{\overline{\overline{g}}}_E$ is even, there are no branch cuts. The poles occur when k_z equals the propagation constants of the structure without the conducting strips, but these propagation constants are not equal to the propagation constants k_z' of the structure with the strips. The integral is then easily evaluated and the integral equation is

$$\bar{E} = \frac{-j\omega\mu e^{-jk'_z z}}{2\pi} \sum_{m=1}^{M} \sum_{p=0}^{P} \int_{x_m - w_{mx}/2}^{x_m + w_{mx}/2} \tilde{\bar{\bar{g}}}_E(x, y, k'_z; x', y_m) \cdot \hat{z}\, I_{mp} \Psi_{mp}(x')\, dx' \quad (2.94)$$

Application of Galerkin's technique as before enforces the boundary conditions on the conducting strips and gives a homogeneous system of equations

$$[0] = [Z][I] \quad (2.95)$$

The elements of the impedance matrix $[Z]$ are similar to those given by equation 2.81, but in the two-dimensional case, there is no z-dependence and G_{Ezz} is replaced by $\tilde{g}_{Ezz}$. The propagation constants for the structure are the eigenvalues of the system and are determined from the zeros of the determinant of $[Z]$.

In general, the propagation constant $\gamma = jk_z$ can be complex and is expressed in terms of the phase constant β and the attenuation constant α as $\gamma = \alpha + j\beta$. The calculation of the zeros of the determinant of $[Z]$ is discussed in the next chapter. Once the propagation constant is known, the fields for a given mode are calculated from the integral equation and, as shown below, the characteristic impedance is determined from the power carried by the propagating modes of the structure and the associated modal currents.

2.6.2 Characteristic Impedance

The characteristic impedance Z_c of a given mode in a structure is determined from a reciprocity-related characteristic impedance definition [12, 86], which is chosen because it converts the modal description of general, asymmetric multi-conductor systems into a form where the equivalent voltages and currents are compatible with external device models.

If the structure consists of N_c conductors (not including the shielding, which serves as ground), then the structure propagates N_c modes which have no cut-off frequencies. An $N_c \times N_c$ eigencurrent matrix $[I]$ can be defined, where the components I_{mk} of $[I]$ are the currents on line m for mode k, given by

$$I_{mk} = \sum_{p=0}^{P} \int_{\text{strip m}} I_{mpk} \Psi_{mpk}(x)\, dx \tag{2.96}$$

where I_{mpk} is the coefficient of equation 2.92 for the k^{th} mode. If an appropriate characteristic impedance Z_{mk} for line m and mode k is assumed to exist, then an $N_c \times N_c$ eigenvoltage matrix $[V]$ with components $V_{mk} = Z_{mk} I_{mk}$ may also be defined. The characteristic impedance is determined by including the orthogonality of the eigenvoltages and the eigencurrents:

$$V_k^T I_{k'} = \delta_{kk'}\, P_k \qquad k' = 1, N_c \tag{2.97}$$

where V_k is column k of $[V]$, $I_{k'}$ is column k' of $[I]$, $\delta_{kk'}$ is the Kronecker delta, and P_k is the total power carried by mode k. The power is given by the integral of the Poynting vector

$$P_k = \frac{1}{2} \iint_S \bar{E}_k \times \bar{H}_k^* \cdot \hat{z}\, dx\, dy \tag{2.98}$$

where $\bar{E}_k$ and $\bar{H}_k$ are the total electric and magnetic fields of mode k and S is the cross-section of the waveguide which is perpendicular to the direction of propagation. The integral equation 2.94 is used to determine $\bar{E}_k$, and $\bar{H}_k$ follows from Maxwell's equations.

A commonly used definition for the characteristic impedance is the power-current definition [30]. Practical characterization of asymmetric multi-conductor systems is not possible with this definition, but it is applicable to a structure which has a single conducting strip or a symmetric pair of coupled strips. In these cases, the reciprocity-related modal definition of characteristic impedance is equivalent to the power-current definition, which can be written as

$$Z_{mk} = \frac{2P_k}{N_c |i_{mk}|^2} \qquad m, k = 1, N_c \tag{2.99}$$

where $i_{11} = 1$ when $N_c = 1$ and $i_{11} = i_{12} = i_{21} = -i_{22} = 1$ when $N_c = 2$.

2.7 Mode Matching for the Analysis of Dielectric Waveguides

In chapter V, a monolithic dielectric waveguide is developed and characterized using a mode matching technique which is closely related to the theory which was discussed earlier. The mode matching method is simpler than the hybrid IEMM method, since neither an integral equation nor a Green's function is required.

The specific technique which is applied to the dielectric waveguide structures is quite similar to the method described in [17, 52, 68]. The general structure is modeled as a waveguide containing homogeneous rectangular dielectric regions, as in figure 2.1 with the conducting strips removed. As in section 2.4.1, the fields are determined using the vector potentials $\bar{A}$ and $\bar{F}$ and equations 2.14–2.15. The x-dependencies are exactly as before. The y-dependencies are chosen to satisfy the radiation condition at $y = \pm\infty$ if the walls at at $y = 0$ and $y = b$ are removed. In this configuration, laterally open structures can be characterized. The y-dependencies are

$$Y_l^{(j)}(y) = \begin{cases} \left. C_l^{(1)}\exp(jk_{yl}^{(1)}y) \right\} & \text{Section 1 w/o wall at } y = 0 \\ \left. \begin{array}{l} C_l^{(j)}\cos k_{yl}^{(j)}y \\ \quad +D_l^{(j)}\sin k_{yl}^{(j)}y \end{array} \right\} & \begin{array}{l} \text{Section 1 w/ wall at } y = 0, \\ \text{Sections 2–J-1, and} \\ \text{Section J w/ wall at } y = b \end{array} \\ \left. C_l^{(J)}\exp(-jk_{yl}^{(J)}y) \right\} & \text{Section J w/o wall at } y = b \end{cases} \tag{2.100}$$

Only two-dimensional structures are considered, and, since no Green's function is involved, the rigors of the Fourier transform are avoided by simply choosing the z-dependence to be

$$Z^E(z) = Z^M(z) = e^{-jk_z z} \tag{2.101}$$

The mode matching technique uses transmission matrices to relate the fields in adjacent sections. A simple transmission matrix relates the fields at one end of a section ($y = b^{(j-1)}$) to the fields at the other end ($y = b^{(j)}$). Scattering matrices are used in the IEMM formulation, but are not necessary here since the number of modes necessary for convergence is smaller than in the IEMM method. (Convergence is discussed in chapter III, and the scattering and transmission matrix formulations are briefly compared in section 2.4.3.) The fields in all sections are related by multiplying the transmission matrices and applying transverse resonance. A homogeneous system results, and the propagation constants $\gamma = \alpha + j\beta$ are determined by the zeros of the system determinant.

2.8 Summary

The formulations of the IEMM and mode matching techniques have been presented in this chapter. The IEMM technique was applied by creating a general model for three-dimensional strip-ridge structures and solving the spatial domain electric field integral equation with a Green's function-method of moments approach. The Green's function was determined by dividing the model into sections of layered parallel-plate waveguide and employing mode matching to enforce the boundary conditions at the interfaces between these waveguides. An appropriate Fourier transform provided a version of the IEMM method for two-dimensional strip-ridge structures. The well-known mode matching method for the characterization of dielectric waveguides was also outlined.

CHAPTER III

COMPUTATIONAL CONSIDERATIONS AND VALIDATION

The translation of the theory into a set of functional computer-aided modeling tools is divided into two parts. The first, computational considerations, addresses the solution of the transcendental equations for the x-directed wavenumbers, the storage and inversion of matrices, the calculation of the propagation constants of two-dimensional structures, the convergence of the infinite summations, and the efficiency of the code. The second part, validation, contains examples of the many software tests which ensured that accurate results were obtained.

3.1 Computational Considerations

3.1.1 Solution of the Transcendental Equation for the x-directed Wavenumbers

In both the IEMM and mode matching methods, the x-directed wavenumbers must be determined for each term in the layered parallel-plate waveguide's eigenfunction expansion. A structure which has only lossless materials is first considered, and the calculation of the wavenumbers in a structure with lossy materials is described at the end of this section.

The wavenumbers k_{xl} in each section of the lossless structure are determined by solving the transcendental equations which result from applying the boundary conditions at the layer interfaces (section 2.4.2). A nonlinear technique such as the Newton-Raphson method [60, ch. 9] solves these equations for as many wavenumbers as are required for mode matching. As is typical with such a method, initial approximations are necessary for accurate solutions. In the lossless case, neither the wavenumbers nor the transcendental equations are complex, and a direct search for the real and imaginary wavenumbers which satisfy the equations can be employed to determine the initial approximations. Two important issues arise when such a search is used. First, depending on the geometry and the internal parameters of the Newton-Raphson subroutine, the initial value might not be close enough to the actual value for the routine to return the desired wavenumber. For example, if the l^{th} wavenumber is needed and the initial value is too high, the routine will return the $(l+1)^{\text{th}}$ wavenumber. Second, the search is not guaranteed to detect all of the solutions in a given interval. Depending on the geometry, the tangent functions in equations 2.31 and 2.34 cause some of the poles and zeros to be so close to one another that a coarse search will not find all the wavenumbers. In practice, a very fine search (e.g., 30 000 points for each wavenumber) is required to avoid these problems. Even if the search does miss a wavenumber, the missing term in the mode matching summations causes an abnormally high condition number ($> 10^6$) in the matrix which is inverted to determine the generalized scattering matrices (equations B.29–B.32). The nonlinear solver is very efficient, often solving for each wavenumber in less than 10 iterations. On the other hand, the direct search is very time-consuming and, although the fineness of the search and the indirect evidence provided by the inflated condition number eliminate the possibility of omitting a wavenumber, a swift analytical method of finding the initial approximations for the wavenumbers is desirable.

The drawbacks of the direct search are removed by combining the search with an approximate technique for determining the eigenvalues. Since each section of the structure is a section of parallel-plate waveguide, the x-directed wavenumbers in a given section can be determined from the propagation constants of the corresponding parallel-plate waveguide which is infinite in the y- and z-directions. The dispersion equation for the j^{th} section's parallel-plate waveguide is

$$\left(k_{xl}^{(ij)}\right)^2 = \left(k^{(ij)}\right)^2 + \left(\gamma_{\text{PP}l}^{(j)}\right)^2 \tag{3.1}$$

where $\gamma_{\text{PP}l}^{(j)}$ is the propagation constant of the l^{th} mode of the parallel-plate waveguide, and, as in chapter II, $k^{(ij)}$ is the material wavenumber of the i^{th} layer in the j^{th} parallel-plate waveguide. Propagating modes are characterized by $\left(\gamma_{\text{PP}l}^{(j)}\right)^2 < 0$ and evanescent modes by $\left(\gamma_{\text{PP}l}^{(j)}\right)^2 > 0$. The propagation constants are approximated in numerical order starting with the dominant mode by using the Rayleigh-Ritz procedure for layered rectangular waveguides [15, ch. 6] and adapting it for layered parallel plate-waveguides, as was done for TE$_x$ modes in [80]. In short, the Rayleigh-Ritz procedure determines approximate eigenfunctions and eigenvalues for the layered waveguide with a variational integral whose stationary values correspond to the actual eigenvalues when suitable eigenfunctions are used in the integrand. A particularly convenient set of eigenfunctions comprises functions which are sums of the homogeneous waveguide eigenfunctions (i.e., $\cos l\pi/a$ for TE$_x$ modes and $\sin l\pi/a$ for TM$_x$ modes). When the L^{th} approximate eigenfunction is formed from a sum of the first L homogeneous waveguide eigenfunctions, an $L \times L$ real symmetric matrix eigenvalue problem is formed. This system is easily solved for the first L values of $\left(\gamma_{\text{PP}l}^{(j)}\right)^2$ with Householder reduction and a QR algorithm [60, ch. 11]. Each approximate value of $\left(\gamma_{\text{PP}l}^{(j)}\right)^2$ is an upper limit on the actual value, and, in view of the above dispersion equation, the associated approximate value of $\left(k_{xl}^{(ij)}\right)^2$ is also an upper limit on the actual value. The approximate values are further refined by searching along the real or imaginary axis in the appropriate direction with minimal computation time, and accurate values are then determined by the non-linear solver.

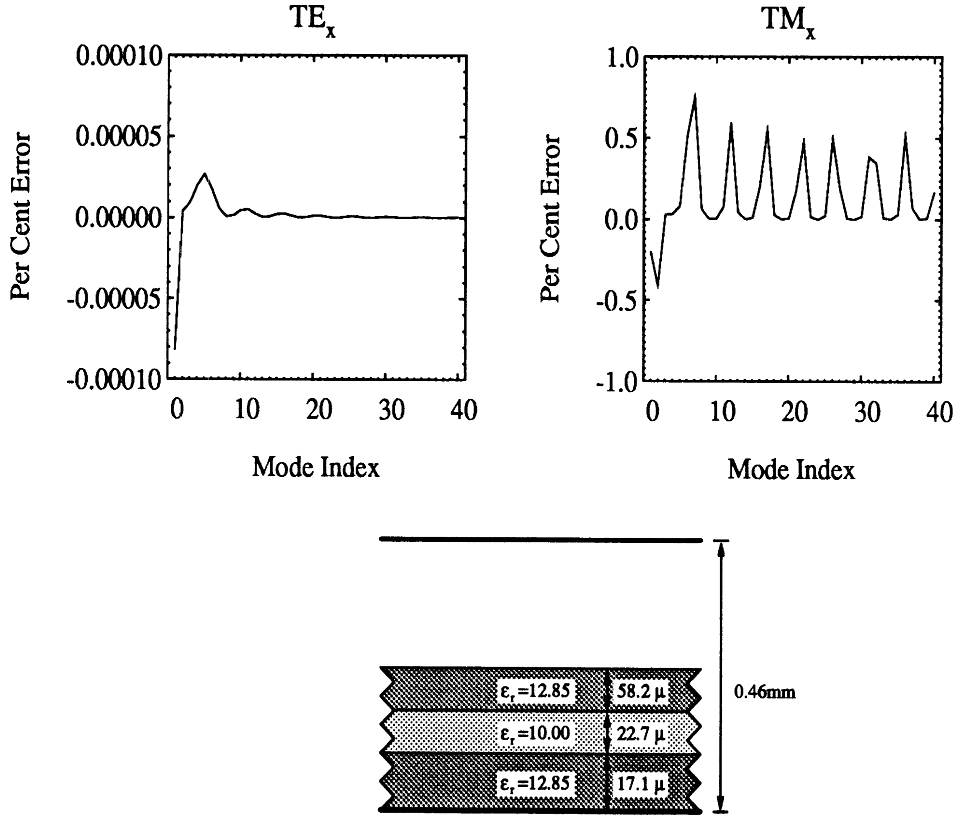

Figure 3.1: Percent error in the Rayleigh-Ritz calculations of the x-directed TE$_x$ and TM$_x$ wavenumbers for a four-layered parallel-plate waveguide.

A comparison between the Rayleigh-Ritz results and the actual results is given in figure 3.1 for the first 40 modes of a four-layered parallel-plate waveguide. The error is negative when the wavenumbers are imaginary and positive when the wavenumbers are real. Since the approximate eigenfunctions are sums, the procedure is more accurate with more terms. For this example, the wavenumbers were calculated from a 160×160 matrix eigenvalue problem. The approximate and actual values are essentially equal for the TE$_x$ modes and differ by less than 1.0% for the TM$_x$ modes. The reason for the difference is directly related to the boundary conditions at the layer interfaces. All of the TE$_x$ fields are continuous across each layer interface, since the electric fields are parallel to the interfaces and the permeability of each layer is μ_o. The x-components of the electric fields in the TM$_x$ modes are discontinuous across each interface due to the difference in permittivity between layers. The Rayleigh-Ritz procedure is valid in either case, but the approximate eigenfunctions require many more terms to accurately describe the step-discontinuity of the x-components of the TM$_x$ electric fields. The error is greatest for those modes where the x-component of the electric field is strongest.

When the dielectric materials are lossy and the section is inhomogeneous, the x-directed wavenumbers are complex and determined iteratively. In each iteration, the losses in each layer are slightly incremented, and the initial approximations given to the nonlinear solver are the wavenumbers from the previous iteration. For the lossy structures in this work, an increment of $0.01\epsilon'$ for ϵ'' enabled the nonlinear solver to find the correct wavenumbers. The first iteration uses the lossless wavenumbers as initial approximations, and the process ends when the losses in the layers have been incremented to the desired values. The nonlinear solver is the Newton-Raphson method for two variables (i.e., the real and imaginary parts) [34; 60, ch. 9]. When the section is homogeneous, the x-directed wavenumbers are always real (i.e., $l\pi/a$) and independent of dielectric losses.

3.1.2 Matrix Storage and Inversion in the IEMM Method

As shown in the previous chapter, the IEMM method relies heavily on matrix algebra. Several options are available for the storage and inversion of the matrices. The goal of this work is not to break new ground in this area but to apply well-established methods in order to minimize storage requirements and run-times and allow for convenient implementation.

The size of each matrix in the Green's function calculation depends on the numbers of terms used in the summations, and the storage requirements depend on how the summations are ordered. Let the transverse and longitudinal modes be numbered from $l = 1, \ldots, L$

and $n = 1, \ldots, N$ so that there is a total of (LN) modes. Either the sum over l is performed N times or the sum over n can is performed L times; in other words, two choices are available for numbering the modes:

$$(1,1),(1,2),\ldots,(1,N);\ \ (2,1),(2,2),\ldots,(2,N);\ \ \ldots;\ \ (L,1),(L,2),\ldots,(L,N) \quad (3.2)$$

and

$$(1,1),(2,1),\ldots,(L,1);\ \ (1,2),(2,2),\ldots,(L,2);\ \ \ldots;\ \ (1,N),(2,N),\ldots,(L,N) \quad (3.3)$$

Because of the orthogonality between longitudinal modes, the first choice leads to banded matrices and the second choice leads to block diagonal matrices. The block diagonal form is preferable because the Green's function can be determined by solving N separate $L \times L$ systems, rather than handling one large $(LN) \times (LN)$ system.

The three-dimensional IEMM method requires several matrix inversions: one inversion to calculate the generalized scattering matrices (appendix B); two inversions to calculate each reflection coefficient matrix (equation 2.66); one inversion to calculate the Green's function (equations C.9–C.10); and one inversion of the moment method impedance matrix (equation 2.82) to determine the currents on the conducting strips. In general, the matrices are full, so direct solvers, rather than iterative methods, are considered [18]. Of the direct solvers, LU-decomposition is chosen for its efficiency and ability to invert a matrix which is not part of a system of equations wherein the right-hand side is known [60, ch. 2].

The above discussion also applies to the two-dimensional IEMM method, except there is no inversion of the method of moments impedance matrix, and the number of $L \times L$ systems which must be solved is not N but instead depends on the number of iterations required to determine the propagation constant (section 3.1.3).

3.1.3 Propagation Constant Calculations

The propagation constants of a two-dimensional strip-ridge structure are calculated from the zeros of the determinant of the impedance matrix of equation 2.95. When the structure is lossless, a propagating mode has an imaginary propagation constant, an evanescent mode has a real propagation constant, and complex modes exist in pairs with complex conjugate propagation constants of opposite sign [56]. The determinant is either real or imaginary in the former cases, and complex in the latter. As in the calculation of the x-directed wavenumbers (section 3.1.1), the Newton-Raphson method is used to solve the nonlinear equation. Again, initial approximations for the propagation constants are required.

When propagating or evanescent modes are sought, the simplest method of determining the initial approximations for a new structure is to plot the determinant as a function of the propagation constant. Because the determinant does not vary rapidly, very coarse plots (10 points per k_o) are sufficient. When the frequency or geometry is varied, educated guesses based on past results can be used. Two facts are useful in making these guesses. First, if the structure has N_c conducting strips, then N_c modes propagate at all frequencies, i.e., N_c modes do not have cutoff frequencies [12]. Second, the determinant has poles when the propagation constant coincides with a propagating mode of the structure when the conducting strips are not present (section 2.6.1). The initial approximation must not have a pole between it and the actual value, or the nonlinear solver will not find the correct propagation constant.

When complex modes are sought, a plot of the determinant as a function of the propagation constant is impractical, since the propagation constant is complex and the plot must cover the complex plane. Initial approximations must be obtained from *a priori* knowledge, which can be gained by examining the evanescent and propagating modes over frequency.

A complex mode, if one exists, is located by finding the point where two evanescent or propagating modes merge together and disappear over a frequency interval. If the two modes are propagating modes, the phase constant of the complex mode at a frequency point just after the point where the modes disappear is very close to the phase constant of the two propagating modes, and the attenuation constant is very small. Similarly, if the two modes are attenuating modes, the attenuation constant of the complex mode at a frequency point just after where the modes disappear is very close to the attenuation constant of the two evanescent modes, and the phase constant is very small. Once the complex mode is found, it can be traced by slowly varying the frequency. In this work, complex modes have only a minor role—these modes carry reactive power and are included in the mode diagrams of chapter VI only for completeness.

In the lossy case, an iterative procedure similar to the one described for the x-directed wavenumbers is used.

Similar considerations apply to the calculation of the propagation constants of a dielectric waveguide structure from the zeros of the matrix generated by the mode matching method.

3.1.4 Convergence

A comprehensive treatment of the convergence of the IEMM and mode matching methods is desirable, but this type of study is beyond the scope of this work. If convergence were examined, methods for accelerating the convergence of the infinite summations would first be considered, and expressions for the upper limits of the summations and criteria for the discretization of the conducting strips would then be sought. The magnitude of the study is compounded by the dependence of the convergence on the desired quantity; for example, as shown below, the propagation constant of a strip-ridge structure is accurately determined with fewer terms than the characteristic impedance. The geometry of the structure, the operating frequency and the required accuracy are also factors to be considered.

In place of an arduous and exhaustive study, this work, like many other implementations of numerical methods, includes convergence data which are representative of the specific structures which are characterized. Although data is not shown for each and every structure, similar tests assured that convergent results were obtained in all cases.

Mode Matching Method

In chapter V, dielectric waveguides are analyzed by the mode matching method, and the convergence of this technique when it is applied to these structures is demonstrated in figure 3.2. Curves are shown at two frequencies, which are near the upper and lower extremities of the structure's bandwidth. At the low end of the frequency range, the dielectric waveguide width w is thinnest with respect to wavelength and sufficient terms to model the interaction between the two mode matching planes must be included. At the upper frequency, the dielectric waveguide is wider, but the layers are thicker; less terms are needed to account for the interaction between mode matching planes but more terms are needed to satisfy the boundary conditions at each plane.

The number of terms required for convergence is somewhat higher than reported in previous applications of mode matching to hybrid millimeter-wave dielectric waveguides, where convergence was found with less than 14 terms (i.e., 7 TE_x and 7 TM_x terms) in the field expansion in a given section of the structure [17, 52, 68]. The difference occurs because the dielectric waveguides of chapter V have widths which are considerably narrower than those of the hybrid waveguides, and the interaction between mode matching planes is thus much stronger in the former structures.

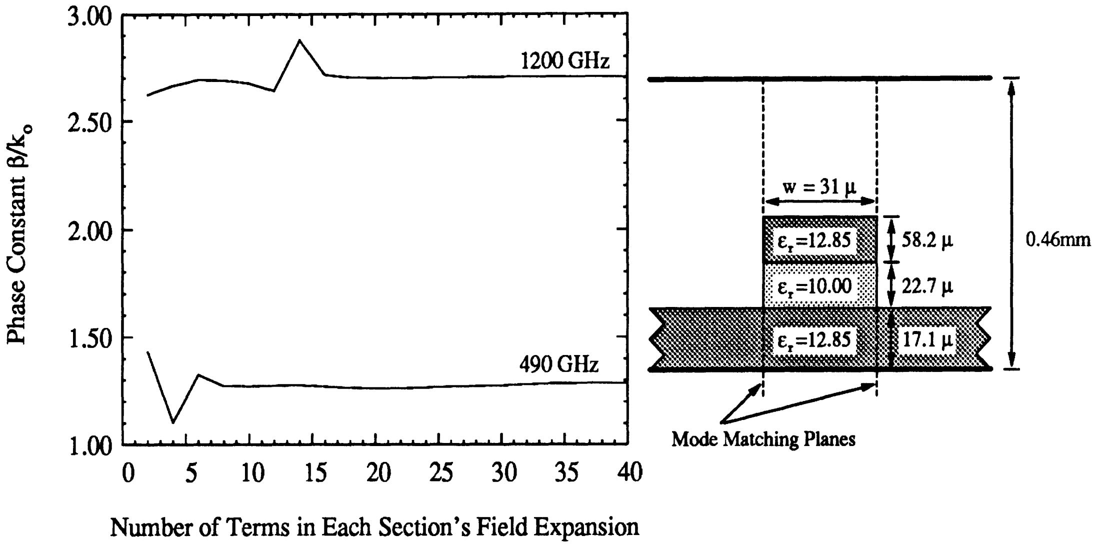

Figure 3.2: Convergence of the propagation constant of a dielectric waveguide structure (chapter V). Equal numbers of TE$_x$ and TM$_x$ modes are used in each field expansion.

Two-dimensional IEMM Method

The convergence examples for the two-dimensional IEMM method consider one of the more complicated structures in this work—the microstrip with a finite substrate and ground plane of figure 3.3. The structure has two different planes of conductors and two different conductor widths. The convergence of the phase constant and characteristic impedance is demonstrated in figure 3.4[1]. These data demonstrate that, as alluded to earlier, the convergence properties depend on the quantity of interest—the convergence of the phase constant is much swifter than that of the characteristic impedance. The convergence of the attenuation constant is similar to that of the phase constant.

---

[1] The microstrip with finite substrate and ground plane is studied in [67] with a different definition of characteristic impedance. Because these results were used to help validate the code, the characteristic impedance results shown in figure 3.4 use this definition, rather than the reciprocity-related definition in section 2.6.2. Both definitions rely on the propagated power, and the convergence behavior of the definitions are very similar.

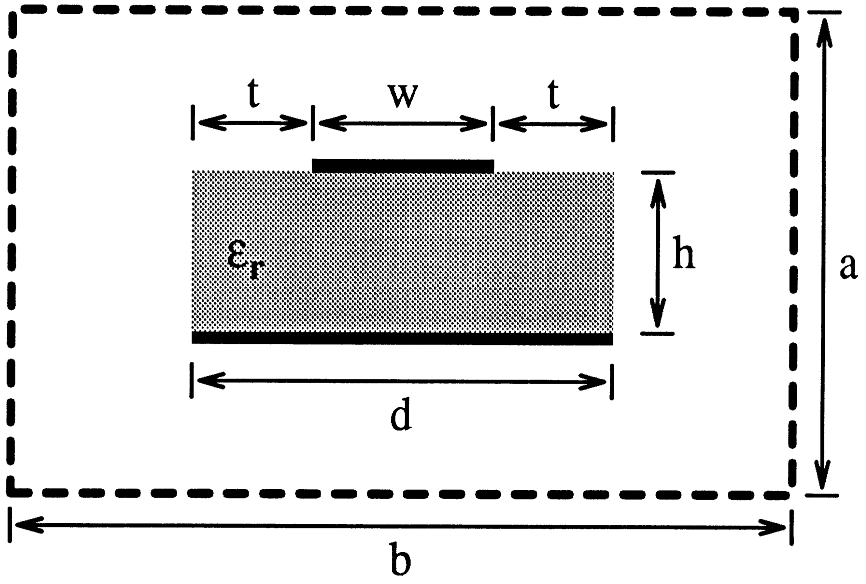

Figure 3.3: Microstrip with finite substrate and ground plane. The shielding waveguide is large enough so that its presence does not affect the results.

Three-dimensional IEMM Method

The currents on a discontinuous conducting strip are calculated with the three-dimensional IEMM method, and the quantity required for circuit modeling is the current input reflection coefficient Γ_{in} looking into the discontinuity. The structure which is studied in chapter VI is a conducting strip on top of a dielectric waveguide (figure 3.5), and the convergence of Γ_{in} for this structure is examined while varying the numbers of terms in the eigenfunction expansions and the discretization of the conducting strip in figures 3.6 and 3.7. The plots have relatively small scales ($< 10^{\circ}$). The first plot shows that the longitudinal and transverse summations are well-converged with 500 and 280 terms, and the second plot shows that Γ_{in} is accurate to within 0.5° when the strip is divided in > 200 subsections. The corresponding sampling rate is 30 per guided wavelength.

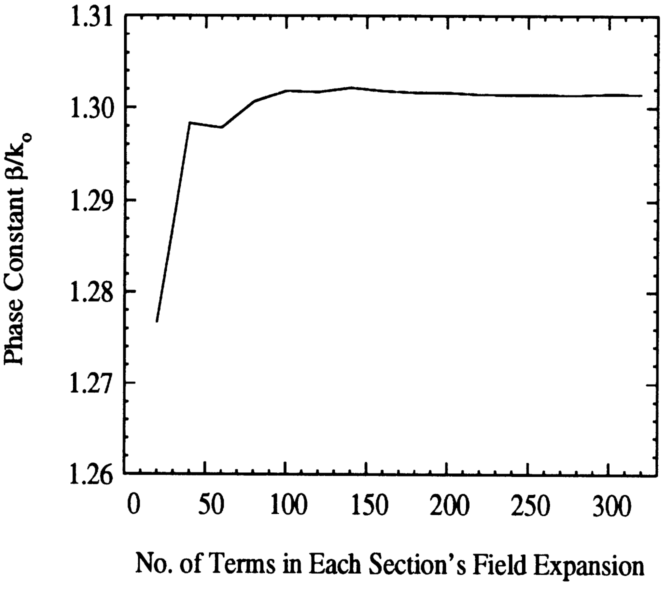

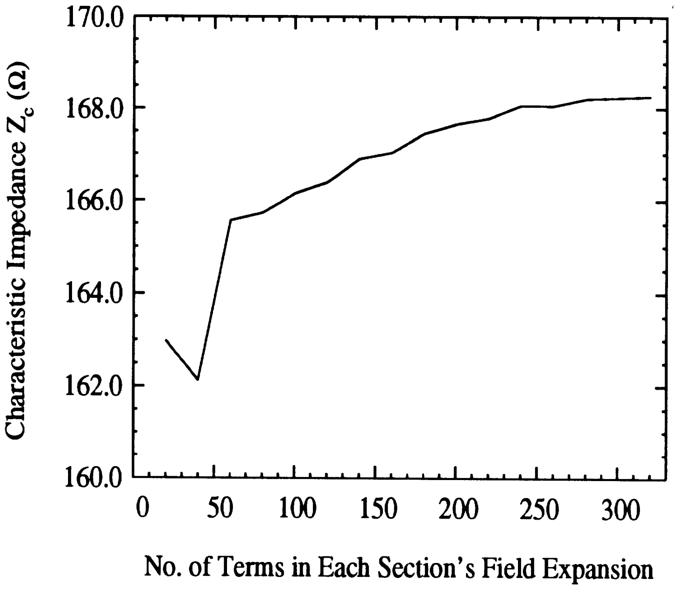

Figure 3.4: Convergence data for the dominant microstrip mode in the structure of figure 3.3 with $t/w = 0.25$, $w/h = 0.5$, $\epsilon_r = 2.5$, $d = 1.5$mm, $a = b = 13.5$cm, and frequency = 3.0GHz.

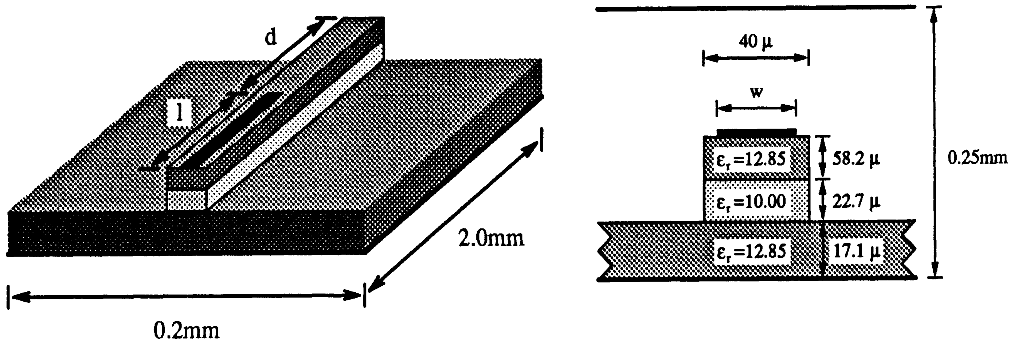

Figure 3.5: Conducting strip on a dielectric waveguide for the convergence study of the three-dimensional IEMM method; in the following figures, d = 1.0mm. The structure is shielded by a perfect electric conductor on all sides. Chapter VI includes an in-depth study of this structure.

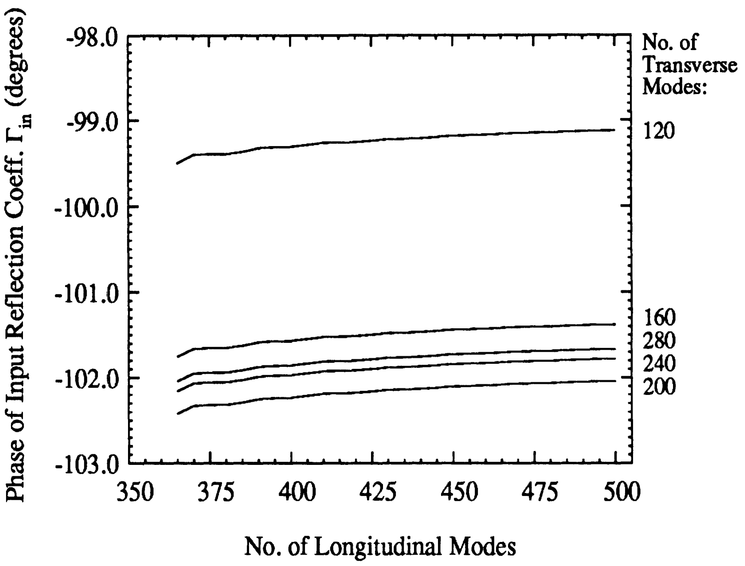

Figure 3.6: Phase of the current input reflection coefficient as a function of longitudinal modes when various numbers of transverse modes are used. There are 183 samples on the conducting strip. The geometry is given in figure 3.5.

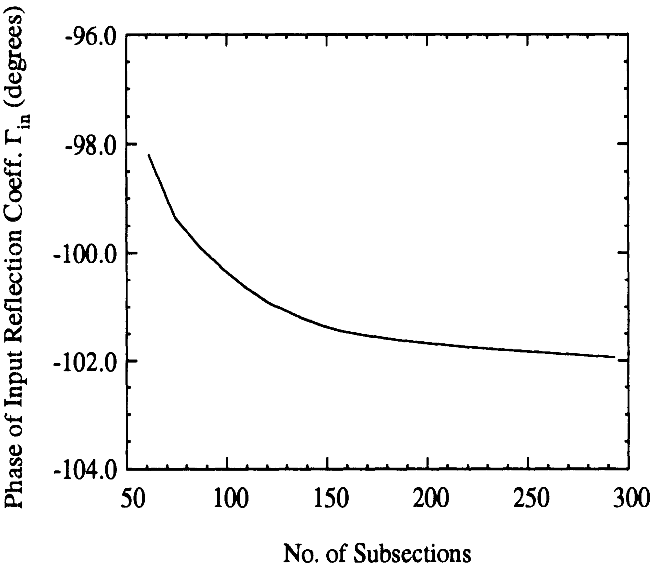

Figure 3.7: Convergence of the phase of the current input reflection coefficient vs. number of samples on the conducting strip, at 510 GHz with 600 longitudinal modes and 280 transverse modes. The geometry is given in figure 3.5.

3.1.5 On the Efficiency of the Code

As with many numerical techniques, the efficiencies of the IEMM and mode matching methods are highly dependent on the speed and memory of the workstation, the operating frequency, and the geometry of the structure. The CPU time required by the integral equation portion of the code depends on the conductor geometry, and the time required by the mode matching depends on the dielectric geometry. As discussed in the previous section, a detailed study of convergence could decrease run-times considerably; and, although considerable effort was expended toward generating efficient code, the algorithms could undoubtedly be improved further.

The efficiency of the code when the current version is run on a recently released workstation is quantified in table 3.1. Because of the ongoing rapid development of the engineering workstation, the run-times will undoubtedly be obsolete within one or two years; the main purposes of the table are to give users some insight as to run-times for specific calculations relative to one another and to highlight those portions of the code which would benefit most from improved efficiency. The state of the code as of this writing can be summarized as follows: the mode matching method is easily usable in real-time design and analysis; the two-dimensional IEMM code can perform frequency sweeps in overnight runs and is practical although not optimal; and the three-dimensional IEMM code is rather slow, requiring multiple overnight runs for each frequency point. The bulk of the CPU time is expended in matrix inversions and multiplications, each of which use $\sim L^3$ operations. Inversion methods other than the LU-decompositions might yield better efficiency; also, methods such as unrolling loops and blocking [7] can be applied to speed up matrix multiplications, but these methods are machine-dependent and are sometimes performed by the compiler when the code is optimized. Improving the efficiency of the IEMM method requires more study and development, and an important point of this discussion is that these CPU times reflect the current state of the code and do not reflect any fundamental limit on the efficiency of the method.

3.2 Validation

3.2.1 Mode Matching Method

The mode matching software for dielectric waveguides was validated by comparing with the numerical and experimental results given in [17, 52, 68]. Examples are given in figures 3.8–3.9.

3.2.2 Two-dimensional IEMM Method

The IEMM software for two-dimensional structures was validated first for simple microstrip and coupled microstrip. Many results for these common structures are available in the literature. Results for the effective dielectric constant ($\equiv (\beta/k_o)^2$) of coupled microstrip as obtained from the IEMM method are shown in figure 3.10. The agreement with results from formulas based on a full-wave spectral-domain hybrid-mode method [44] is within the

METHOD	CALCULATION	SPECIFICATIONS	APPROXIMATE RUN-TIME
Mode Matching, Two- and Three-Dimensional IEMM	Transverse Eigenvalues (k_x)		5 per min.
Mode Matching	Propagation Constant (γ)	30 terms	5 min. (with manual root search)
Two-Dimensional IEMM	Propagation Constant (γ)	200 terms; times are per iteration; usually $<$ 10 iterations	2 min. per section interface, plus 5 min. for combining sections and moment method
Two-Dimensional IEMM	Characteristic Impedance	280 terms	10 min. per section interface, plus 10 min. for combining sections and moment method
Three-Dimensional IEMM	Mode Matching	200 trans. terms; times are per long. term; e.g., 400 long. terms were used for structure of chapter VI	2 min. per section interface, plus 5 min. for combining sections and moment method
Three-Dimensional IEMM	Integral Equation (solve for current)	500 subsections	15 min.

Table 3.1: Typical run-times on an HP9000/720 workstation.

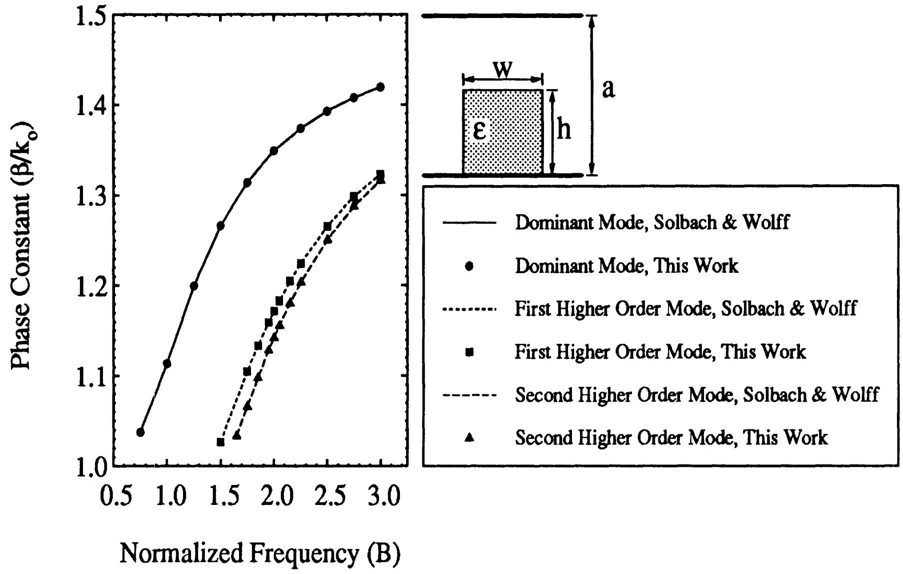

Figure 3.8: Phase constant β/k_o vs. normalized frequency B, compared to the results of Solbach and Wolff [68]. $\epsilon = 2.22\epsilon_o$, $h = 4.100$mm, $w = 4.095$mm, $a = 19.680$mm, $B = 2k_oh\sqrt{\epsilon/\epsilon_o - 1}/\pi$, $k_o = \omega\sqrt{\epsilon_o\mu_o}$.

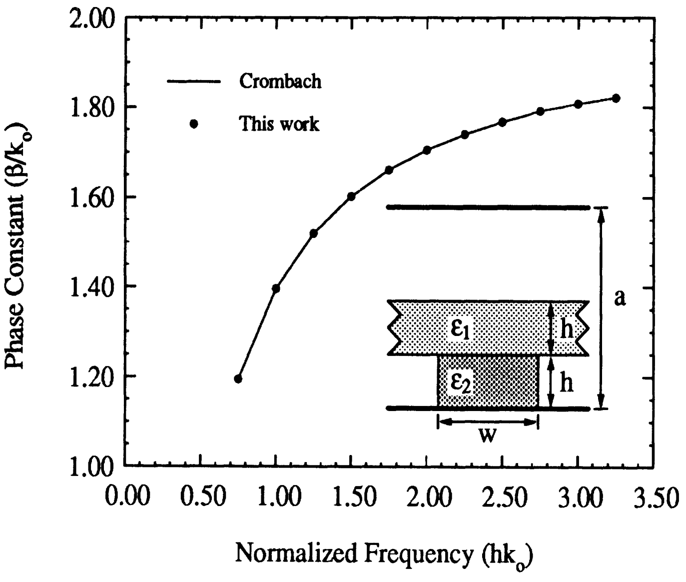

Figure 3.9: Phase constant β/k_o of the lowest order mode with odd symmetry vs. normalized frequency hk_o, compared to Crombach's results [17]. $\epsilon_1 = 3.8\epsilon_o$, $\epsilon_2 = 2.1\epsilon_o$, $h = 3.33$mm, $w = 8.40$mm, $a = 20.00$mm.

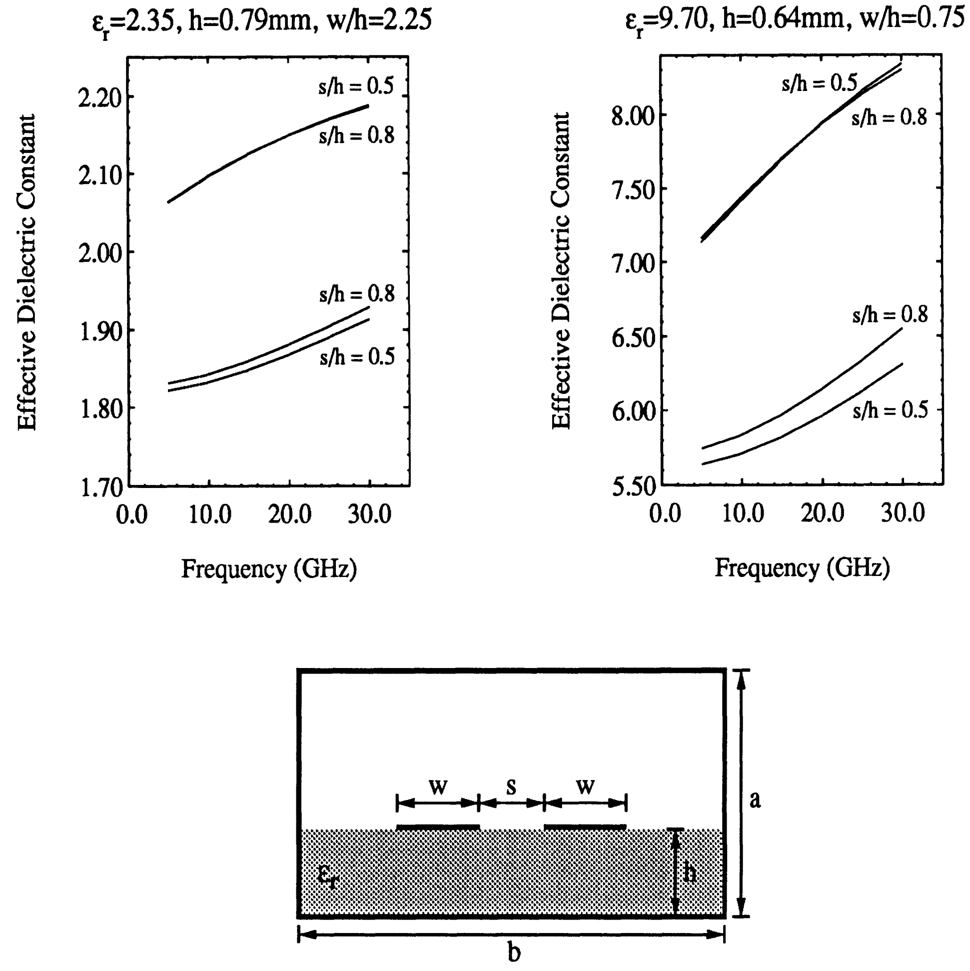

Figure 3.10: IEMM results for the effective dielectric constant of coupled microstrip. $b = 2a = 2.0$cm.

±0.5% range of error given by the reference.

The code was further validated by calculating the propagation constant as a function of frequency for a microstrip near a chip edge and comparing to results obtained from both the method of lines and experiment [74] (figure 3.11). The data are generally in good accord, except for a slight offset between the two theoretical curves. The probable cause of the variation is the inability to exactly recreate the conditions given in [74]; very slight changes in d, w, ϵ_r and frequency are sufficient to bring the curve into even better agreement with the given experimental data.

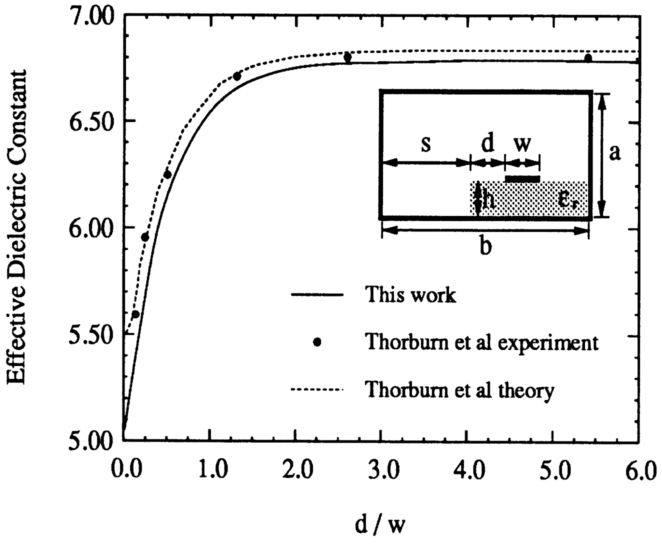

Figure 3.11: Comparison of effective dielectric constant results from this work to theory and measurement by Thorburn *et al* [74] for microstrip near a chip edge. Referring to the inset, $\epsilon_r = 10.2$, $w = 0.925$mm, $h = 1.27$mm, $a = 50.0$mm, $b = 35.0$mm, $s = 15.0$mm, and frequency = 2 GHz.

Results obtained from the IEMM method for the characteristic impedance of a microstrip near a chip edge are compared to quasi-static results obtained using the rectangular boundary division method [90] in figure 3.12. Agreement to within 2% is obtained, and the small difference is attributed to the non-TEM nature of the fields which is not included in the quasi-static method but is fully taken into account by the IEMM technique.

The code was also validated for a structure where the conductors are not coplanar. The structure, a microstrip with a finite substrate and ground plane, is shown in figure 3.3. The shielding is present so that the IEMM method can be applied, but it is large enough so that its presence does not affect the results. Comparisons of results from the IEMM method to results from a quasi-static integral equation method [67] for the unshielded structure are given in figure 3.13[2]. The plots show phase constant and characteristic impedance results for the dominant transmission line mode of the structure when the substrate and ground plane widths are equal to the width of the conducting strip ($t/w = 0.00$) and when the

---

[2] See footnote 1 in section 3.1.4.

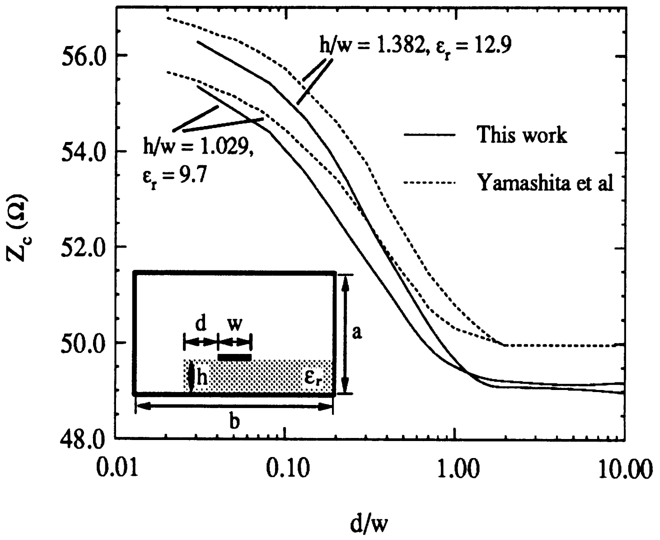

Figure 3.12: Comparison of characteristic impedance results from this work to results by Yamashita *et al* [90] for microstrip near a chip edge. The center of the strip is aligned with $b/2$, $w = 1.0\text{mm}$, $a = b = 27.6\text{mm}$, and frequency = 3 GHz.

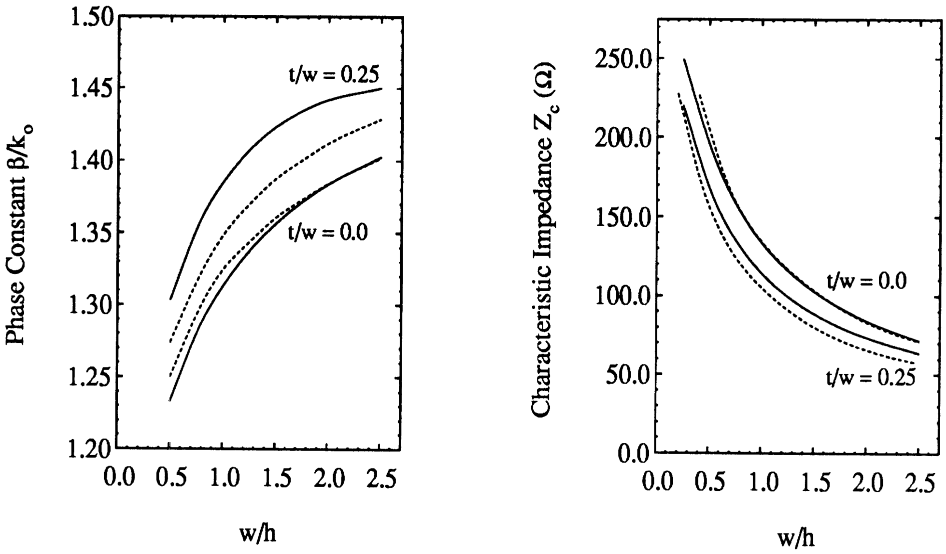

Figure 3.13: Phase constant and characteristic impedance vs. w/h for the structure of figure 3.3 with $t/w = 0.0$ and $t/w = 0.25$, $\epsilon_r = 2.5$, $d = 1.5\text{mm}$, $a = b = 13.5\text{cm}$, and frequency = 3.0GHz. Full-wave IEMM results: ——; quasi-static results [67]: - - -.

substrate and ground plane widths are 50% wider than the conducting strip ($t/w = 0.25$). In the former case, the two methods of analysis are in excellent agreement. In the latter case, the two methods are within 3% for the phase constant results and differ by 5% at small w/h and by 10% at larger w/h for the characteristic impedance results. The full-wave IEMM analysis accurately accounts for the non-TEM fields propagating in the structure; these fields have a larger effect on the characteristic impedance when $t/w = 0.25$.

Coupled microstrip with an etched groove are studied in chapter IV, and results for this structure were validated with another independent technique, the finite difference-time domain (FDTD) method [4, 21, 93]. This method calculates the frequency associated with a phase constant, and the result of using phase constants determined by the IEMM method at 94 GHz as input to the FDTD method is shown in table 3.2. The maximum difference between the expected and FDTD values was less than 2.5%.

The code which accounts for dielectric losses was validated by comparing to experimental [36] and numerical [46] results for metal-insulated-semiconductor transmission lines. A sample of this validation is shown in figure 3.14.

3.2.3 Three-Dimensional IEMM Method

Validation of the three-dimensional IEMM method is closely related to the validation of the two-dimensional version. Since the mode matching portion of the code was extensively validated, only the portion of the code which accounts for the extension to three-dimensional structures needs to be considered. This portion of the code solves the integral equation with the method of moments and was validated by comparing with previously published characterizations of various shielded microstrip discontinuities. An example of the excellent agreement which was obtained is given in figure 3.15, which compares with experimental and numerical results from [22].

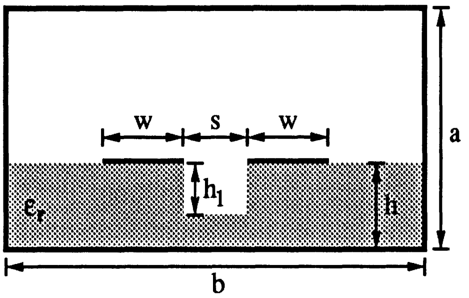

GROOVE DEPTH h_1 (μm)	EVEN MODE		ODD MODE	
	FDTD FREQUENCY (GHz)	PERCENT ERROR	FDTD FREQUENCY (GHz)	PERCENT ERROR
0.0	93.498	-0.53	94.136	0.14
20.0	92.705	-1.38	94.148	0.16
40.0	92.230	-1.88	93.521	-0.51
60.0	91.918	-2.21	93.261	-0.79
80.0	91.793	-2.35	93.210	-0.84
100.0	91.838	-2.30	93.273	-0.77

Table 3.2: FDTD frequency results from 94 GHz IEMM data. Geometry of two microstrips with a groove etched between them: $w = 0.1$mm, $h = 0.1$mm, $d = 0.05$mm, $a = 1.3$mm, $b = 2.51$mm, and $\epsilon_r = 12.85$.

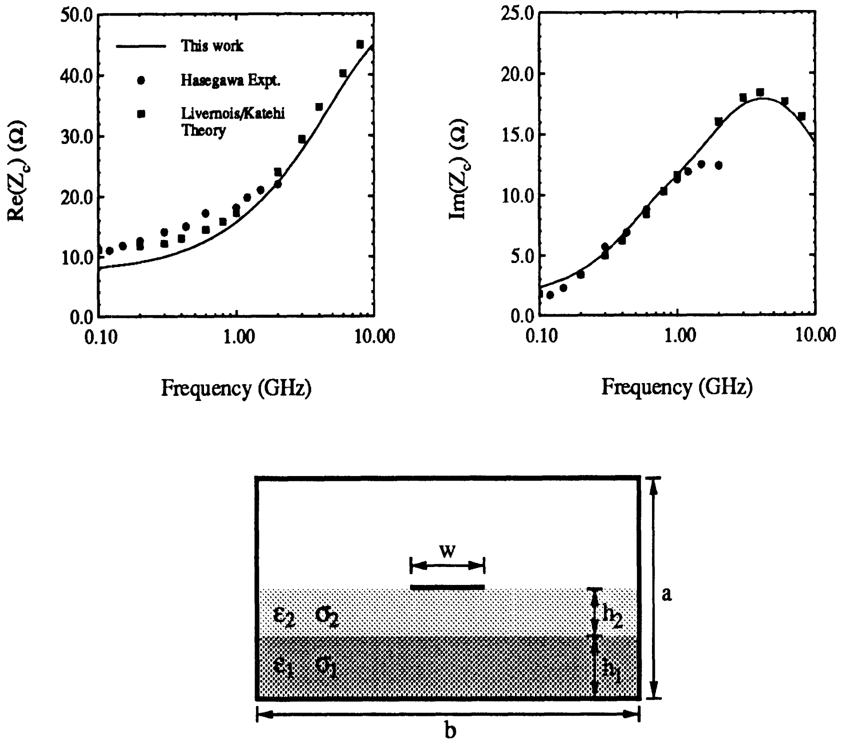

Figure 3.14: Characteristic impedance of MIS transmission line, compared to the experimental results of Hasegawa *et al* [36] and the numerical results of Livernois and Katehi [46]. $\epsilon_1 = 12.0\epsilon_o$, $\sigma_1 = 0.05(\Omega\text{-cm})^{-1}$, $\epsilon_2 = 4.0\epsilon_o$, $\sigma_2 = 0.0(\Omega\text{-cm})^{-1}$, $h_1 = 250.0\mu\text{m}$, $h_2 = 1.0\mu\text{m}$, $w = 160.0\mu\text{m}$.

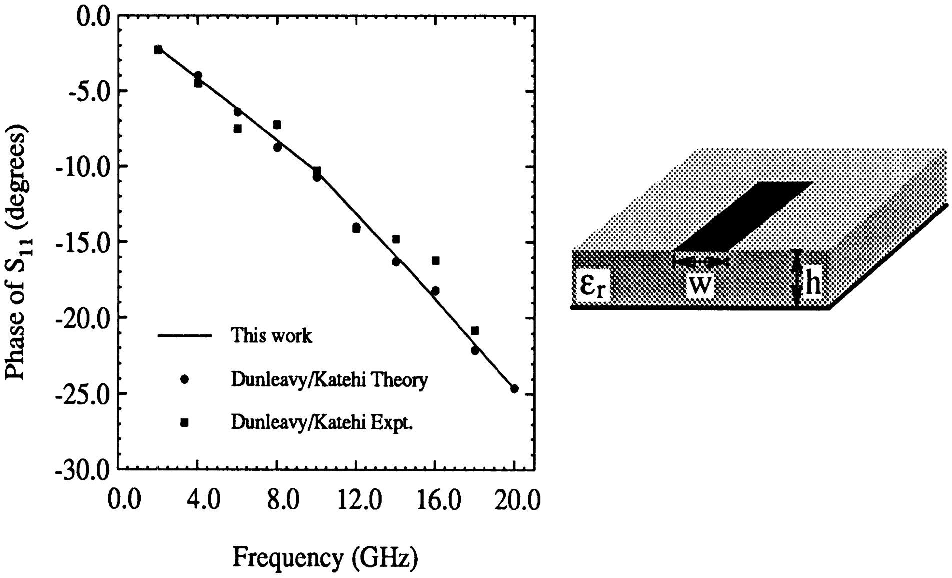

Figure 3.15: IEMM method results compared to Dunleavy and Katehi's results [22] for a shielded microstrip open end discontinuity. $w = h = 0.635$mm, $\epsilon_r = 9.7$, and the cavity has width = height = 6.35mm and length = 50.8mm.

3.3 Summary

Computational considerations and validation of the mode matching and the two- and three-dimensional IEMM methods have been discussed in this chapter. The solution of the transcendental equations for the x-directed wavenumbers was accomplished with the aid of the Rayleigh-Ritz method, which provided an ordered set of initial approximations for the nonlinear solver. The storage and inversion of matrices in the three-dimensional IEMM method were optimized by appropriately ordering the summations. The key to swift calculation of the propagation constants of two-dimensional structures is the choice of initial approximation, and the procedure for making this choice was described. Examples of the convergence of the infinite summations were presented. The efficiency of each of the three numerical methods was quantified with the caveat that these data do not represent the fundamental limits of the techniques. Validation of the methods was established by comparisons with independent experimental and numerical results.

CHAPTER IV

CHARACTERIZATION OF TWO-DIMENSIONAL STRIP-RIDGE STRUCTURES

Strip-ridge structures, first discussed in Chapter I, are found in a variety of VLSI applications as well as in hybrid and monolithic microwave, millimeter-wave, and sub-millimeter-wave integrated circuits. Studies of coupled microstrip on ridges, coupled microstrip with an etched groove, microstrip with finite substrate and ground plane, coupled multilevel microstrip with a finite intermediate dielectric layer, and an electro-optic modulator structure with an etched groove are presented in this chapter. The propagation constant and the characteristic impedance are the quantities of primary interest in frequency domain results, and these quantities are used in the calculation of another useful frequency domain quantity, the coupling coefficient, and in the time domain analysis. The details of the coupling coefficient calculation and the time domain analysis are given in the next two sections, and the characterizations of the various strip-ridge structures are in the succeeding sections.

4.1 Coupling Coefficient

The coupling between two lines in a symmetric structure is quantified with the coupling coefficient k_c, given by [62] as the square root of the ratio of the coupled power to the incident power. Since there are two conductors in the structure (not counting the shielding), the structure propagates two modes which do not have cut-off frequencies (section 2.6.2).

The coupling coefficient k_c is given by

$$k_c = \frac{1}{2}(\Gamma_e - \Gamma_o) \tag{4.1}$$

where

$$\Gamma_e = \frac{j(\bar{Z}_{ce} - \bar{Z}_{ce}^{-1})\sin\beta_e l}{2\cos\beta_e l + j(\bar{Z}_{ce} + \bar{Z}_{ce}^{-1})\sin\beta_e l} \tag{4.2}$$

$$\Gamma_o = \frac{j(\bar{Z}_{co} - \bar{Z}_{co}^{-1})\sin\beta_o l}{2\cos\beta_o l + j(\bar{Z}_{co} + \bar{Z}_{co}^{-1})\sin\beta_o l} \tag{4.3}$$

$$\bar{Z}_{ce} = \frac{Z_{ce}}{Z_o} \tag{4.4}$$

$$\bar{Z}_{co} = \frac{Z_{co}}{Z_o} \tag{4.5}$$

$$Z_o = \sqrt{Z_{ce}Z_{co}} \tag{4.6}$$

and Z_{ce} and Z_{co} are the even- and odd-mode characteristic impedances; β_e and β_o are the even- and odd-mode phase constants; and the length l of the coupler is taken to be one-quarter of the average of the even- and odd-mode wavelengths. The length is chosen so that the coupling coefficient reflects the maximum coupling between the two lines.

4.2 Time Domain Analysis

Propagation of an excitation in the time domain on the structures is characterized by transforming the excitation to the frequency domain, utilizing an equivalent circuit model to evaluate the response at each frequency point [13], and transforming back to the time domain. Switching between the time and frequency domains is accomplished using a discrete fast fourier transform [60, ch. 12]. The equivalent circuit model considers the modes of a system of terminated transmission lines as equivalent decoupled lines of unit characteristic impedance (figures 4.1–4.2). The voltage and current on the k^{th} equivalent line are

$$v_k(z) = a_k^+ e^{-\gamma_k z} + a_k^- e^{\gamma_k z} \tag{4.7}$$

$$i_k(z) = a_k^+ e^{-\gamma_k z} - a_k^- e^{\gamma_k z} \tag{4.8}$$

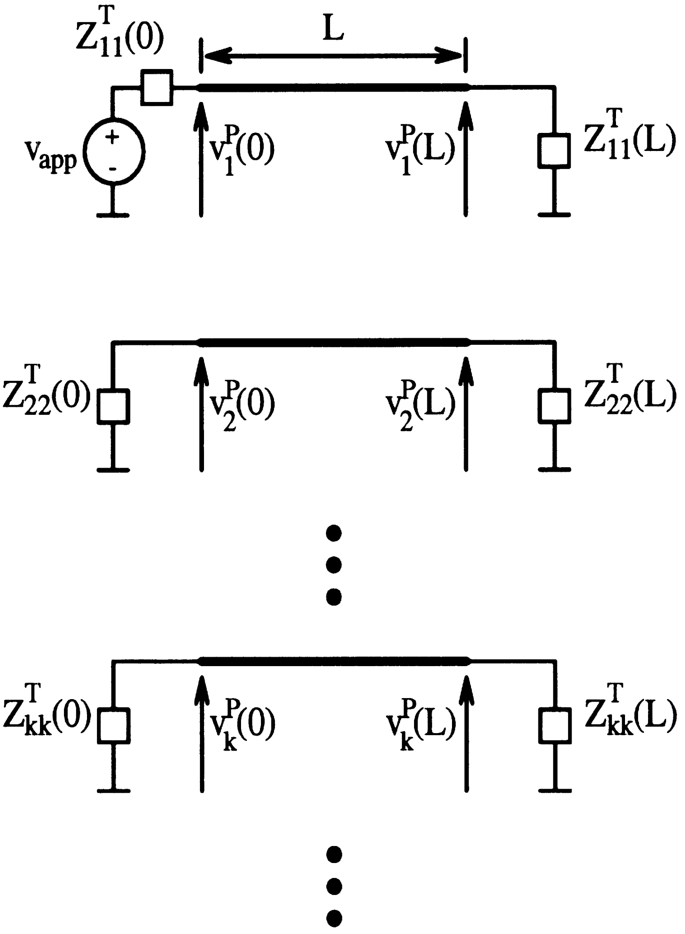

Figure 4.1: The system of terminated transmission lines for the time domain model. Adapted from [13].

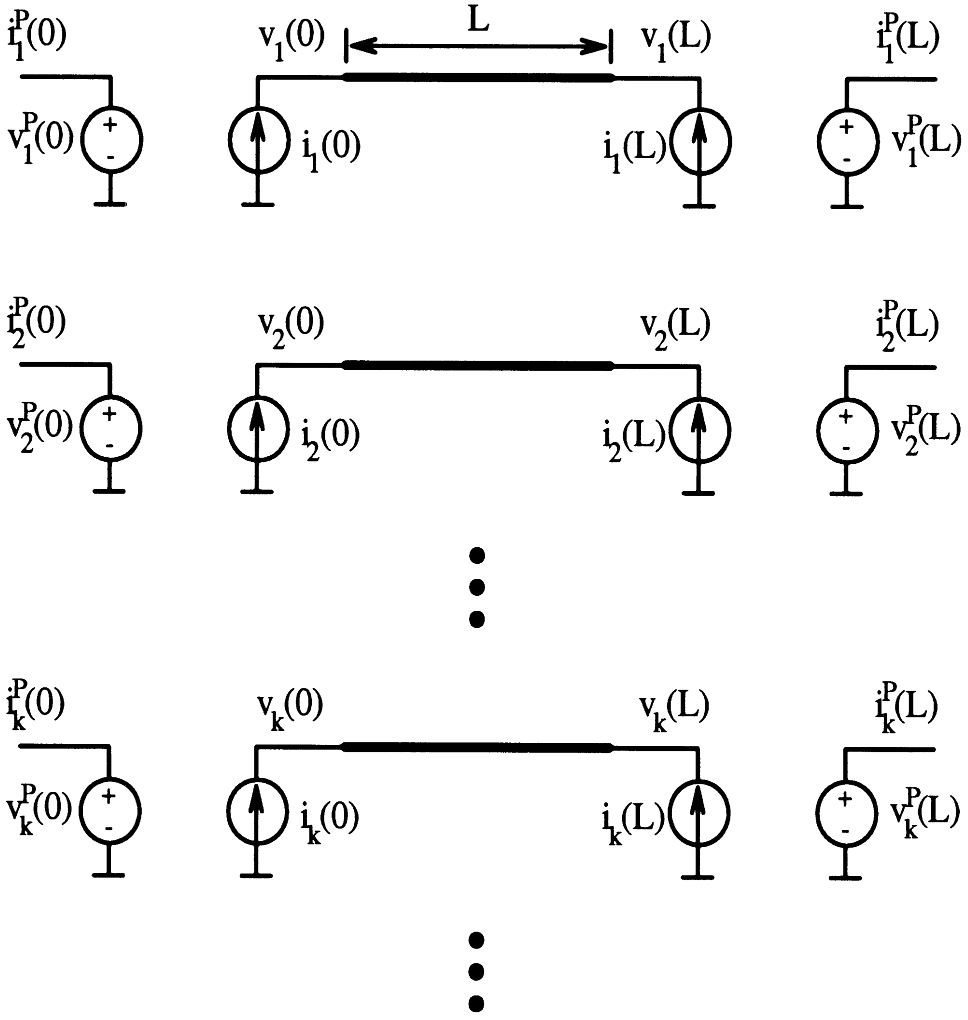

Figure 4.2: The equivalent circuit for the time domain analysis models the modes of the system in figure 4.1 as equivalent decoupled lines of unit characteristic impedance. The physical voltages and currents are v_k^P and i_k^P, the equivalent voltages and currents are v_k and i_k, and these quantities are related by the coupling matrices $[V]$ and $[I]$. Adapted from [13].
]

The spatial variation of the equivalent voltages and currents for the k^{th} mode is described by the propagation constant γ_k, which is calculated from the IEMM analysis, and by two coefficients a_k^+ and a_k^-. The equivalent quantities are related to the physical quantities through coupling matrices $[V]$ and $[I]$ which depend on the modal coefficients I_{mk} of the physical currents (equation 2.96) and the modal characteristic impedances Z_{mk} (section 2.6.2), i.e.,

$$v^P(z) = [V]\, v(z) \tag{4.9}$$

$$i^P(z) = [I]\, i(z) \tag{4.10}$$

where v^P and i^P are vectors whose m^{th} elements are the total physical voltage and current on the m^{th} conductor, $v(z)$ and $i(z)$ are vectors whose k^{th} elements are the equivalent voltage and current $v_k(z)$ and $i_k(z)$, and the mk^{th} elements of $[V]$ and $[I]$ are $Z_{mk}I_{mk}$ and I_{mk}. The coefficients a_k^+ and a_k^- are determined by the boundary conditions at the terminations, which are

$$v_{\text{app}} - v^P(0) = [Z^T(0)]\, i^P(0) \qquad z = 0 \tag{4.11}$$

$$v^P(L) = [Z^T(L)]\, i^P(L) \qquad z = L \tag{4.12}$$

where v_{app} is a vector whose m^{th} element is the excitation at the termination of the m^{th} line and $[Z^T(0)]$ and $[Z^T(L)]$ are diagonal matrices whose m^{th} elements are the terminating impedances of the m^{th} line at $z = 0, L$. At a given frequency, v_{app}, $[Z^T]$, γ_m and Z_{mk} are known, a_k^+ and a_k^- are determined by using equations 4.9–4.10 in equations 4.11–4.12, and the responses $v^P(z)$ and $i^P(z)$ are then determined from equations 4.9–4.10.

4.3 Coupled Microstrip on Dielectric Ridges

The geometry of two coupled microstrip on dielectric ridges is given in figure 4.3; the structure is characterized in figures 4.4–4.5 and 4.7–4.8. The first plot illustrates the behavior of the even- and odd-mode phase constants for different spacings over the frequency range 85–105 GHz. The next three plots show the phase constants β, characteristic

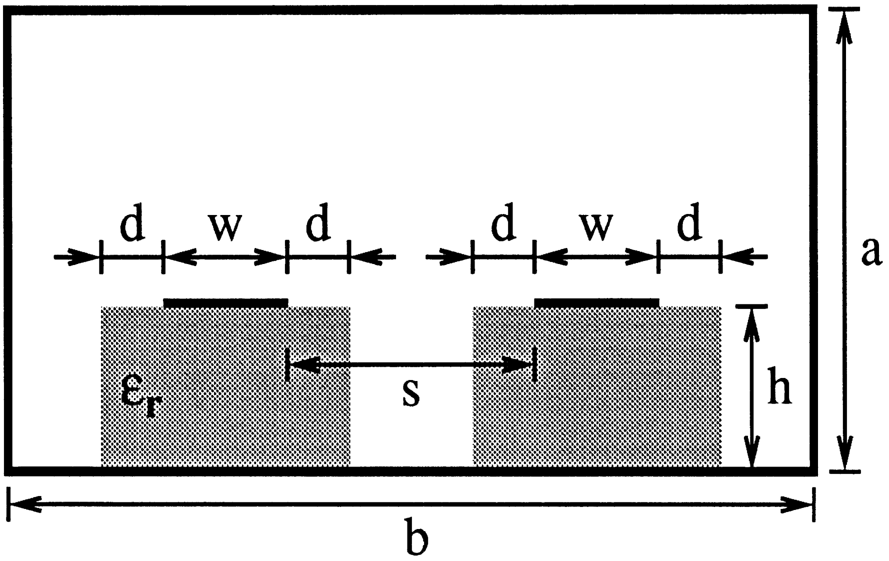

Figure 4.3: Geometry of two coupled microstrip on dielectric ridges: w = 0.1mm, h = 0.1mm, d = 0.05mm, a = 1.3mm, b = 2.51mm, and ϵ_r = 12.85.

impedances Z_c, and coupling coefficient k_c at 94 GHz as a function of spacing for strips on ridges and on a continuous substrate.

Typical of coupled lines, the even-mode phase constants generally decrease and the odd-mode phase constants generally increase with increasing spacing (figures 4.4–4.5)— i.e., as the lines become farther apart, the even and odd modes decouple and the phase constants tend toward the single-strip value. However, in this case, for $100\mu\text{m} < s < 150\mu\text{m}$, the odd-mode phase constant *decreases* before it begins to increase. At $s = 100\mu\text{m}$, the ridges are contiguous and the strips are together on a single ridge; the range $100\mu\text{m} < s < 150\mu\text{m}$ is a transition region between the case of two strips on a single ridge and the case of two strips on two ridges.

The transition region in the odd-mode β-s curve is qualitatively understood by placing an electric wall half-way between the two strips (figure 4.6), considering either the left or right half of the structure, and applying quasi-static analysis [32]. The odd-mode phase

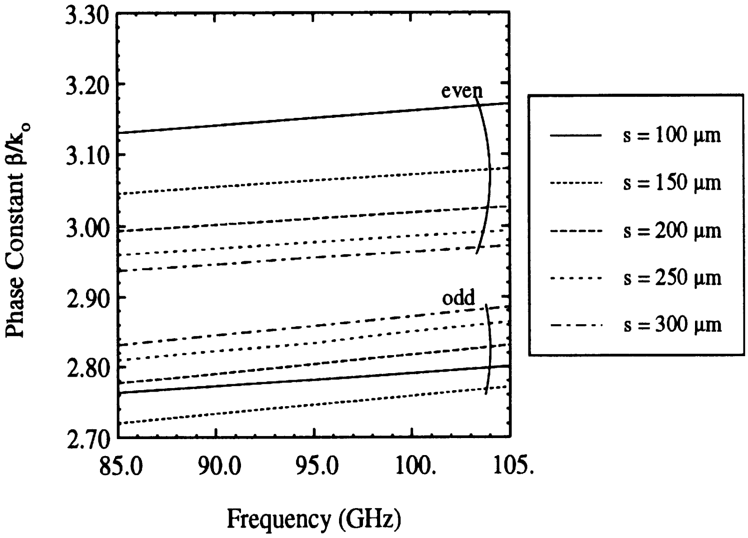

Figure 4.4: Phase constant β vs. frequency at various spacings s for the structure described in figure 4.3.

constant depends on the total capacitance from one of the strips to ground:

$$\beta_o/k_o \;=\; \left(\frac{C_o}{C_o^a}\right)^{1/2} \tag{4.13}$$

where

$$C_o \;=\; C_p + C_{fa} + C_{fd} + C_{ga} + C_{gda} \tag{4.14}$$

and C_o^a is calculated like C_o when $\epsilon_r = 1$. The capacitance C_{gda} between one of the strips and the electric wall through the dielectric ridge and the air gap between the two ridges is sharply decreased when the air gap increases from zero width, just as adding an air gap in a dielectric-filled parallel plate capacitor decreases its capacitance. This decrease in C_{gda} is reflected by the decrease of the odd-mode phase constant in the transition region. As the air gap increases, this capacitance becomes less significant compared to the other capacitances between the strip and ground and the odd-mode β-s curve more closely resembles that of conventional coupled microstrip.

The data demonstrate that as the spacing between strips increases, the strips on the ridges decouple faster than the strips on the continuous substrate. The β-s and Z_c-s

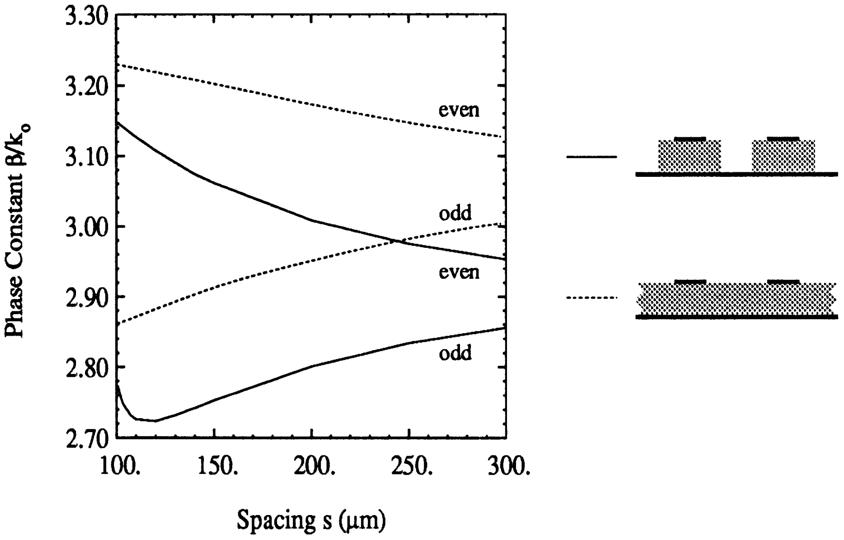

Figure 4.5: Phase constant β vs. spacing s at 94 GHz for microstrip on dielectric ridges (figure 4.3) and microstrip on continuous substrate (figure 4.3, with the two ridges replaced by a single substrate which extends over the entire width of the structure).

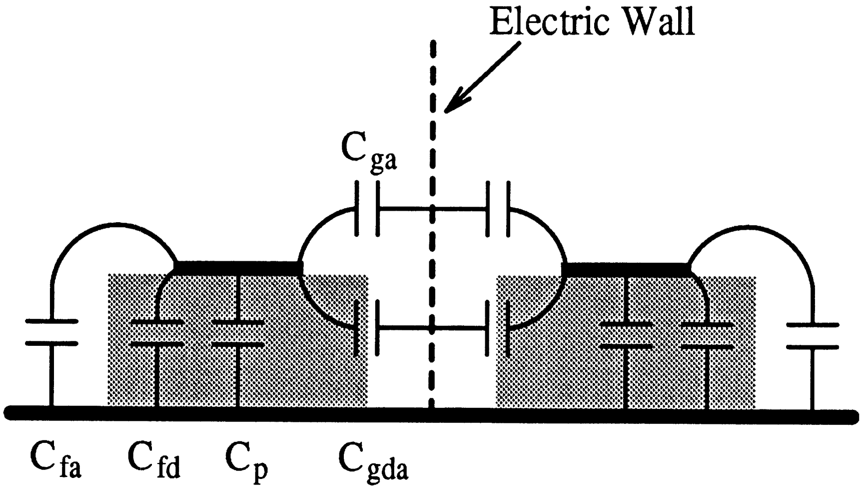

Figure 4.6: Capacitances associated with the odd mode of the symmetric coupled microstrip on dielectric ridges of figure 4.3. C_p is the parallel-plate capacitance between the strip and the ground plane, and C_{fa}, C_{fd}, C_{ga} and C_{gda} are various fringing capacitances.

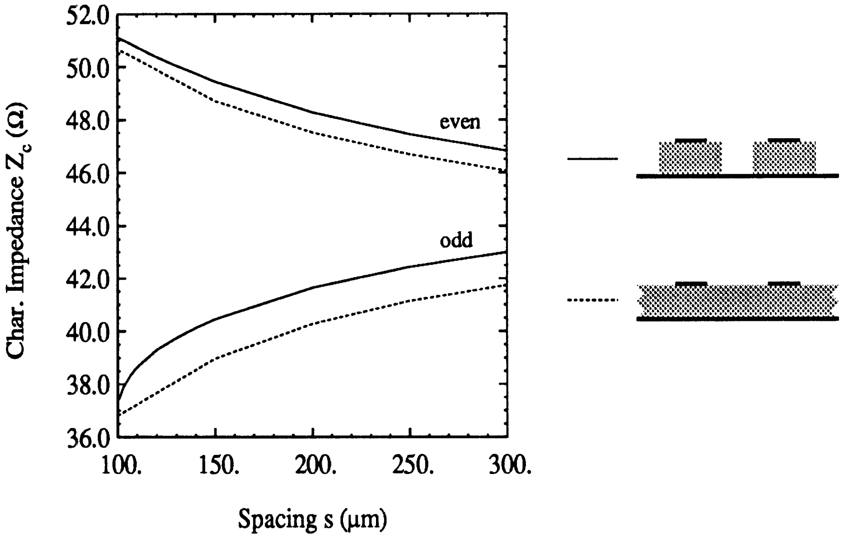

Figure 4.7: Characteristic impedance Z_c vs. spacing s at 94 GHz for microstrip on dielectric ridges (figure 4.3) and microstrip on continuous substrate (figure 4.3, with the two ridges replaced by a single substrate which extends over the entire width of the structure).

curves for the coupled microstrip on ridges converge to the values for a single strip on a ridge faster than the β-s and Z_c-s curves for the strips on the continuous substrate converge to the values for a single microstrip on a continuous substrate. In addition, the coupling coefficient of the strips on the ridges falls off more rapidly with spacing than does the coupling coefficient of microstrip on a continuous substrate. When increased packing density is desirable, structures of this type can be used in place of conventional microstrip.

The coupling coefficient curves include data for the limiting case of ridges with widths equal to the widths of the conducting strips. At $s = 100\mu$m, the strips on the wider ridges are on one ridge, and the coupling is the same as for microstrip on a continuous substrate. As s increases, the coupling of the strips on the wider ridges tends toward that of the strips on the narrower ridges. The transition between the case of strips on a continuous substrate and strips on individual ridges over the range $100\mu\text{m} < s < 150\mu\text{m}$ is again apparent.

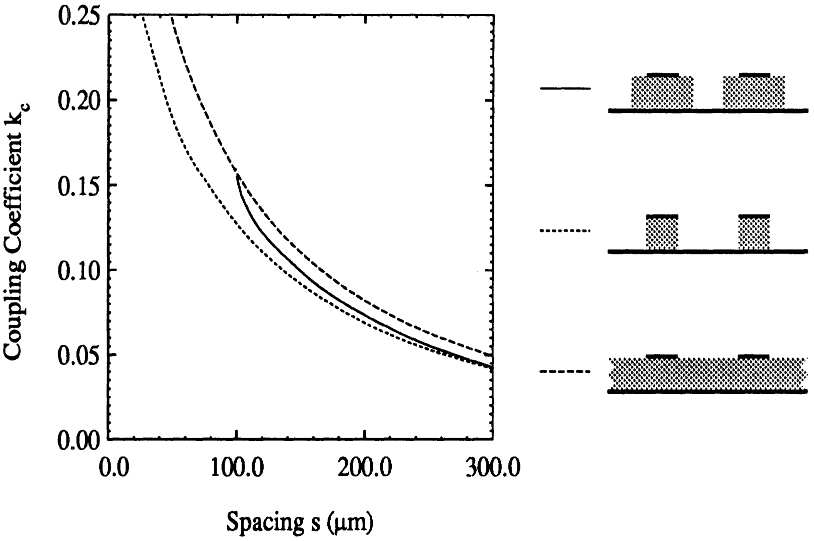

Figure 4.8: Coupling coefficient k_c vs. spacing s at 94 GHz for microstrip on dielectric ridges (figure 4.3), microstrip on narrower dielectric ridges (figure 4.3, with $d = 0$), and microstrip on continuous substrate (figure 4.3, with the two ridges replaced by a single substrate which extends over the entire width of the structure).

4.4 Frequency Domain Study of Coupled Microstrips with an Etched Groove

A structure which is closely related to microstrip on ridges is coupled microstrip with an etched groove (figure 4.9). The effects of groove depth on the propagation and coupling characteristics of the structure at 94 GHz are shown in figures 4.10–4.12.

The plots of the even- and odd-mode phase constants versus groove depth (figure 4.10) show that the phase constants decrease rapidly with increasing groove depth at shallow groove depths, with the odd-mode phase constant decreasing more rapidly. As the groove depth becomes comparable to the substrate height, the decreases of the phase constants become slower and more alike. The odd-mode characteristic impedance also shows rapid change at shallow groove depths. Significant effects on the propagation occur when even a very shallow groove is added; the coupling coefficient versus groove depth plot in figure 4.12 shows that marked decoupling occurs over the range $0\mu\text{m} < h_1 < 20\mu\text{m}$.

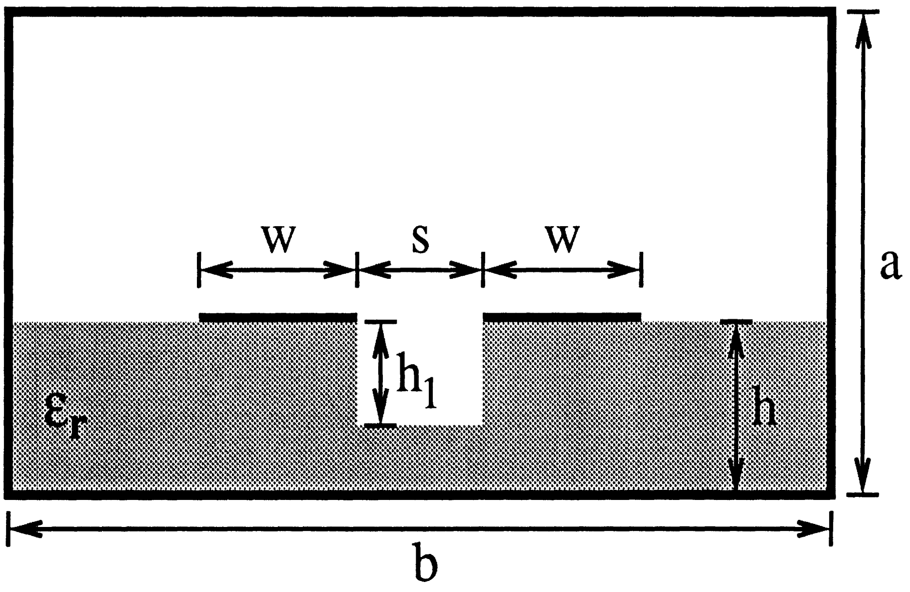

Figure 4.9: Geometry of two microstrips with a groove etched between them: $w = 0.1$mm, $h = 0.1$mm, $d = 0.05$mm, $a = 1.3$mm, $b = 2.51$mm, and $\epsilon_r = 12.85$.

Figure 4.11 shows that the even- and odd-mode characteristic impedances are most dissimilar at very shallow and very deep groove depths, suggesting that the coupling coefficient k_c has a minimum value at intermediate groove depths. Figure 4.12 substantiates that k_c has such a minimum and shows that the minimum occurs when the groove depth h_l is between 50μm and 60μm. The plot also shows that the minimum exists over a wide frequency range (1–94 GHz). Since the time domain characteristics of the structure depend on the steady-state characteristics of the structure over such a frequency range, the minimum in coupling indicates that the crosstalk in the time domain between two microstrips can be decreased by adding a groove. This possibility is explored in the next section.

4.5 Time Domain Study of Coupled Microstrips with an Etched Groove

Pulse propagation on the structure when $h_l = 0\mu$m and $h_l = 50\mu$m is illustrated in figures 4.13– 4.15. In each case, the line lengths were 2.54cm, and the lines were excited

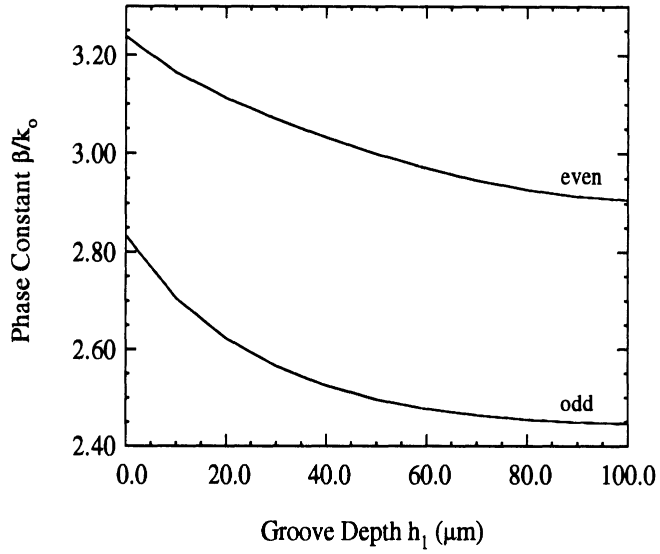

Figure 4.10: Phase constant β vs. groove depth h_l at 94 GHz for coupled microstrip with an etched groove (figure 4.9).

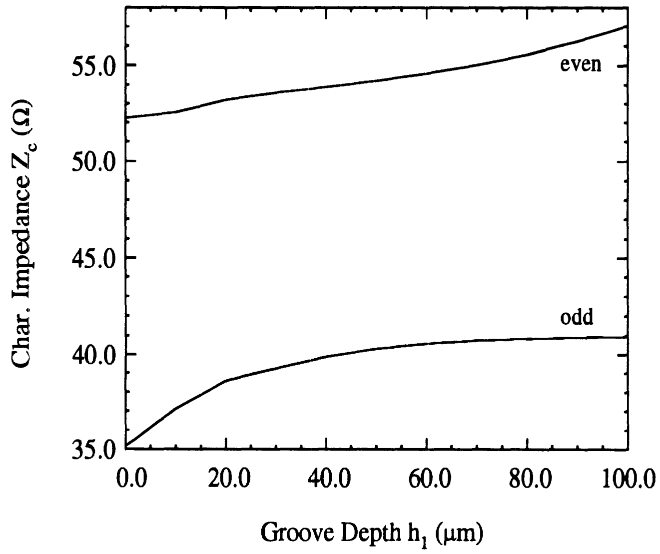

Figure 4.11: Characteristic impedance Z_c vs. groove depth h_l at 94 GHz for coupled microstrip with an etched groove (figure 4.9).

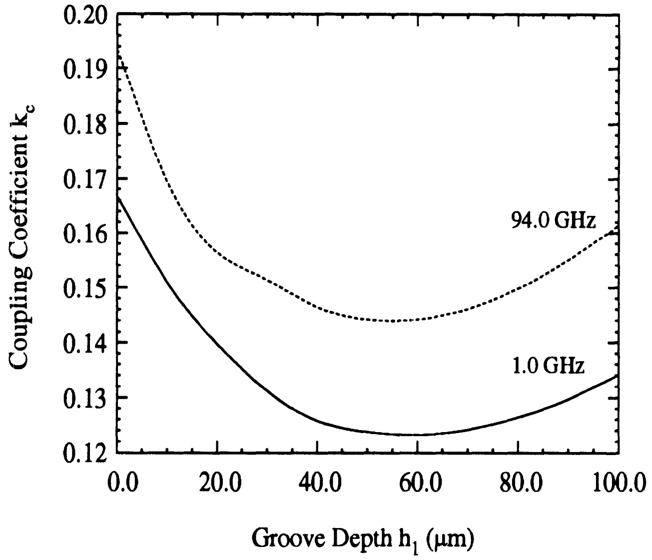

Figure 4.12: Coupling coefficient k_c vs. groove depth h_l at 1 and 94 GHz for coupled microstrip with an etched groove (figure 4.9).

at one end of one of the lines, i.e., the "near end" of the "active line." The pulse had a duration of 1.0ns, rise and fall times of 0.1ns, an amplitude of 1.0V, and a period of 10.0ns. Each end was terminated with 43.0Ω, which is the characteristic impedance of a single conducting strip on the substrate shown in figure 4.9 with $h_l = 0\mu$m. Independent of groove depth, the pulse on the active line undergoes no noticeable dispersion, since no losses are included and since the propagation constant is nearly constant at frequencies up to the maximum significant frequency component necessary for the construction of the pulse.

Associated with the rise and fall of the pulse on the active line, relatively short pulses of low but opposite amplitudes are present at the near end of the "sense line" (i.e., the line without the source). When the front of the pulse leaves the near end of the active line, the rise of the first pulse is induced at the near end of the sense line. Before the end of the pulse leaves the near end, the front of the active-line pulse has already returned from the far end, and the drop of the first sense-line pulse is induced. A steady state is

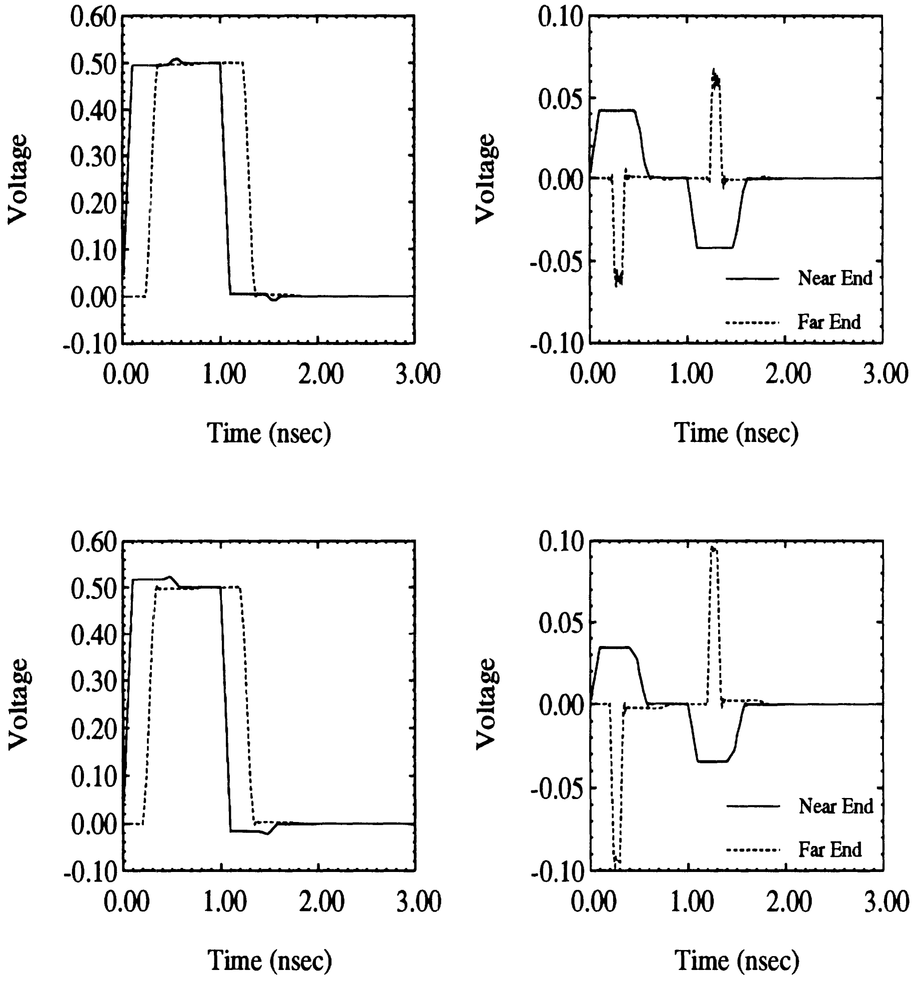

Figure 4.13: Propagation of a pulse on coupled microstrip with no etched groove (top) and with an etched groove of depth $h_1 = 50\mu m$ (bottom). The geometry is given in figure 4.9. Left—active line; right—sense line.

achieved while the active-line pulse is being sent, and there is no coupled signal during this time. The opposite sense-line pulse is induced in a similar manner when the back of the active-line pulse leaves the near end.

The response on the sense line shows that the presence of the groove lessens the crosstalk between the two lines at the near end. The amplitude of the near-end sense-line pulses in the ungrooved case is greater than the amplitude of the near-end sense-line pulses in the grooved case by a factor which is approximately equal to the ratio of the coupling coefficients when $h_1 = 0.0\mu\text{m}$ and $h_1 = 50.0\mu\text{m}$. At the far end of the sense line, the dispersion due to the difference in even- and odd-mode phase velocities [31] causes the amplitude of the far-end sense-line pulses to be larger in the grooved case. The line length at which the groove ceases to improve the crosstalk is determined from figure 4.14, which shows the time domain response at various points along the sense line, and from figure 4.15, which shows the maximum amplitude of the pulses as a function of position on the sense line. At line lengths less than 1.20cm, the maximum amplitude of the pulse in the grooved case is less than the maximum amplitude of the pulse in the ungrooved case; the converse is true for line lengths greater than 1.20cm.

4.6 Microstrip with Finite Substrate and Ground Plane

A microstrip with finite substrate and ground plane was considered in [67], and results were used as part of the verification of the IEMM code (section 3.2.2). New results for the microstrip with finite ground plane and substrate illustrate the effects of varying the distance t/w of the microstrip from the edge of the substrate/ground plane on steady-state and pulse propagation. The structure is shown in figure 4.16 (replicated from figure 3.3 for convenience).

As in the two-conductor structures of the previous sections, two modes propagate on the structure. When $t/w = 0.0$, the upper and lower conductors are the same width and

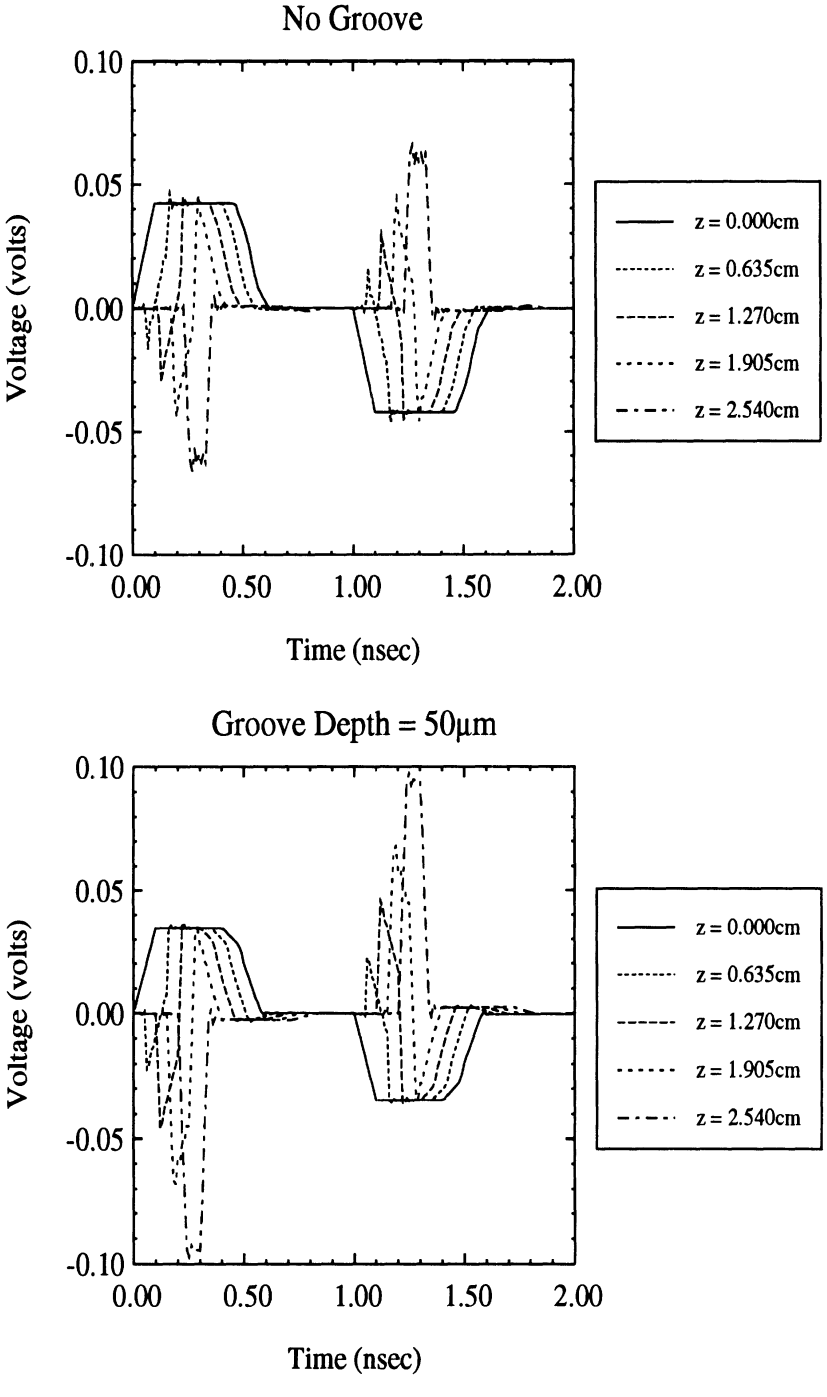

Figure 4.14: Propagation of a pulse on the sense line of coupled microstrip with no etched groove (top) and with an etched groove of depth $h_1 = 50\mu\text{m}$ (bottom). The geometry is given in figure 4.9.

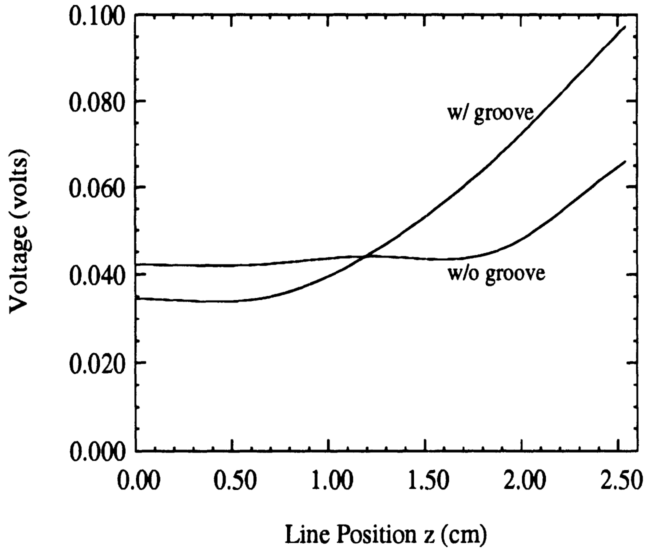

Figure 4.15: Maximum crosstalk on the sense line of coupled microstrip with and without an etched groove of depth $h_1 = 50$. The geometry is given in figure 4.9.

the modes are even and odd. When $t/w \neq 0.0$, the conductors have unequal widths and the modes are distorted versions of the pure even and odd modes. The odd and quasi-odd modes are designated as mode 1, and the even and quasi-even modes are designated as mode 2. Mode 1 is the dominant microstrip transmission line mode.

The frequency domain characterization is shown in figures 4.17–4.18. The even- and odd-mode phase constants β_1 and β_2 and the characteristic impedances Z_c change very little with increasing frequency for both $t/w = 0.0$ and $t/w = 2.0$ (figure 4.17). At 5.0 GHz, β_2 rises very slowly and β_1 increases then decreases as a function of increasing t/w (figure 4.18). The behavior of β_1 corresponds to a similar behavior of the confinement of the fringing fields in the dielectric substrate. The maximum and minimum β_1 differ by less than 10%. Unlike β_1 and β_2, the characteristic impedances depend strongly on t/w. The upper conductor impedances increase and the lower conductor impedances decrease with increasing t/w.

Pulse propagation on the structure is examined by applying a pulse with duration of 0.5ns, rise and fall times of 0.1ns, amplitude of 1.0V, and period of 10.0ns. The line lengths

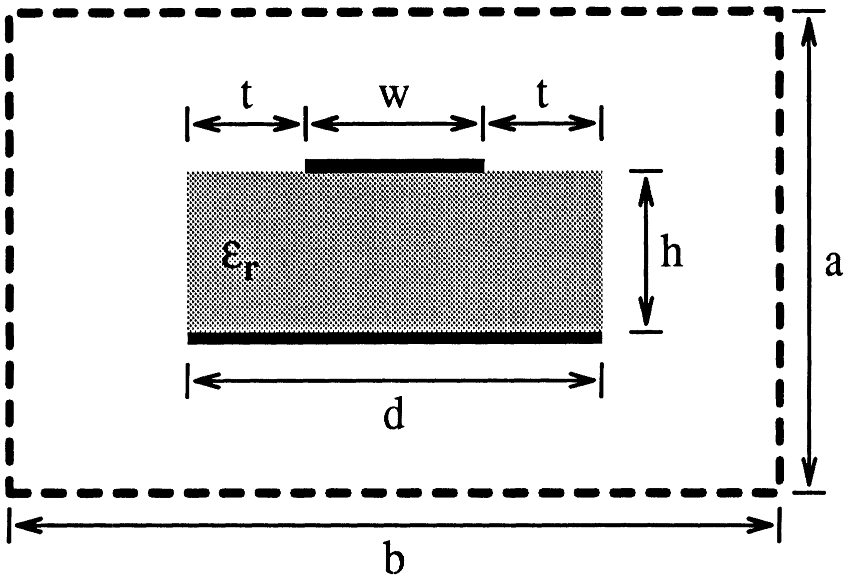

Figure 4.16: Microstrip with finite substrate and ground plane. The shielding waveguide is large enough so that its presence does not affect the results. (This figure is replicated from figure 3.3 for convenience.)

were 25.0cm, and the lines were excited at one end of the upper conductor, i.e., the "near end." Each end of the lines was terminated with the geometric mean of the even- and odd-mode characteristic impedances in order to minimize reflections.

Figure 4.19 shows the pulse at the near and far ends of the upper conductor for $t/w = 0.0, 2.0$. In each case, the pulse undergoes considerable dispersion over the length of the line. The shape of the pulse at the far end indicates that the dispersion is due to the large difference in phase velocities between the two propagating modes [31]. The small variations in β over frequency show that very little dispersion is caused by differing phase velocities of the significant frequency components of the pulse.

A comparison of the time domain results for $t/w = 0.0, 2.0$ shows differences in the amplitudes of the pulses and in the distortion of the far-end pulse. The amplitude differences are determined by the terminations; reflections at the ends were not completely eliminated with the chosen values. The differences in the distortion in the far-end pulse

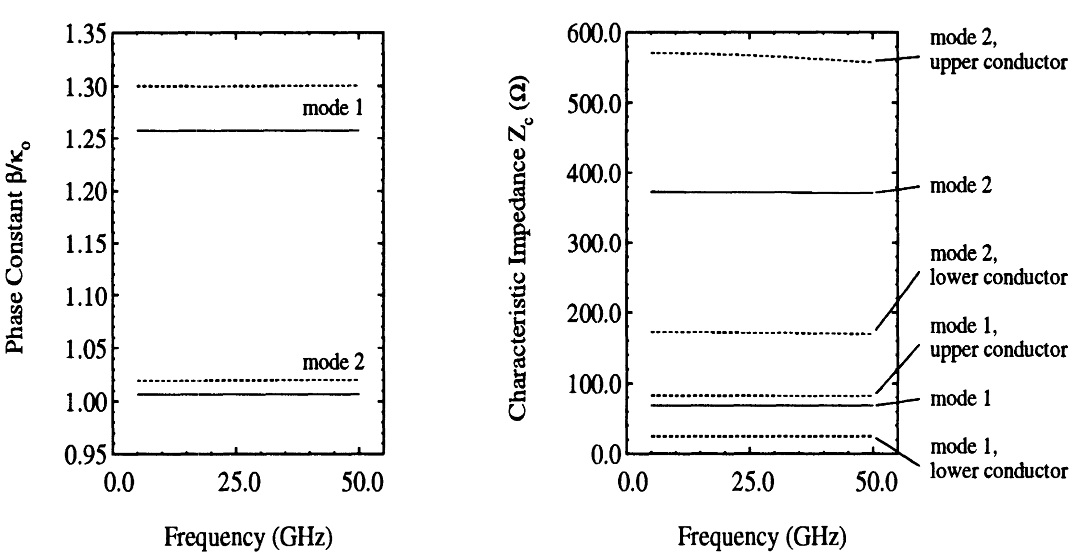

Figure 4.17: Phase constant and characteristic impedance vs. frequency for the structure of figure 4.16 with $t/w = 0.0$ (——) and $t/w = 2.0$ (- - -), $\epsilon_r = 2.2$, $w = h = 0.1$mm, $a = 3.5$mm, and $b = 2.0$mm.

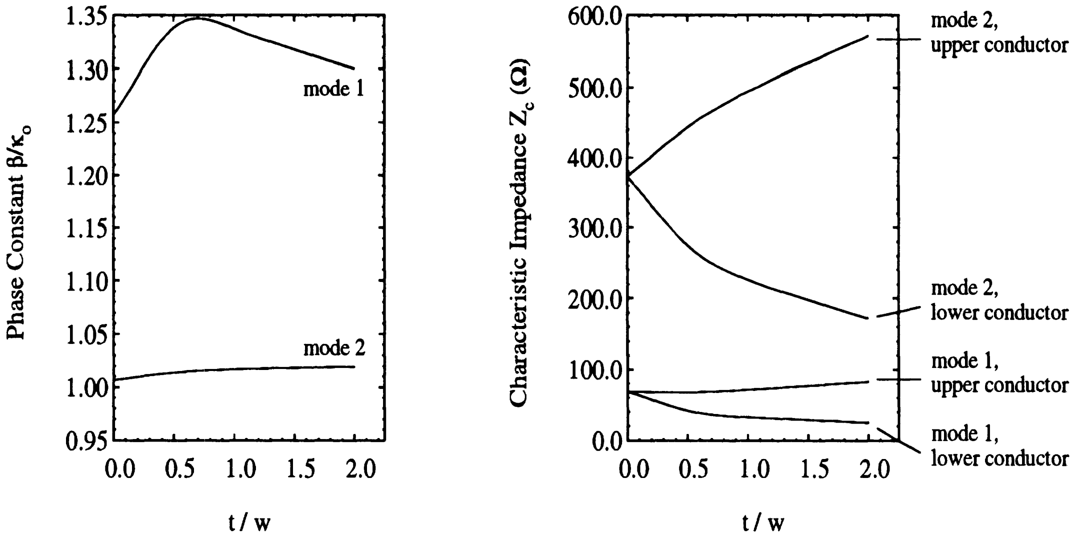

Figure 4.18: Phase constant and characteristic impedance vs. t/w for the structure described in figure 4.17 at frequency 5.0 GHz.

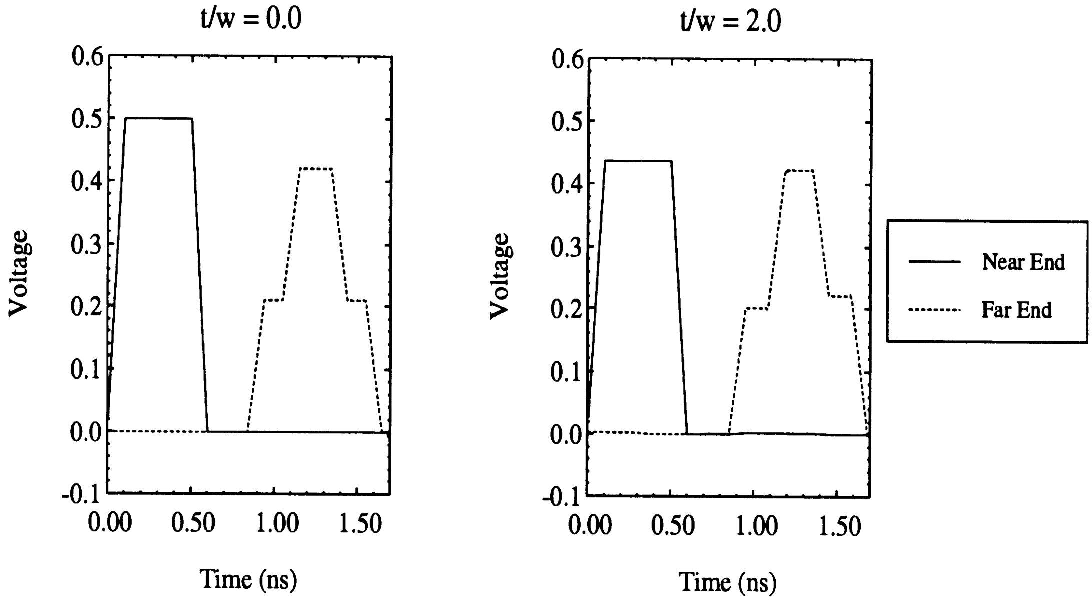

Figure 4.19: Pulse propagation on the upper conductor of the structure described in figure 4.17 with $t/w = 0.0, 2.0$.

are explained by considering the pulse as the sum of two pulses, each associated with one of the two propagating modes on the conductor. When $t/w = 2.0$, the asymmetry of the modes causes the distortion of the far-end pulse to be asymmetric as well.

4.7 Coupled Multilevel Microstrip with a Finite Intermediate Dielectric Layer

Coupled microstrip on different layers with a finite intermediate layer (FIL) and with a homogeneous intermediate layer (HIL) are shown in figure 4.20. The shielding is once again far enough from the strips so as to not affect the results. The effect of the finite layer is shown in the frequency and time domains in figures 4.21–4.24.

Like the structure of the previous section, two modes propagate on this structure. The phase constants and characteristic impedances versus frequency are plotted in figures 4.21–4.22. In both the FIL and HIL cases, the phase constants increase gradually with frequency. The HIL phase constants are greater than the corresponding FIL phase constants since the HIL causes more of the fields to be confined within the dielectric. Notable in figure 4.22

are the negative values of the mode 1, upper conductor and the mode 2, lower conductor characteristic impedances in the HIL case. These values are a consequence of enforcing the reciprocity condition in the characteristic impedance calculation [12].

Pulse propagation on the FIL and HIL structures is shown in figures 4.23–4.24. The pulse is the same as the microstrip on finite substrate and ground plane: the duration is 0.5ns, the rise and fall times are 0.1ns, the amplitude is 1.0V and the period is 10.0ns. The excitation is at the near-end of the upper conductor. The line length is again 25.0cm and the termination at the end of each line is 50Ω.

The dispersion of the pulse at the far end of the upper conductor in the FIL case is much greater than in the HIL case (figure 4.23). As in the previous section, the dispersion in the FIL case is due to the difference in the modal phase velocities, and the asymmetry in the distortion of the pulse is due to the asymmetric nature of the propagating modes. The dispersion in the HIL case is minimal because the presence of the additional dielectric material reduces mode 1's contribution to the pulse to a negligible level, i.e., the additional dielectric greatly increases the isolation between the two strips.

The crosstalk on the lower conductor is comparable at the near-end of each case and much lower in the HIL case at the far-end (figure 4.24). The relative magnitudes of the far-end crosstalk provide further evidence of the greater isolation between the lines in the HIL case.

The signal at the near-end of the sense line is a small single pulse, while in the case of the coupled microstrip with an etched groove the signal consisted of two pulses of opposite amplitude (section 4.5 and figure 4.13). The difference occurs because the line length was much shorter in the grooved geometry. With the longer line length, the rise and fall of the pulse on the sense line are simply induced by the rise and fall of the pulse on the active line.

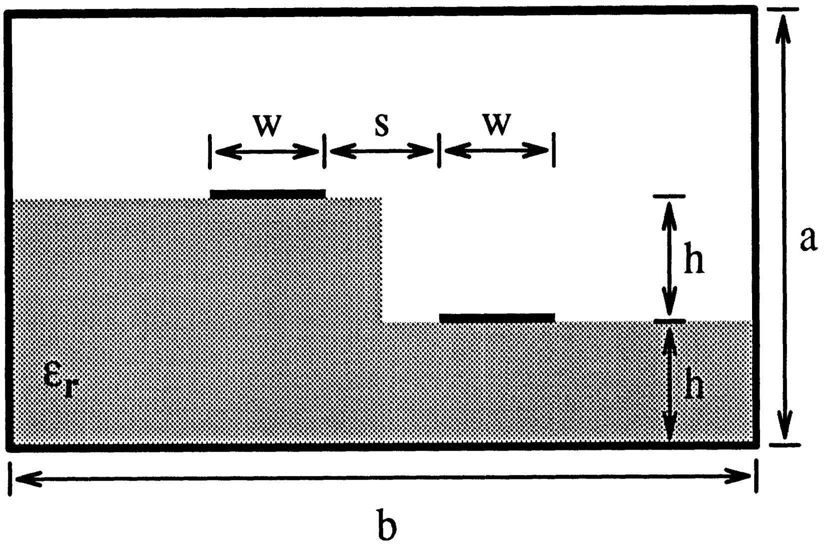

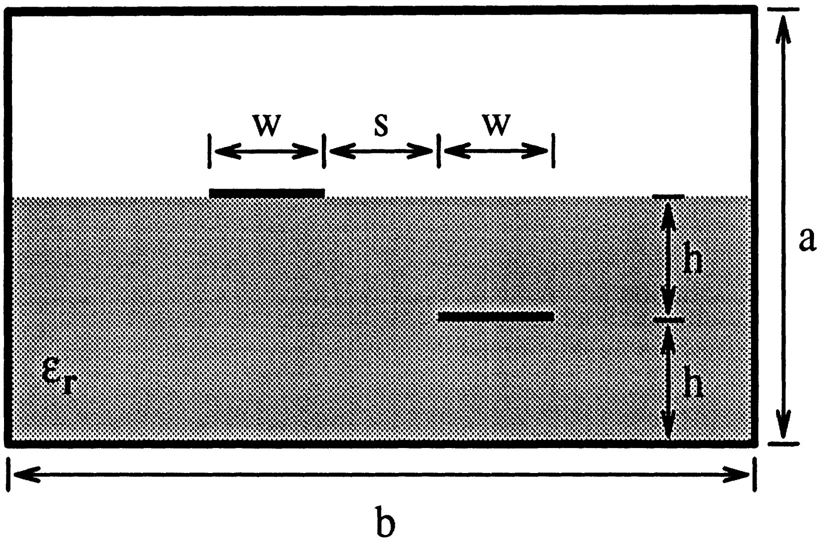

Figure 4.20: Coupled multilevel microstrip with a finite intermediate layer (FIL) and with a homogeneous intermediate layer (HIL). $\epsilon_r = 12.0$, $w = h = s = 0.1$mm, and $a = b = 1.2$mm.

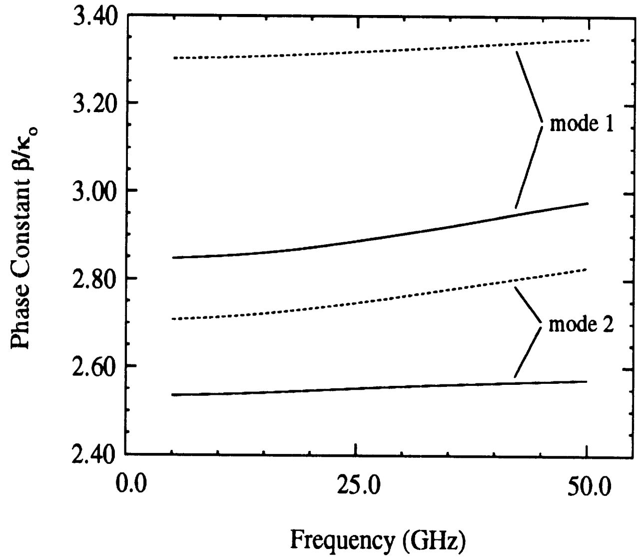

Figure 4.21: Phase constant vs. frequency for the coupled multilevel microstrip structures of figure 4.20. Finite intermediate layer: ——; homogeneous intermediate layer: - - -.

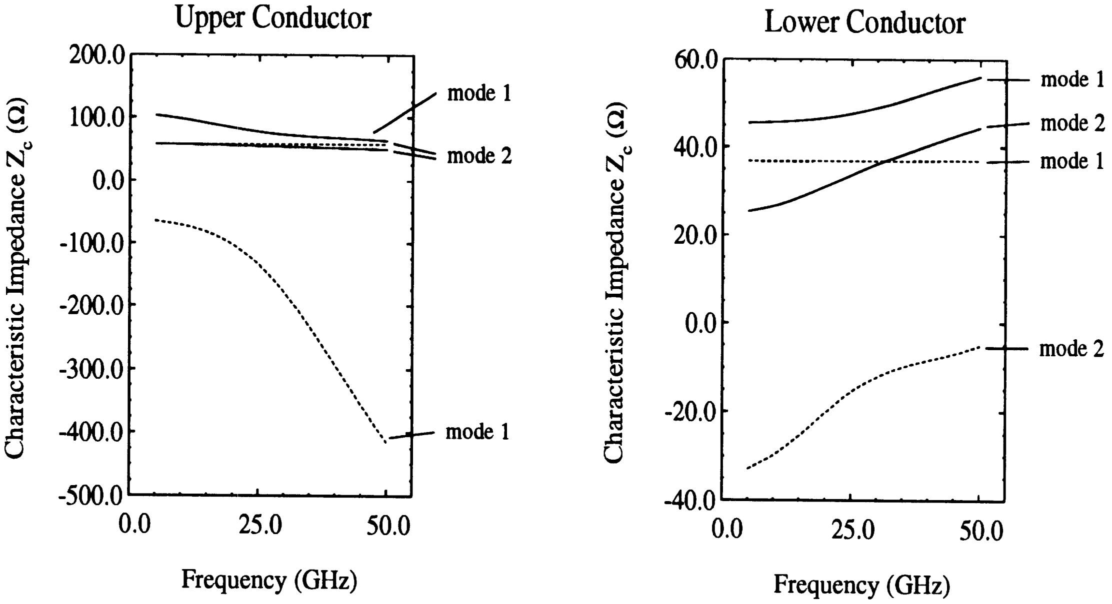

Figure 4.22: Characteristic impedance vs. frequency for the coupled multilevel microstrip structures of figure 4.20. Finite intermediate layer: ——; homogeneous intermediate layer: - - -.

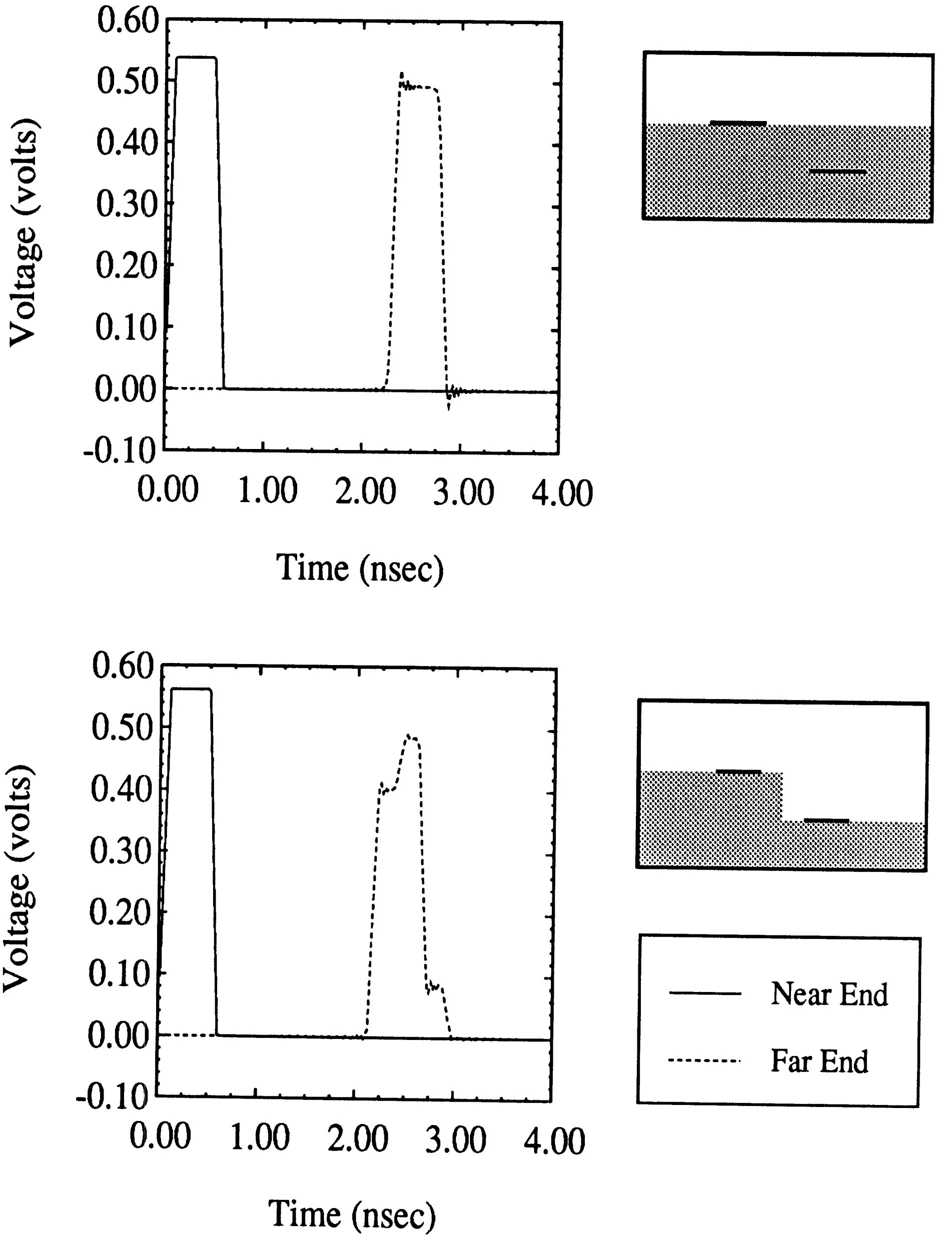

Figure 4.23: Pulse propagation on the active (upper) conductors. The dimensions of the structures are given in figure 4.20.

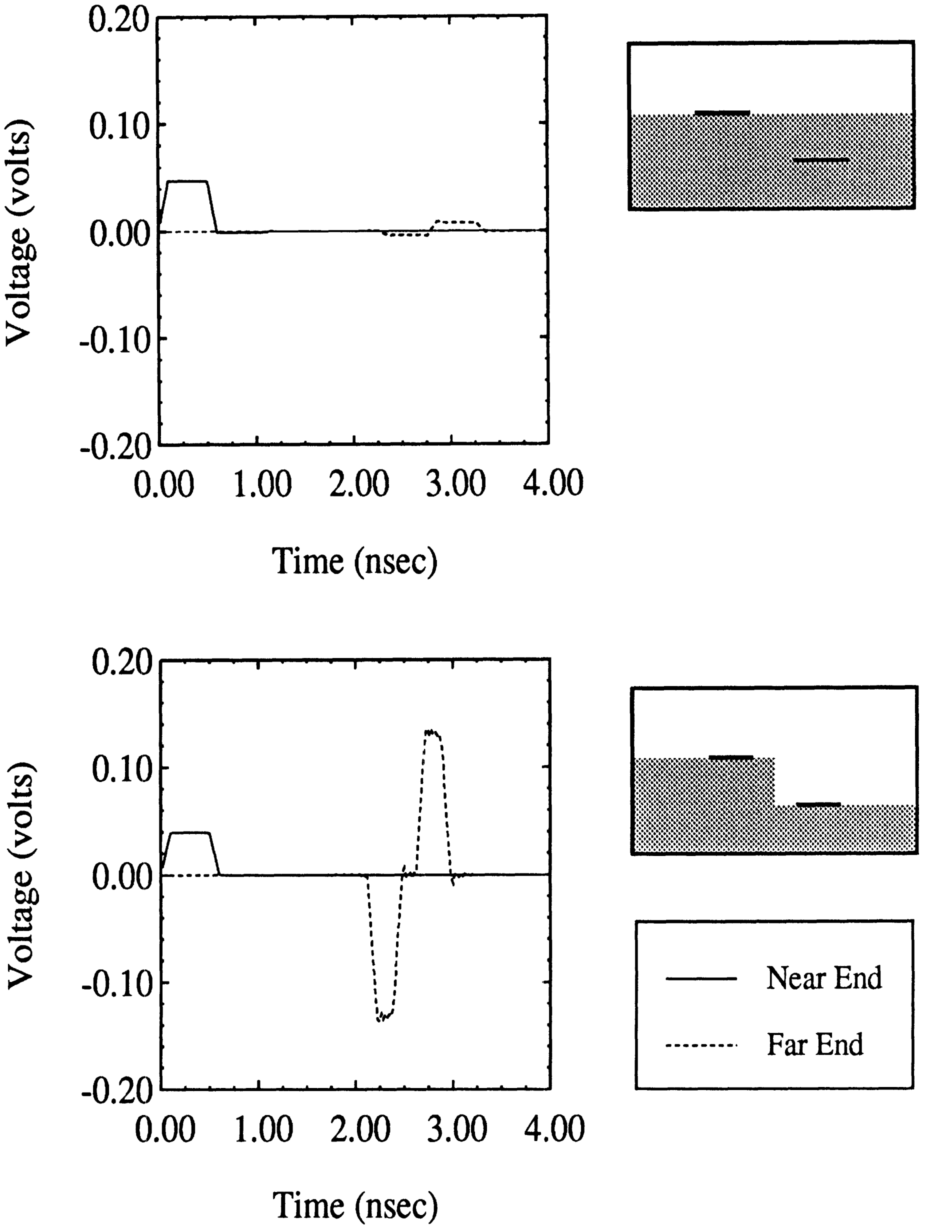

Figure 4.24: Pulse propagation on the sense (lower) conductors. The dimensions of the structures are given in figure 4.20.

4.8 Electro-optic Modulator Structures

The IEMM analysis technique may also be applied to electro-optic modulator structures. A possible integrated traveling-wave modulator structure (figure 4.25) consists of an intrinsic GaAs guiding layer for the optical signal and p- and n-$\mathrm{Al_{0.025}Ga_{0.975}As}$ layers for top and bottom cladding. Typically, an integrated modulator is constructed on a 250μm n^+-GaAs substrate; for simplicity, the substrate has been assumed to be a perfect conductor in this case. The optical signal is modulated by a microwave signal, which is guided by the two conducting strips. The bandwidth depends inversely on the difference between the optical and microwave indices of refraction [3]. The microwave index of refraction (i.e., β/k_o) is considerably larger than the optical index of refraction (= 3.41 for intrinsic GaAs at $\lambda = 1.3\mu$m [82]). A groove is etched between the two electrodes in order to improve the bandwidth by decreasing the microwave index of refraction and to minimize the attenuation in the microwave signal [87].

The microwave phase and attenuation constants are plotted over the frequency range 1–40 GHz for two different groove depths in figure 4.26. As the frequency increases to 13 GHz, the phase constants β/k_o decrease; at frequencies above 13 GHz, the phase constants are approximately constant at values between 4.0 and 6.0. The attenuation constants increase with frequency. The microwave frequency at which the difference between microwave and optical indices of refraction is minimized, and at which microwave attenuation is minimized, is therefore approximately 13 GHz.

The behavior of the propagation constants as the groove width and height varies at 18 GHz is presented in figures 4.27–4.28. As the groove width s increases, the even and odd modes decouple as the phase constants converge; the attenuation is only slightly affected. As the groove depth h increases, the odd-mode attenuation decreases until the groove begins to penetrate the lossless layer, at which point the attenuation becomes ap-

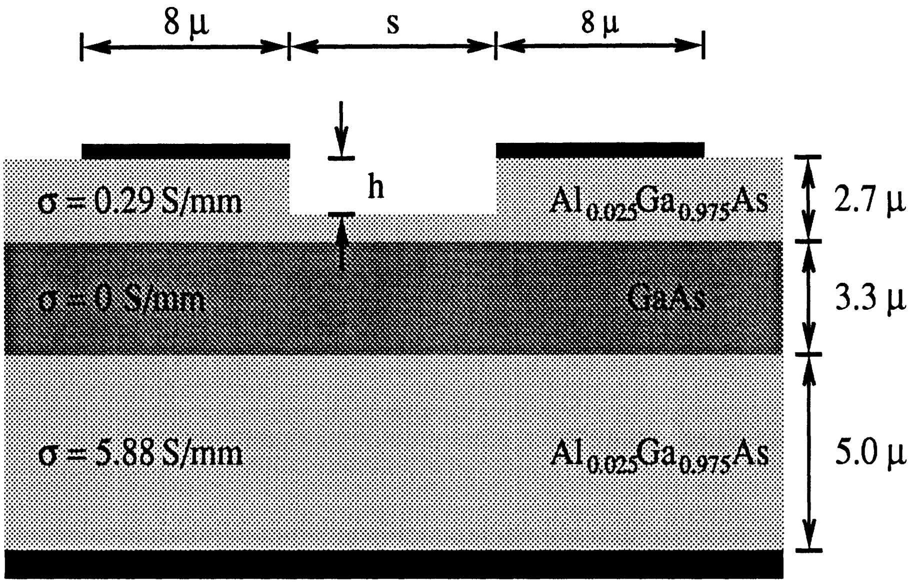

Figure 4.25: Geometry of modulator structure. The structure is shielded, but the shielding is large enough so that it does not affect the results. The shielding has width = height = 1mm.

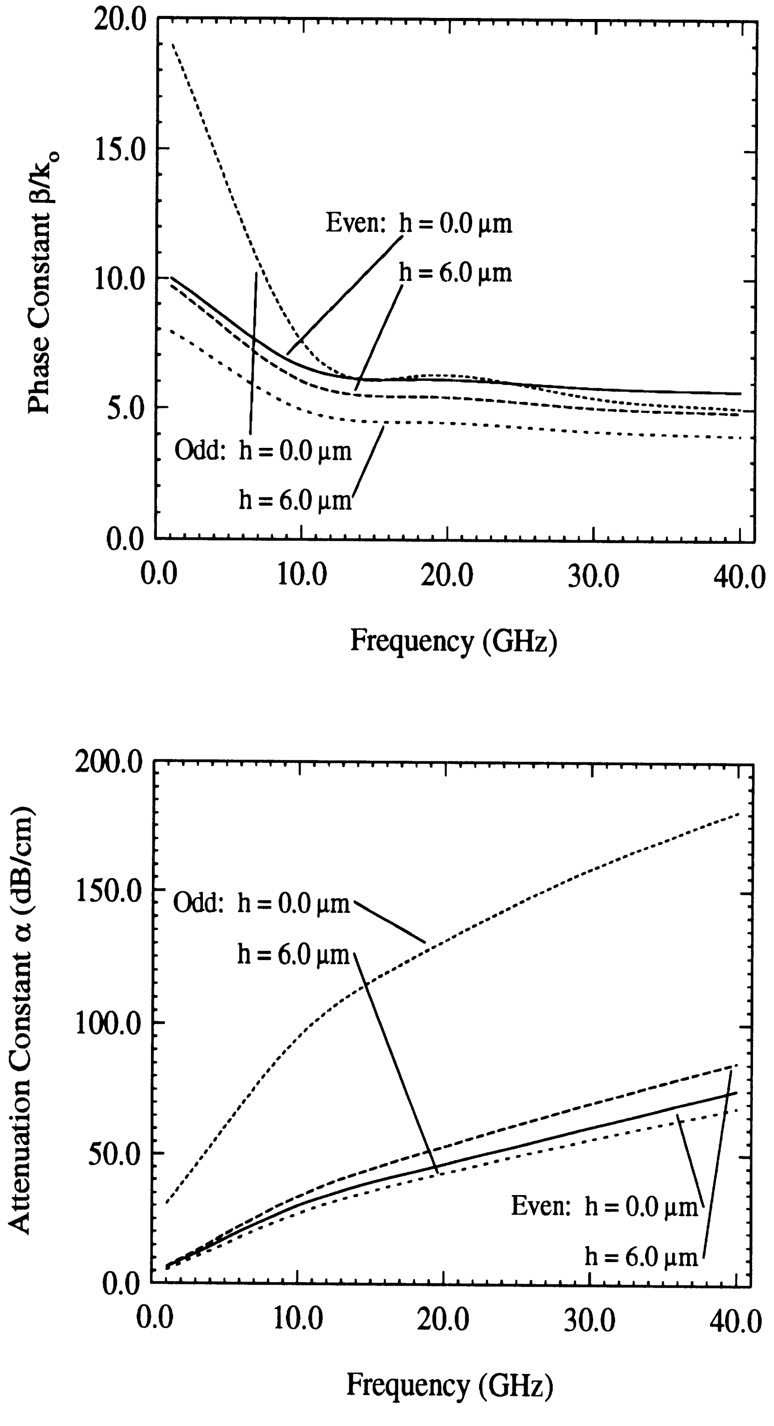

Figure 4.26: Propagation constant $\gamma = \alpha + j\beta$ vs. frequency for the modulator structure of figure 4.25 at groove width $s = 8.0\mu$m and groove depths $h = 0.0\mu$m and $h = 6.0\mu$m.

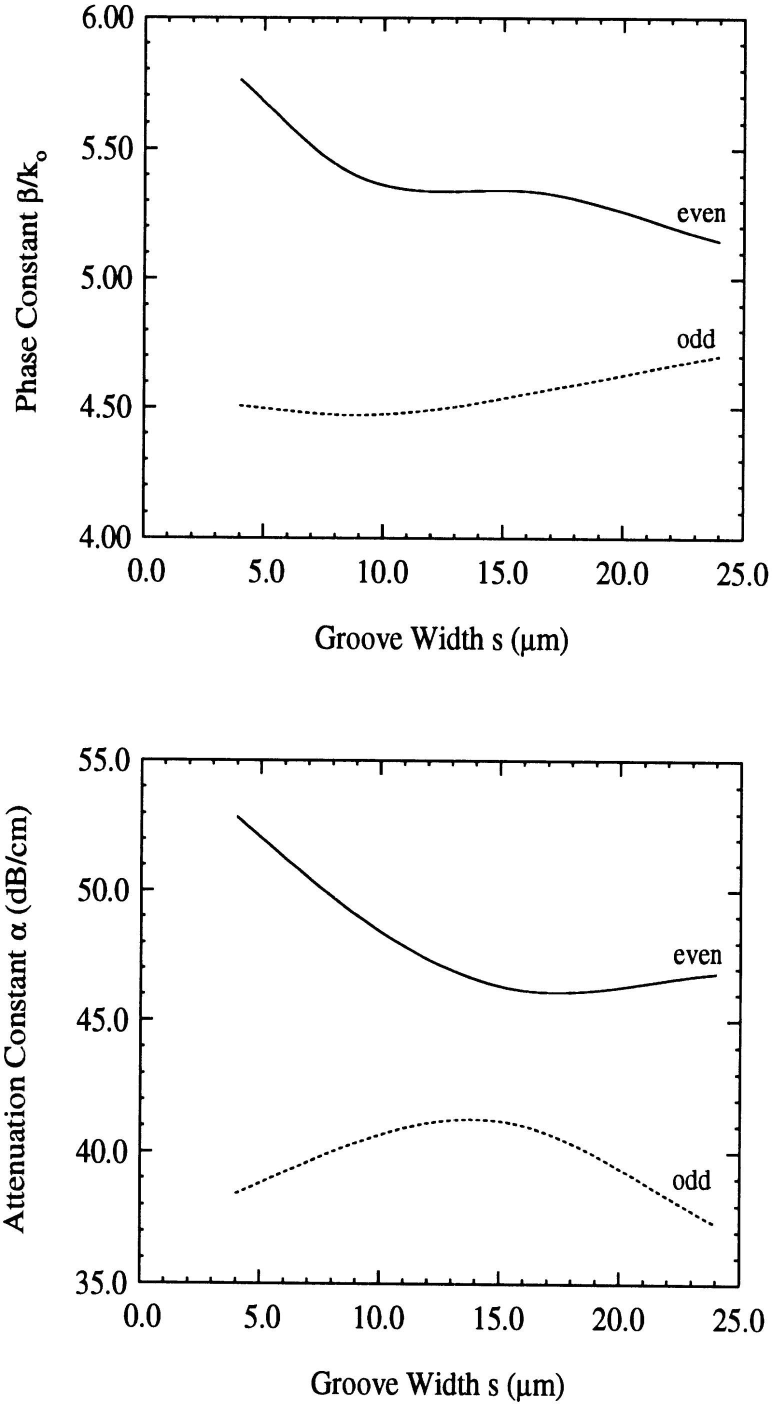

Figure 4.27: Propagation constant $\gamma = \alpha + j\beta$ vs. groove width s for the modulator structure of figure 4.25 at frequency = 18 GHz and groove depth $h = 6.0\mu$m.

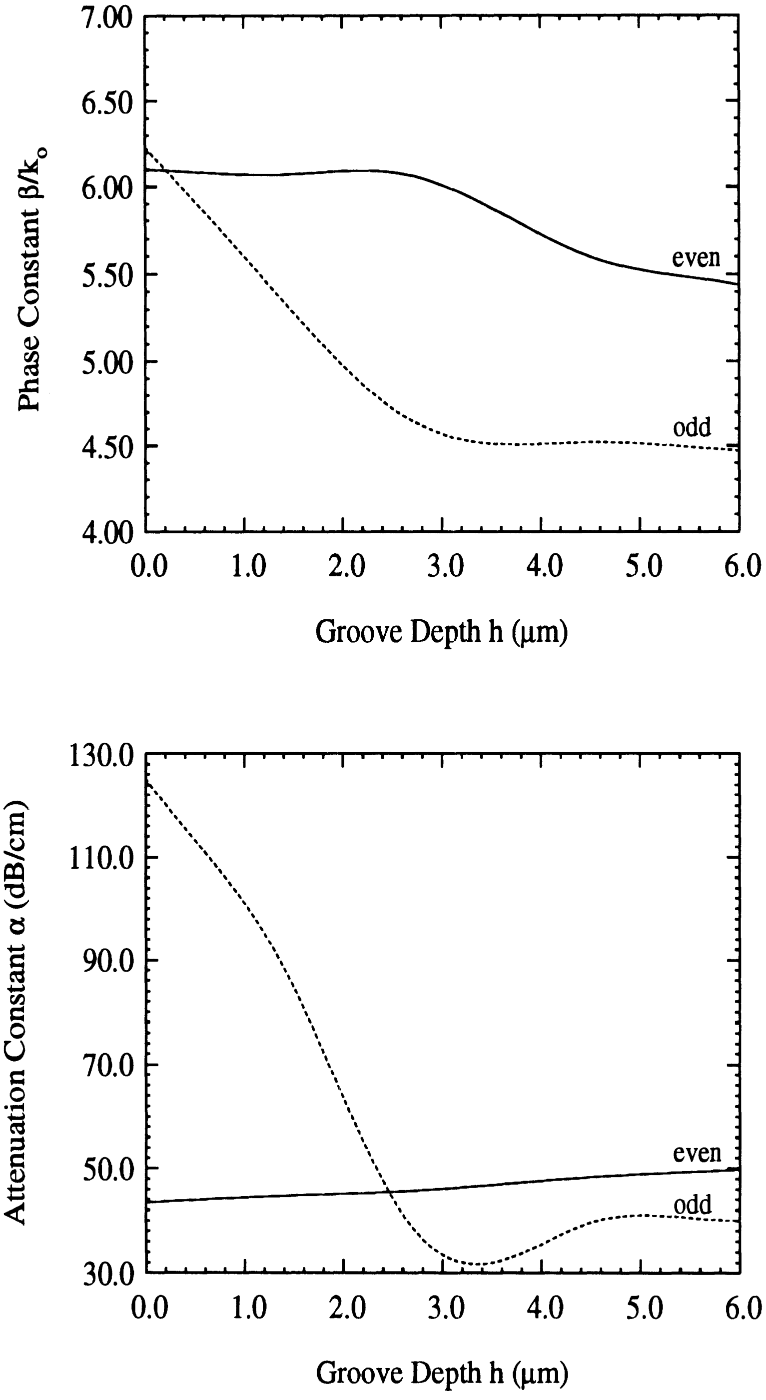

Figure 4.28: Propagation constant $\gamma = \alpha + j\beta$ vs. groove depth h for the modulator structure of figure 4.25 at frequency = 18 GHz and groove width $s = 8.0\mu$m.

proximately constant. This characteristic is consistent with the attenuation constant data over frequency, which shows that the odd-mode attenuation constant is highest when no groove is present ($h = 0.0\mu$m). The odd mode evidently has a large fraction of its power contained in the area between the conductors in the upper lossy cladding layer.

Of interest in the characteristic impedance plots (figures 4.29–4.31) is the relatively small ($< 10\Omega$) change in resistance over the entire range of groove and widths and heights. Design of the electro-optic structure is thereby simplified, since, at a given frequency, the optimal propagation constant may be chosen from the range of groove dimensions without fear of an undesired large change in characteristic impedance.

4.9 Summary

The IEMM method was applied to the frequency and time domain characterization of a variety of nonplanar two-dimensional structures. Generally, the presence of grooves, ridges and layers was found to either increase or decrease coupling between two conducting strips, depending greatly on the geometry of the structure. The results introduce new methods for increasing packing density, decreasing crosstalk and enhancing coupling in VLSI, monolithic and hybrid applications.

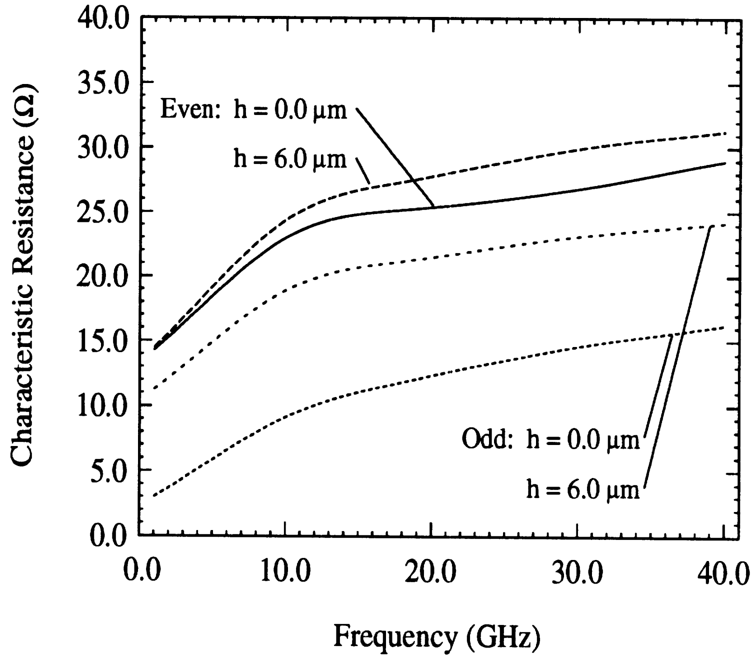

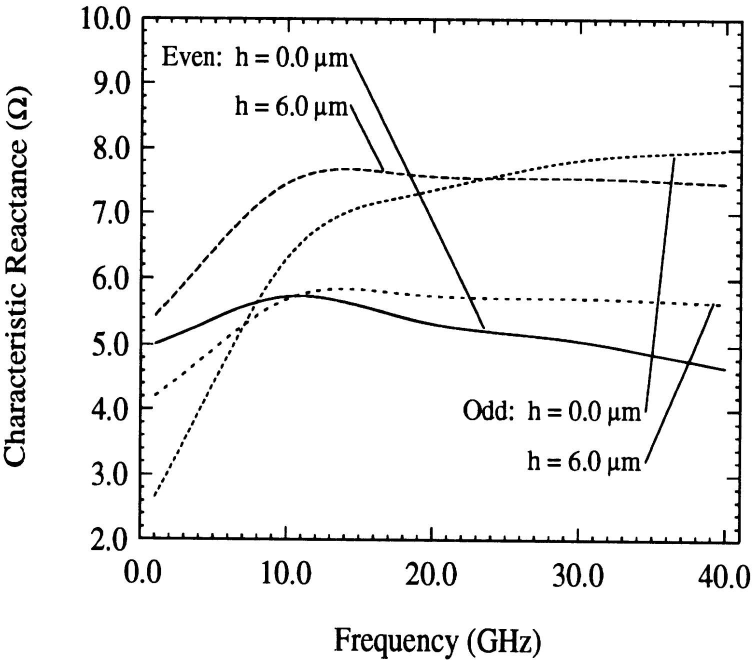

Figure 4.29: Characteristic impedance vs. frequency for the modulator structure of figure 4.25 at groove width $s = 8.0\mu$m and groove depths $h = 0.0\mu$m and $h = 6.0\mu$m.

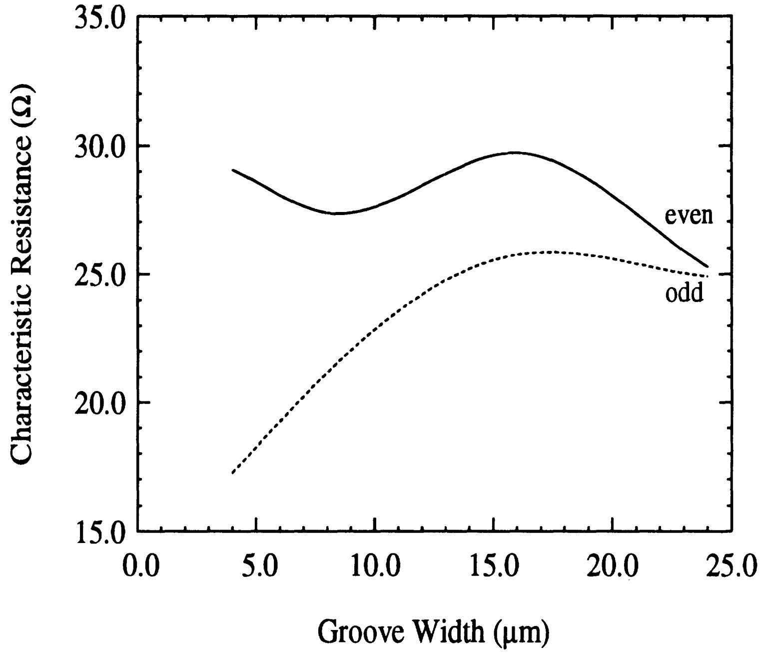

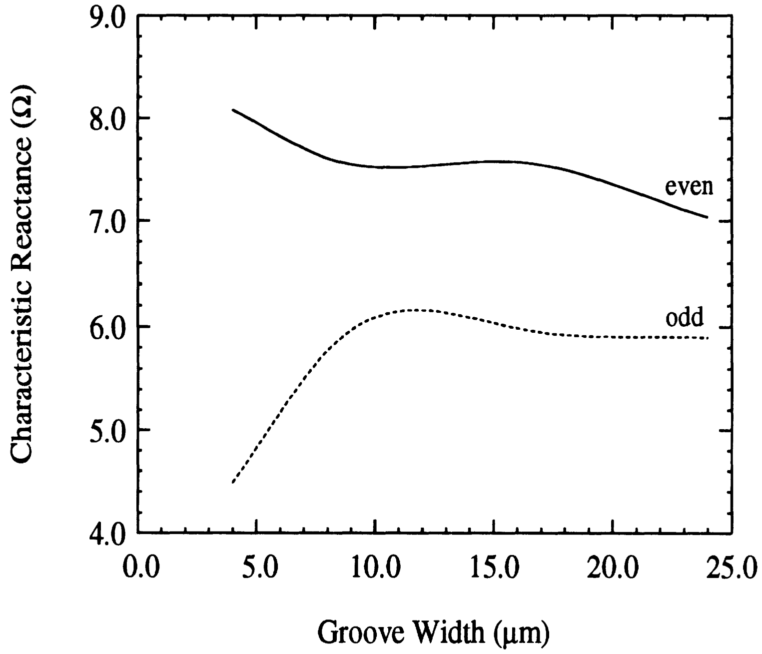

Figure 4.30: Characteristic impedance vs. groove width s for the modulator structure of figure 4.25 at frequency = 18 GHz and groove depth $h = 6.0\mu$m.

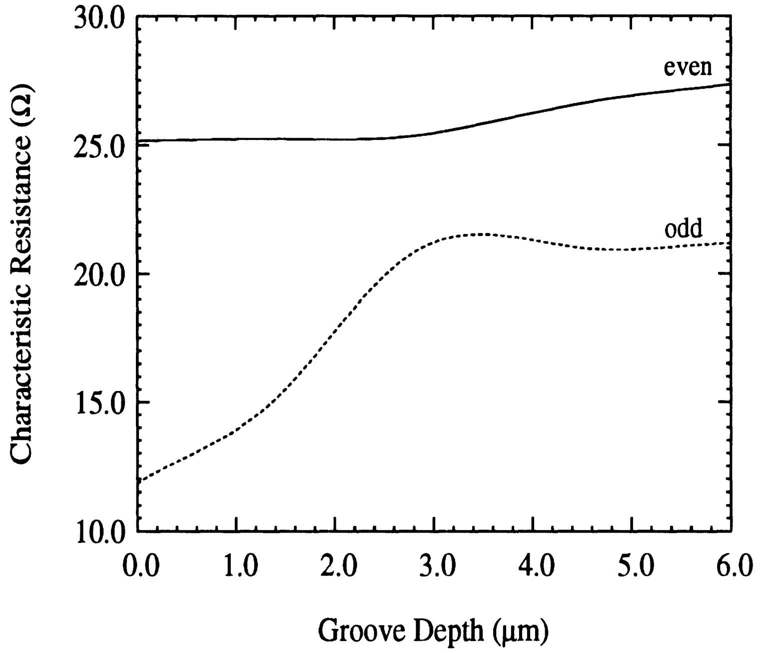

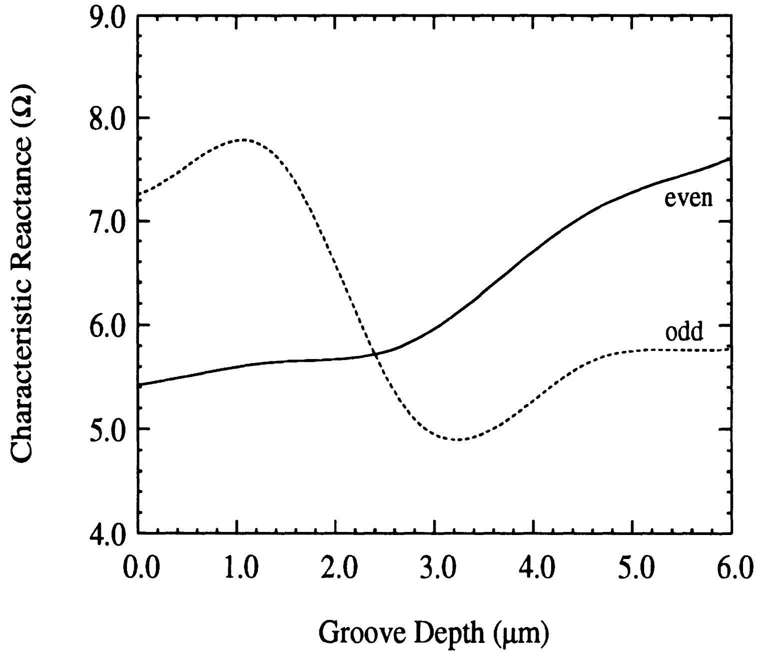

Figure 4.31: Characteristic impedance vs. groove depth h for the modulator structure of figure 4.25 at frequency = 18 GHz and groove width $s = 8.0\mu$m.

CHAPTER V

LOW-LOSS LAYERED RIDGED DIELECTRIC WAVEGUIDES FOR SUB-MILLIMETER-WAVE AND TERAHERTZ FREQUENCY APPLICATIONS

Because the extensions of planar monolithic millimeter-wave and optical technologies to sub-millimeter-wave and terahertz frequencies have inherent limitations (section 1.1), different approaches are necessary for the design of monolithic transmission lines at these frequencies. One such approach is established by examining the millimeter wave dielectric waveguides which were extensively investigated in the 1970's and early 1980's. Examples of these waveguides include dielectric image guides [68], strip dielectric guides, insulated image guides, strip-slab guides [50], inverted strip dielectric guides [40], cladded image guides [53], and trapped image guides [41]. The waveguides are constructed from combinations of layers and ridges of various permittivities in order to provide a region wherein the propagating power is well-confined. The widths of the lines approach one guided wavelength in order to maximize field confinement. Although there are several examples of the monolithic use of dielectric waveguides in the literature (e.g., [83]), these waveguides have been generally considered hybrid in nature.

Monolithic sub-mm and THz guiding structures are realized by considering variations of the early dielectric waveguides. The new waveguides are constructed from dielectric materials and structures which are available in monolithic technology so that the use of the waveguides in integrated circuits is possible. The dimensions of the waveguides are on the order of a fraction of a guided wavelength, so that the new structures can be used not only as transmission lines, but also as passive circuit elements such as inductors and couplers. Since the proposed structures will have properties similar to conventional microstrip elements, the structures will be able to provide both low-loss feeding networks and highly efficient radiating elements for arrays.

In the succeeding sections, two types of monolithic guiding structures are described. Examples are designed for specific frequencies in the 0.3–2.0 THz and 0.1–0.3 THz ranges and propagation in each of the waveguides is characterized over relevant frequency ranges by applying the mode-matching technique of section 2.7.

5.1 Proposed Construction

The proposed structures, shown in figures 5.1–5.3, consist of alternating layers of high and low permittivities. The abrupt changes in the permittivities in the x-direction are designed to optimize power confinement in the layer with the lowest permittivity. This layer, designated the *propagation layer*, is away from the ground plane, resulting in minimal ground plane conductor loss. A ridge or a semi-embedded strip provides power confinement in the y-direction.

The structures in figures 5.1 and 5.2 are suitable for the 0.3–2.0 THz region. The structures may be either ridged or semi-embedded and are made of semiconducting materials grown on GaAs or InP substrates. The ridged structure is created by etching a layered wafer. The semi-embedded waveguide is fabricated by etching a well of appropriate dimensions into a semiconducting substrate, filling the well with layers of intrinsic semiconducting materials using regrowth techniques, and etching again. In both the ridged and the semi-embedded structures, layers of 5–10 microns are required, and these layers can be provided by MOCVD.

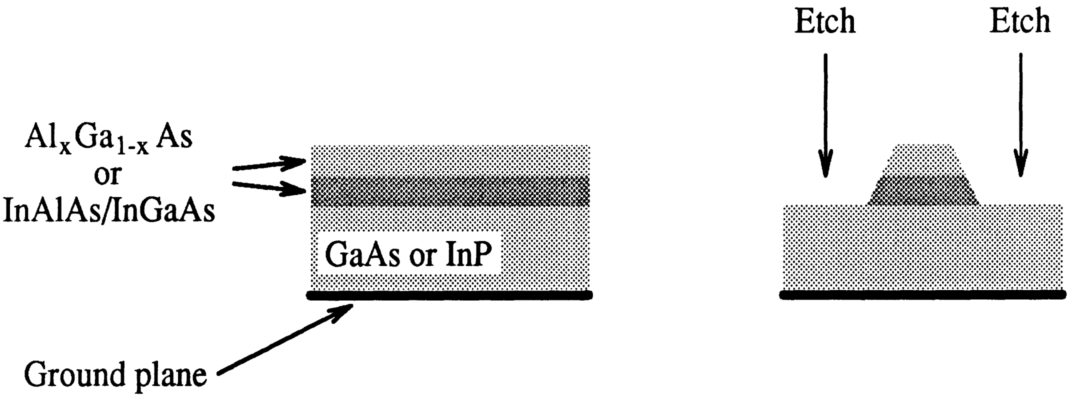

Figure 5.1: Ridged example of 0.3–2.0 THz waveguide.

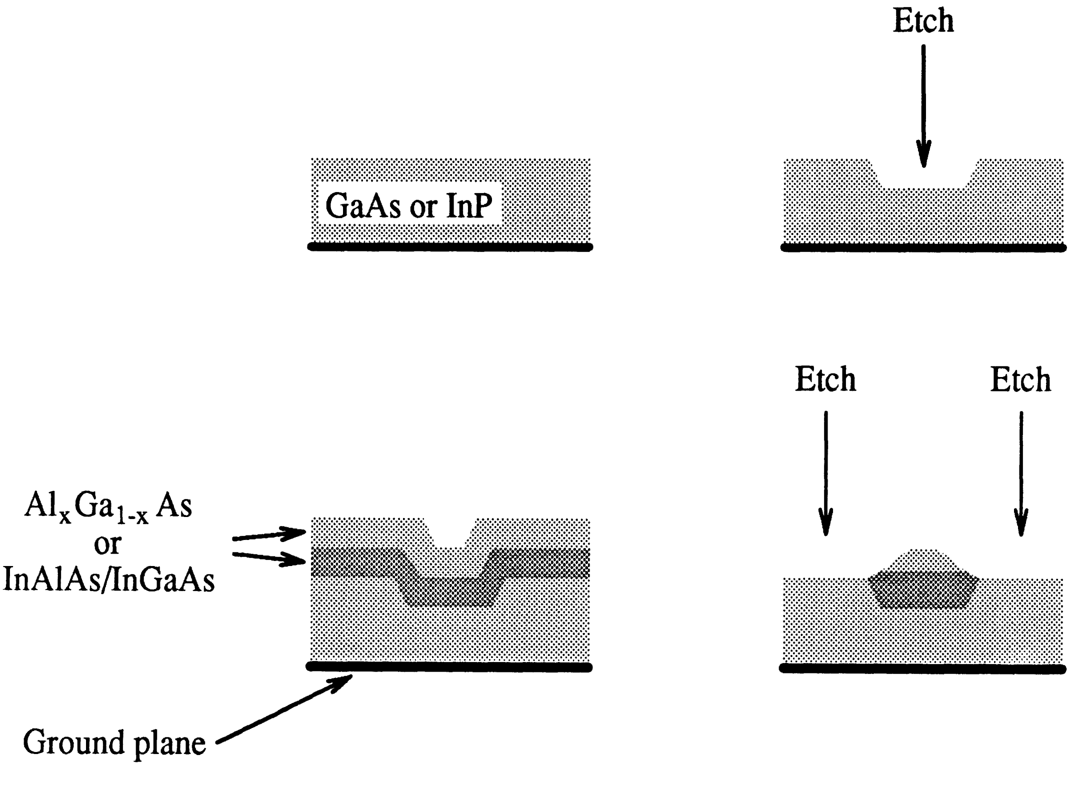

Figure 5.2: Semi-embedded example of 0.3–2.0 THz waveguide.

As the frequency of operation decreases, thicker layers are required and the times required to grow the layers on the wafers become impractically large. Hence, a second type of waveguide is proposed for the sub-mm wave region (0.1–0.3 THz). This structure is constructed from a combination of semiconducting substrates and dielectric films. In the example shown in figure 5.3, a wafer of GaAs is covered with a polyamide film, attached to another GaAs wafer with a thin epoxy glue, and etched to produce a ridged waveguide. The epoxy is expected to create a gap of approximately 1 micron, which would not affect the propagation characteristics. A similar structure could be created with silicon wafers and a quartz film; in this case, the wafers are attached with electrobonding.

The fabrication of integrated circuits which use the dielectric waveguides as interconnects is conceivable. For example, an active device can be integrated with the 0.1–0.3 THz waveguide by manufacturing the device in the position shown in figure 5.3. This step is performed prior to the addition of the polyamide layer; the subsequent construction of the layers and the etching to create the ridged structure may be done without damaging the active device. An active device may be integrated with a 0.3–2.0 THz waveguide in a similar fashion, but the addition of high quality, low-loss layers after the device has been manufactured may be troublesome if the process used to add the layers requires temperatures which are high enough to damage the active device. Several alternatives exist for the design of a transition between an active device and a waveguide. The similarity between the dominant mode of the dielectric waveguide and the dominant mode in microstrip and the ease with which a transition between microstrip and an active device may be accomplished suggests that a transition could consist of a short length of microstrip near a device (figure 5.3). Another design could employ a vertical probe extending upward from the device into the propagation layer. A combination of the above alternatives could also be used as a transition. The device could be biased using side feeds which are perpendicular

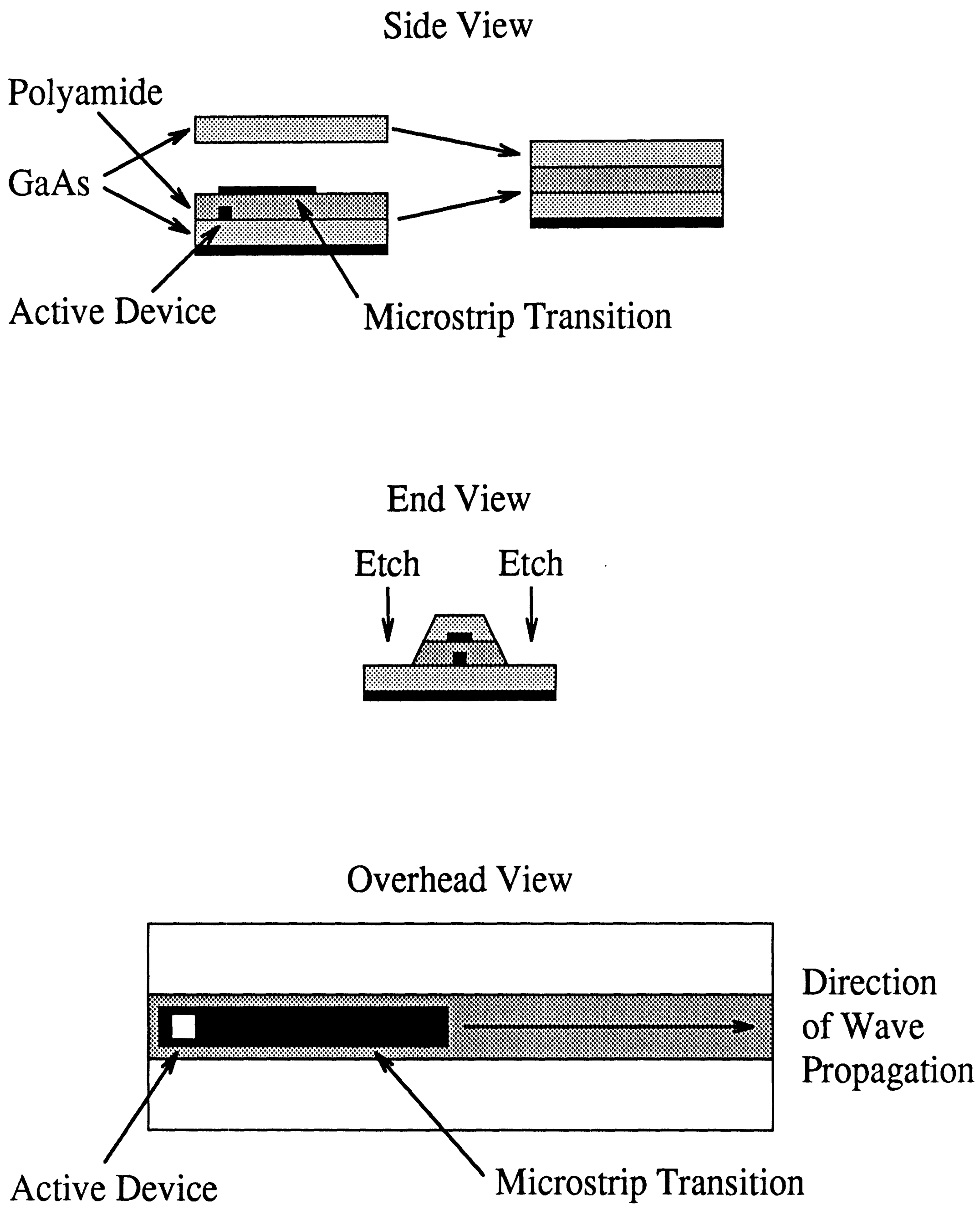

Figure 5.3: Example of 0.1–0.3 THz waveguide, including the integration of an active device and its transition.

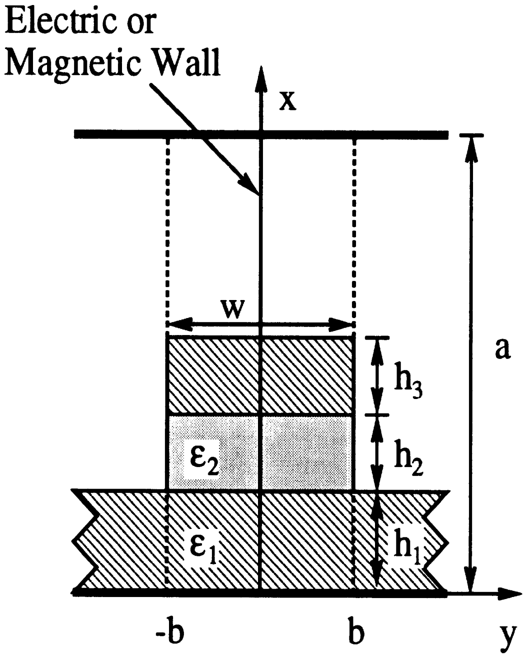

Figure 5.4: General structure for layered ridged dielectric waveguide design examples.

to the direction of propagation. Passive structures such as couplers, stubs, T-junctions, and inductors can be created by fabricating the transmission lines in the desired pattern on the substrate and selectively adding metallization to add inductance or improve power confinement.

5.2 Design Examples

The design parameters and characterization of an example of each type of guiding structure are given in figures 5.5–5.15. The structures are designed specifically for 94 and 490 GHz and are constructed as shown in figure 5.4. Each structure has a GaAs substrate with a ground plane; the 94 GHz waveguide consists of layers of polyamide and GaAs, and the 490 GHz waveguide consists of layers of AlAs and GaAs. The permittivity of AlAs is given in [1]. Although the substrate of the 490 GHz waveguide is extremely thin (17.1μm), the substrate/ground plane configuration can be realized by growing a layer of intrinsic GaAs on another highly conductive wafer. The dimensions of the propagation layers at the design frequencies are on the order of 1/10th of a guided wavelength $\lambda_g(= 2\pi/\beta)$. The structures are open in the lateral direction. Since the structures are symmetric, the analysis is simplified by adding an electric or magnetic wall at $x = 0$ and only considering half of the structure.

5.2.1 Propagation Constants

In general, the propagation constant γ is complex and is expressed in terms of the phase constant β and the attenuation constant α as

$$\gamma = \alpha + j\beta \tag{5.1}$$

If all of the dielectrics are lossless, the propagation constants may be either real, imaginary or complex. When γ is real ($\alpha \neq 0$, $\beta = 0$), the mode is evanescent. When γ is imaginary ($\alpha = 0$, $\beta \neq 0$), the mode is propagating; thus, all the power is bound to the waveguide and propagates in the z-direction. When γ is complex ($\alpha \neq 0$, $\beta \neq 0$), the mode is also propagating, but power propagates at an angle away from the z-axis into the surrounding substrate, In the latter case, the mode is "leaky", and deleterious crosstalk effects could be significant. If any of the dielectrics are lossy, γ is always complex.

Determining the propagation constants of non-leaky modes of the laterally open lossless structure is straightforward, but some additional calculations are required to determine the leaky modes. Recall that each mode's propagation constant is a mode of the structure if it is a zero of the mode-matching/transverse resonance matrix's determinant (section 2.7). The non-leaky modes of the structure are found by searching for zeros of the determinant with imaginary values of γ. Leaky modes are determined by first considering a structure which has sidewalls which are very far away from the ridge. In order to simulate the open case, only propagating modes with $\beta/k_o > 1$ are considered. Each propagating mode of the laterally shielded structure corresponds to a non-leaky or a leaky propagating mode in the

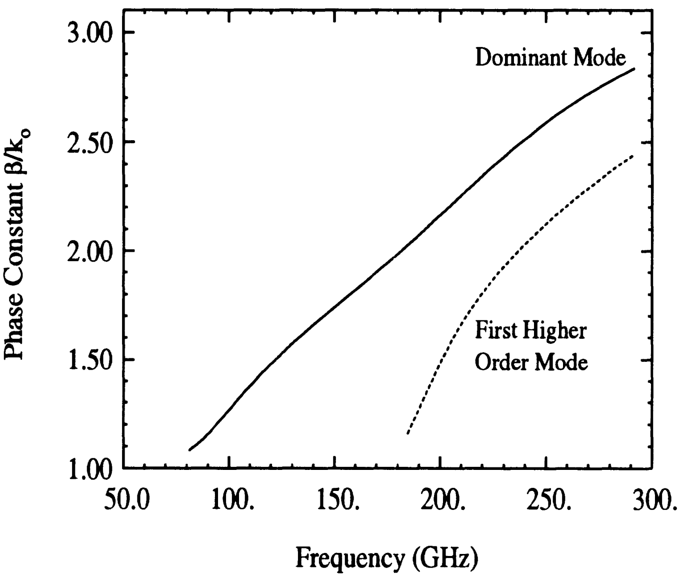

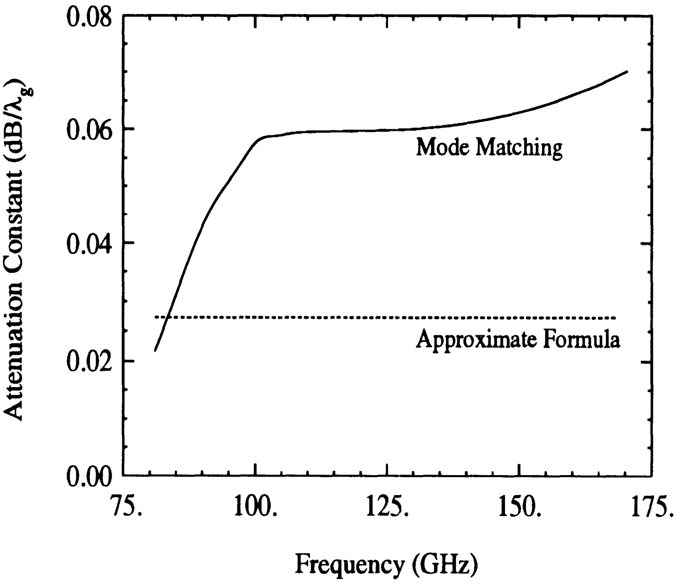

Figure 5.5: Propagation constant of the structure designed for 94 GHz. Referring to figure 5.4, $h_1 = 0.032\lambda_g$ (86.4μm), $h_2 = 0.049\lambda_g$ (130μm), $h_3 = 0.116\lambda_g$ (309μm), $w = 0.091\lambda_g$ (241μm) and $a = 0.863\lambda_g$ (2.31mm). Top: phase constant as a function of frequency with lossless dielectrics. $\epsilon_1 = 12.85\epsilon_o$ (GaAs), $\epsilon_2 = 3.0\epsilon_o$ (polyamide). Bottom: upper bound of attenuation constant as a function of frequency with worst-case dielectric losses. $\epsilon_1 = 12.85\epsilon_o(1.0 - j0.002)$ (GaAs) and $\epsilon_2 = 3.0\epsilon_o(1.0 - j0.001)$ (polyamide).

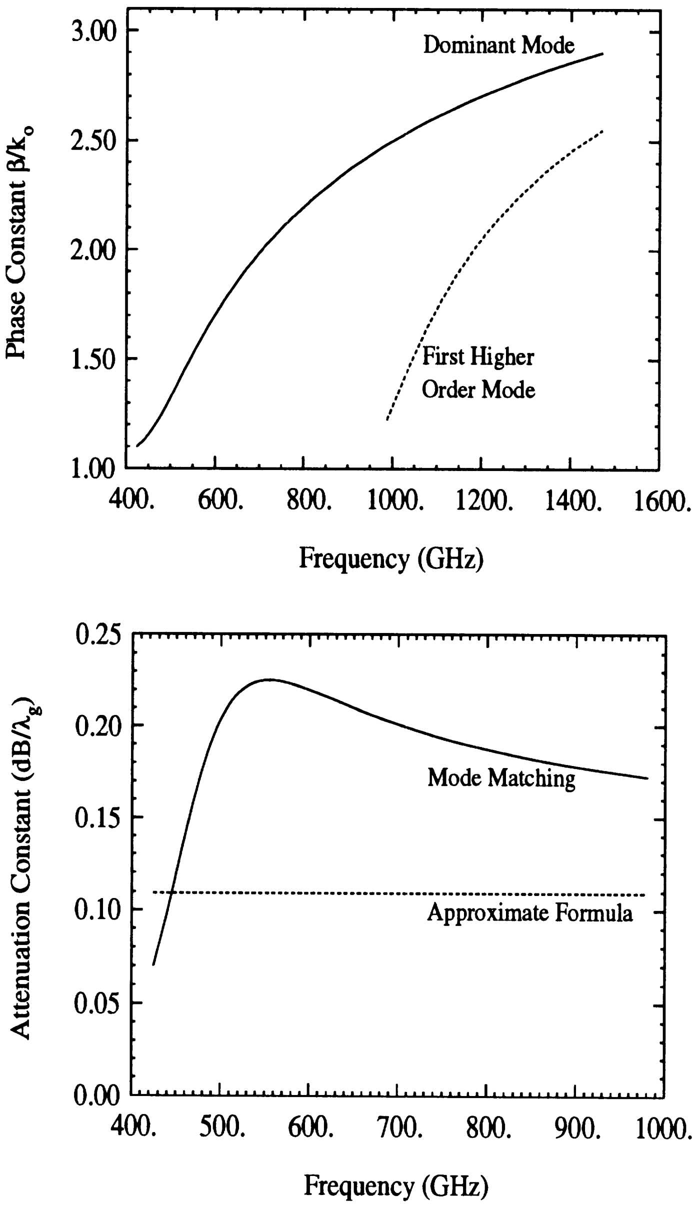

Figure 5.6: Propagation constant of the structure designed for 490 GHz. Referring to figure 5.4, $h_1 = 0.036\lambda_g$ (17.1μm), $h_2 = 0.048\lambda_g$ (22.7μm), $h_3 = 0.122\lambda_g$ (58.2μm), $w = 0.064\lambda_g$ (30.6μm) and $a = 0.965\lambda_g$ (459μm). Top: phase constant as a function of frequency with lossless dielectrics. $\epsilon_1 = 12.85\epsilon_o$ (GaAs) and $\epsilon_2 = 10.0\epsilon_o$ (AlAs). Bottom: upper bound of attenuation constant as a function of frequency with worst-case dielectric losses. $\epsilon_1 = 12.85\epsilon_o(1.0 - j0.004)$ (GaAs) and $\epsilon_2 = 10.0\epsilon_o(1.0 - j0.004)$ (AlAs).

laterally open structure. If β/k_o of the shielded structure leads to a complex determinant in the laterally open case, then the mode leaks in the open structure and the associated propagation constant γ has approximately the same phase constant as in the shielded case but also a non-zero attenuation constant.

Plots of the phase constant versus frequency for the dominant and first higher order modes of the 94 GHz structure are shown in figure 5.5. The dielectrics were assumed to be lossless for the phase constant calculations. The dominant mode has no cut-off frequency, while the first higher order mode becomes leaky at approximately 183 GHz. Similar results hold for the 490 GHz structure (figure 5.6), where the first higher order mode becomes leaky at 980 GHz.

An alternate method for assessing which modes leak and which do not has been developed by Oliner and Peng [54, 59], and this method has been applied to the design examples. The waveguide is considered as two constituent sections, namely, the inner waveguide region ($|y| < b$ in figure 5.4) and the surrounding substrate ($|y| > b$). Each propagating mode in the dielectric waveguide is based on a particular surface wave mode traveling at some angle to the z-axis in the inner constituent region. The propagating mode does not leak if the corresponding surface wave mode undergoes total internal reflection each time it hits a sidewall of the waveguide (at $y = \pm b$). A mode is leaky if the corresponding surface wave mode only partially reflects at the sidewalls; in this case, the inner surface wave mode in the inner constituent region couples to a propagating surface wave mode in the surrounding substrate. The coupling occurs when the effective index of refraction $n^{(2)}$ of the inner surface wave mode is less than the effective index of refraction $n_0^{M(1)}$ of the dominant substrate surface wave mode. The effective indices of refraction are calculated using the dispersion relation of equation 2.18 with $k_y = 0$ (since the surface wave is the wave which propagates when the region is infinite in the y-direction [35]):

$$n_l^{(j)} = \frac{\beta_l^{(j)}}{k_o} = \frac{1}{k_o}\left(\left(k^{(ij)}\right)^2 - \left(k_{xl}^{(ij)}\right)^2\right)^{1/2} \tag{5.2}$$

where $k_{xl}^{(ij)}$ is the l^{th} x-directed wavenumber in layer i of section j (see section 2.4.2) and a superscript E or M is added depending on whether a TE$_x$ or a TM$_x$ mode is considered. The results of applying this method to the 94 GHz waveguide are shown in figure 5.7, which contains a frequency plot of the effective indices of refraction of the dominant TM$_{z0}$ substrate surface wave mode ($n_0^{M(1)}$) and the dominant TM$_{z0}$ and first higher order TM$_{z1}$ inner region surface wave modes ($n_0^{M(2)}$ and $n_1^{M(2)}$) on which the dominant and first higher order waveguide modes are based. According to this plot, the dominant waveguide mode does not leak and the first higher order mode will leak (if it propagates at all) at frequencies below 130 GHz. The latter conclusion does not agree with the results of figure 5.5. The reason for the discrepancy is that this method does not include the higher mode interactions between the sides of the waveguide when the waveguide width is sufficiently small. A similar discrepancy is found when the 490 GHz waveguide is analyzed (figure 5.8).

After including losses in the dielectric layers, the attenuation constant α of the dominant mode of each structure was calculated as a function of frequency (figures 5.5 and 5.6). For simplicity, the loss tangents were taken to be the worst-case (maximum) values over the frequency ranges, so that the attenuation constants shown in the plots represent upper bounds for the actual values. A worst-case value of 0.002 for the loss tangent of the GaAs layers for frequencies below 400 GHz was obtained from [2]; extrapolation of the data in this reference provided a worst-case value of 0.004 for frequencies up to 1.0 THz. The loss tangent of AlAs was assumed to be comparable to that of GaAs; if the actual losses of AlAs are significantly higher, any material which has a lower loss tangent and is compatible with GaAs may be substituted. Polyamide, when it is prevented from absorbing moisture, is known to exhibit low losses in the sub-mm region, and its loss tangent was taken to be 0.001.

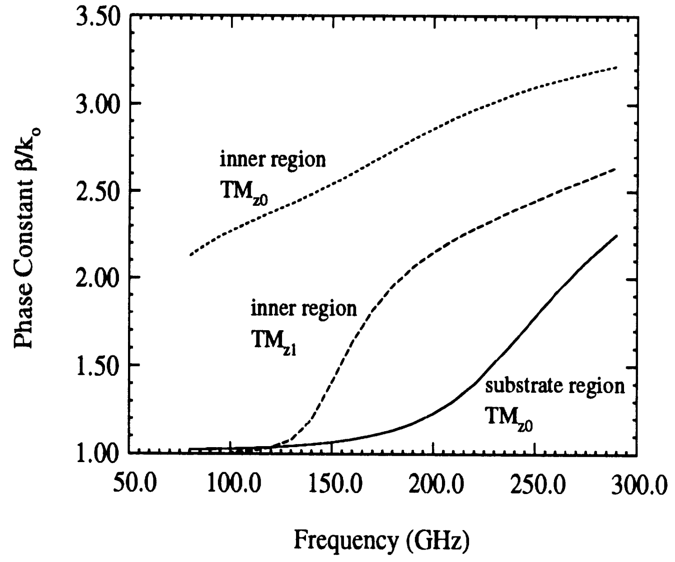

Figure 5.7: Effective indices of refraction of the lowest order surface wave modes of the constituent regions of the 94 GHz waveguide.

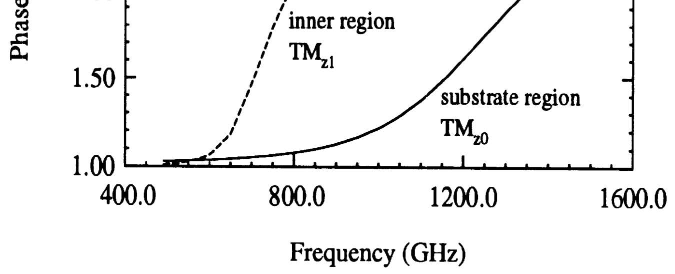

Figure 5.8: Effective indices of refraction of the lowest order surface wave modes of the constituent regions of the 490 GHz waveguide.

Approximate maximum attenuation constant values for the two examples are 0.05 dB/λ_g (18 dB/m) at 94 GHz and 0.19 dB/λ_g (400 dB/m) at 490 GHz, respectively. When the lossless and lossy cases are compared, the phase constants β do not differ significantly.

A simple estimate for the attenuation in the waveguides is obtained by assuming that $\tan\delta$ in the propagation layer is small and that all of the propagating power is contained in the propagation layer. Under these conditions,

$$k_{\text{prop. layer}} = \omega\sqrt{\epsilon_o\mu_o\epsilon_r'(1 - j\tan\delta)} \approx \omega\sqrt{\epsilon_o\mu_o\epsilon_r'}(1 - \frac{j}{2}\tan\delta) \tag{5.3}$$

and

$$k_{\text{prop. layer}} = k_z = \beta - j\alpha \tag{5.4}$$

so that

$$\alpha = \frac{\beta}{2}\tan\delta \tag{5.5}$$

Results obtained from the above formula are included in the attenuation constant plots. Comparisons of the mode matching results to the approximate results illustrate the effects of the losses in the non-propagating layers. If the propagation layer is constructed from a low-loss material (as in the 94 GHz waveguide), and if power confinement in the propagation layer is then maximized, losses are minimized. Possibly, increasing the thickness of the propagation layer could improve the power confinement.

The attenuation constants of the two waveguide structures behave differently as the frequency increases. The attenuation increases at high frequency in the 94 GHz waveguide, and the converse is true in the 490 GHz waveguide. In the next section, power density data demonstrate that less power is contained in the propagation layer as the frequency increases. In the 94 GHz waveguide, the outer layers were modeled with worst-case losses which are much higher than the losses in the propagation layer, and the attenuation constant increases as the power migrates to the outer layers. In the 490 GHz waveguide, the outer layers were modeled with worst-case losses which are the same as the losses in the propagation layer, and the variation of the attenuation constant is not unexpected in view of the assumption of frequency-independent losses.

The attenuation of the waveguides is contrasted with the attenuation of conventional rectangular waveguide and microstrip in figure 5.9. The rectangular waveguides were designed with center frequencies comparable to the design frequencies of the monolithic waveguide examples, and the attenuation of the rectangular waveguides from sidewall conductor losses was calculated in accordance with [6]. The microstrip was designed on a substrate comparable to the substrate used for the 94 GHz waveguide, and its attenuation from both conductor and dielectric losses was calculated in accordance with [78]. Due to the impracticality of microstrip at 490 GHz, the microstrip is shown only in the 94 GHz example. Although the new guiding structures do not have the extremely low attenuation exhibited by the rectangular waveguides, the new waveguides are smaller, and their monolithic nature allows for both easier construction of passive circuit elements (such as couplers, stubs, T-junctions, and inductors) and easier integration of active devices and device-waveguide transitions.

5.2.2 Field and Power Distributions

Field investigations show that both the dominant and first higher order modes are TM_z-like modes, with dominant electric field components in the x-direction. The dominant mode is very similar to a typical microstrip mode, so that the aforementioned coupling to active devices via short lengths of microstrip is achievable. The fields of the two waveguides are presented in figures 5.10–5.13.

The power density of the dominant mode of each waveguide is extremely well-confined

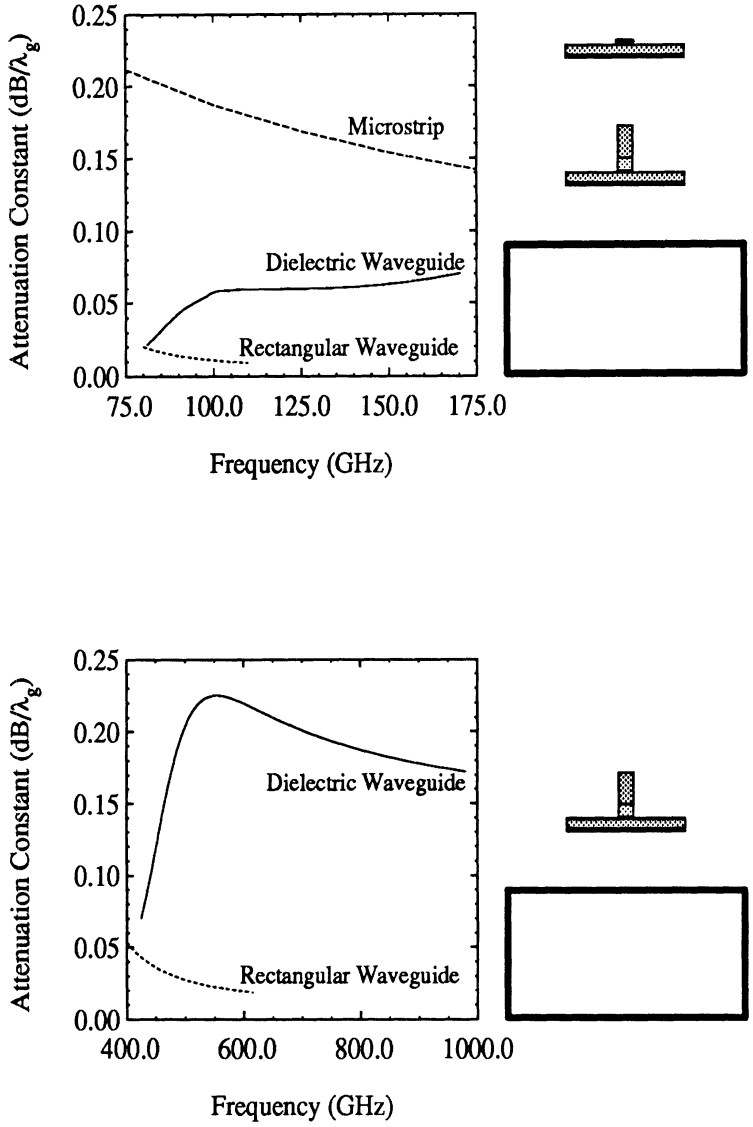

Figure 5.9: Comparisons of the attenuation of the structures of figures 5.5–5.6, rectangular waveguide and microstrip. Top: 94 GHz waveguide (figure 5.5) compared to 2.54mm by 1.27mm rectangular waveguide with gold sidewalls; and 50Ω microstrip with $h = 100\mu m$, $w = 75\mu m$, $\epsilon = 12.85\epsilon_o(1.0 - j0.002)$ (GaAs) and strip conductivity = 3.33 x 10^4 S/mm. The three guiding structures are drawn in the same scale. Bottom: 490 GHz waveguide (figure 5.6) compared to 0.488mm by 0.244mm rectangular waveguide with gold sidewalls (conductivity = 4.1 x 10^4 S/mm). The two guiding structures are drawn in the same scale.

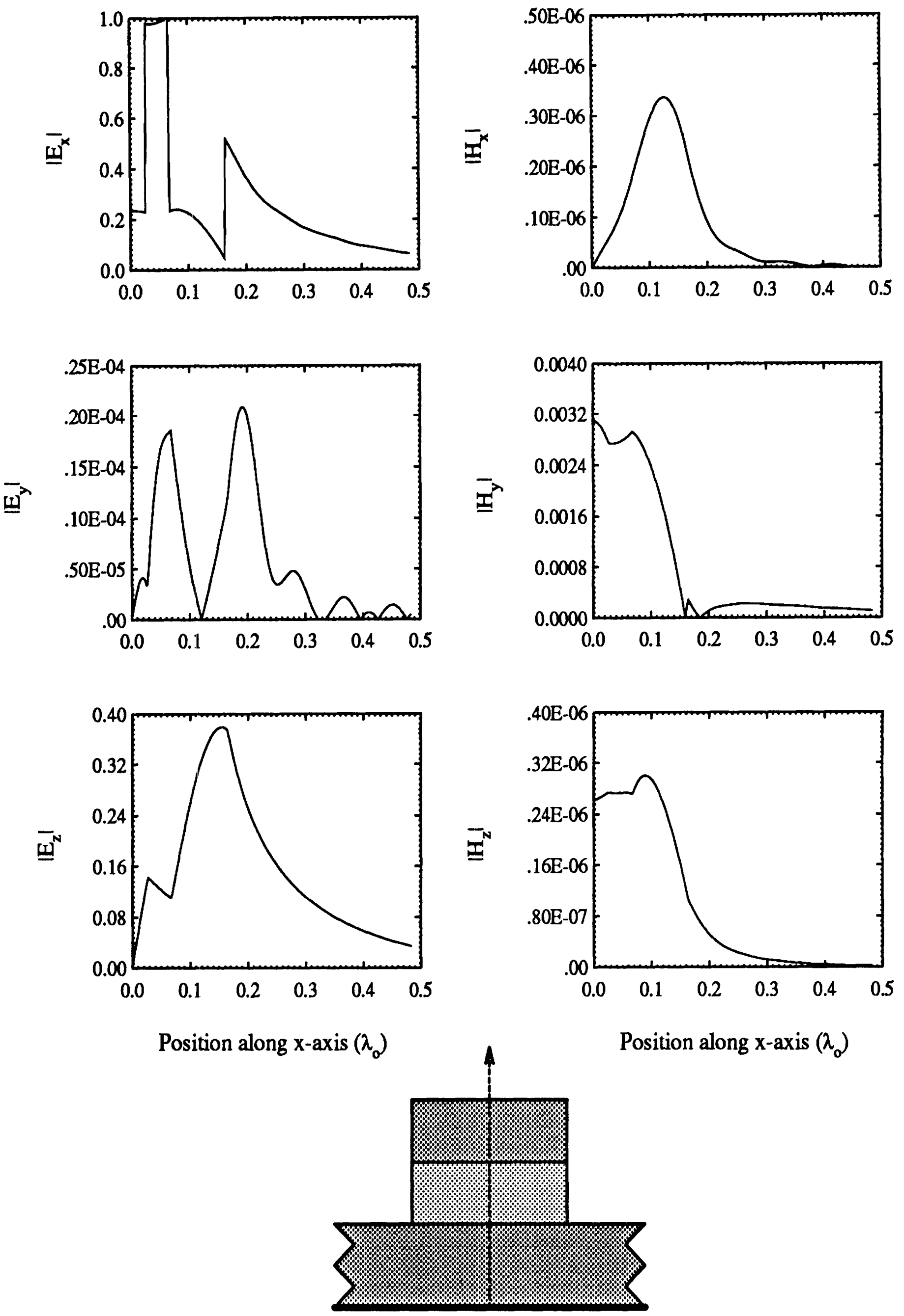

Figure 5.10: Field plots for the 94 GHz waveguide at 94 GHz along the x-axis at $y = 0$, as shown by the arrow. The geometry is described in figure 5.5.

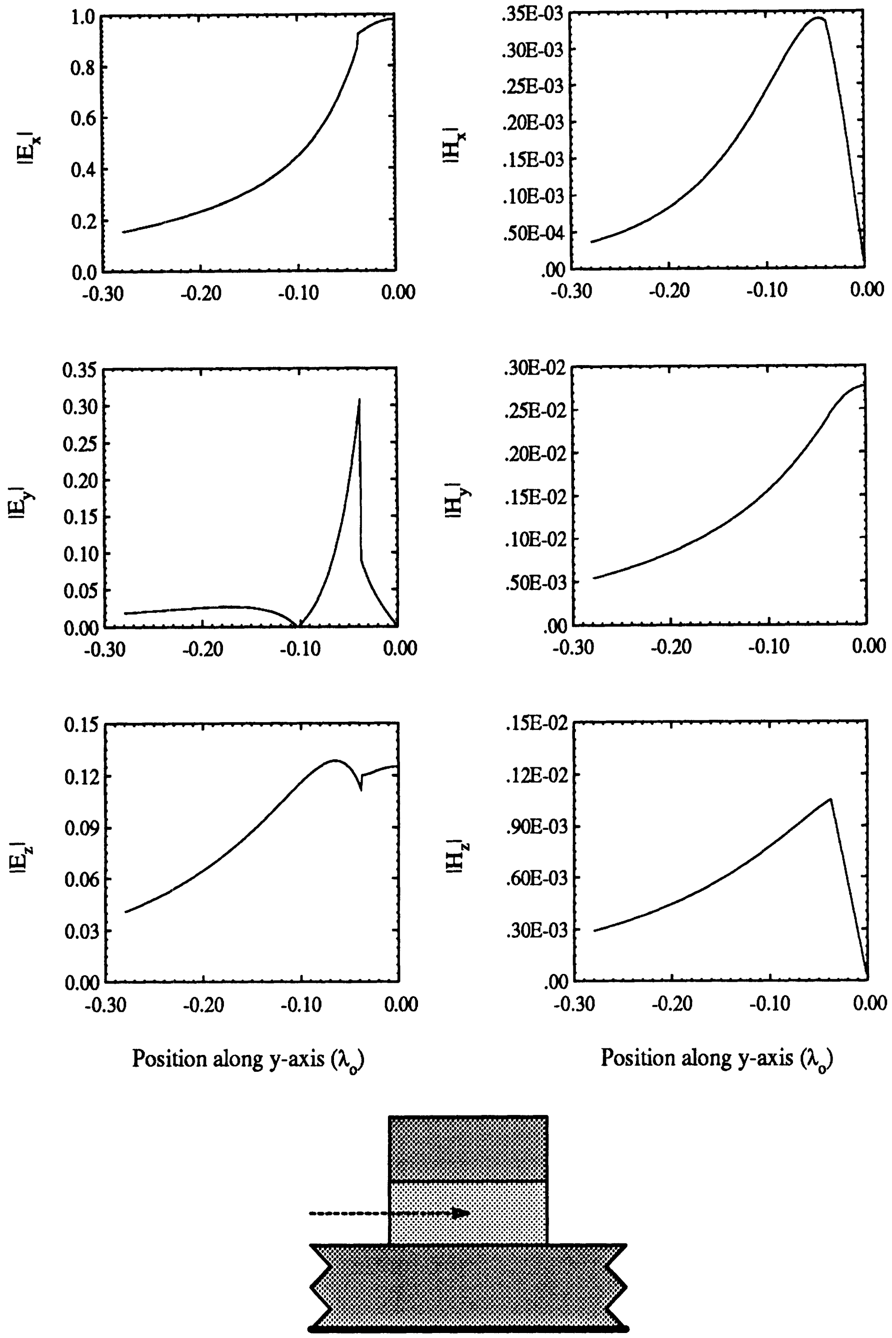

Figure 5.11: Field plots for the 94 GHz waveguide at 94 GHz along the y-axis through the middle of the propagation layer, as shown by the arrow. The geometry is described in figure 5.5.

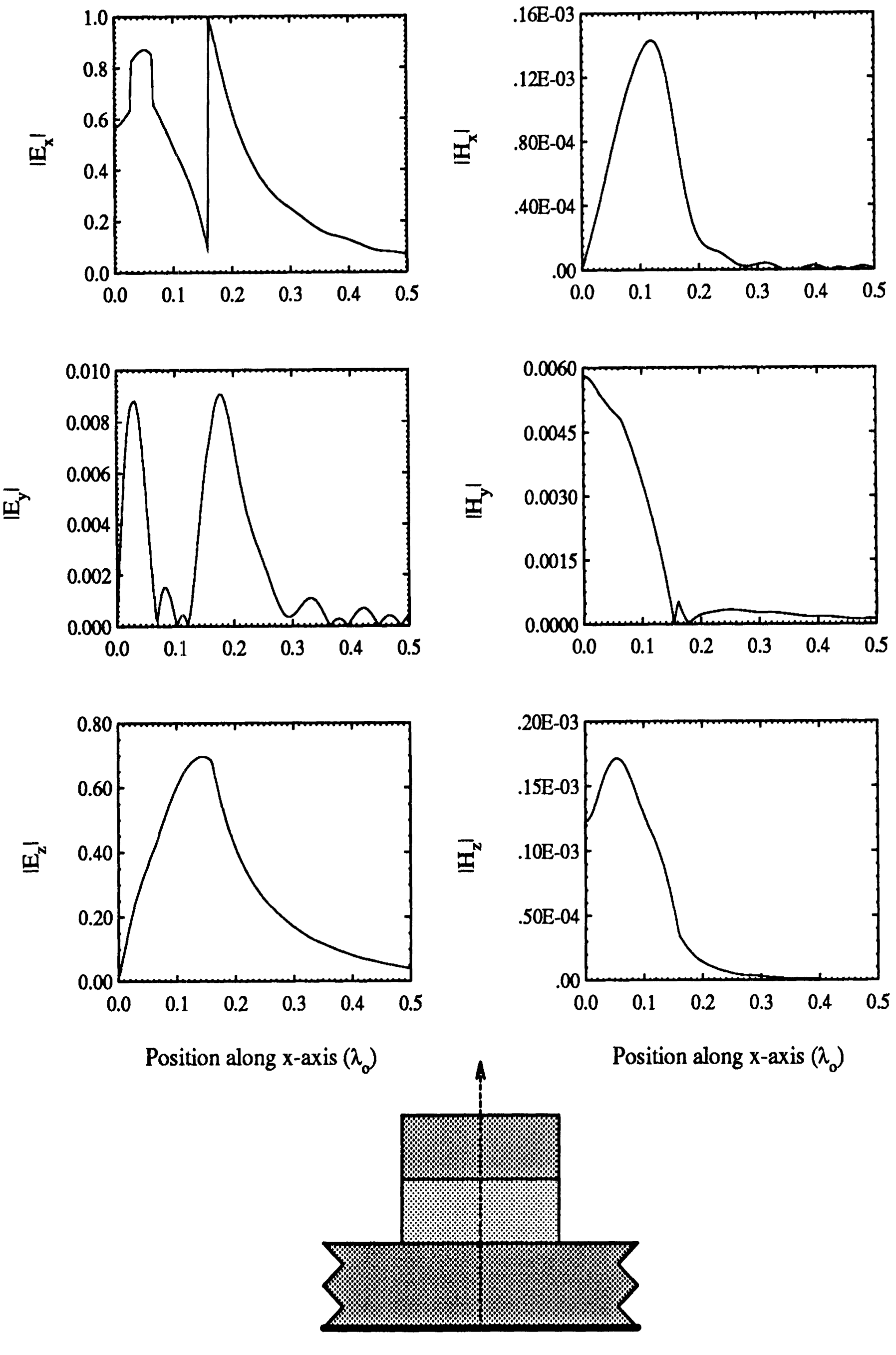

Figure 5.12: Field plots for the 490 GHz waveguide at 490 GHz along the x-axis at $y = 0$, as shown by the arrow. The geometry is described in figure 5.6.

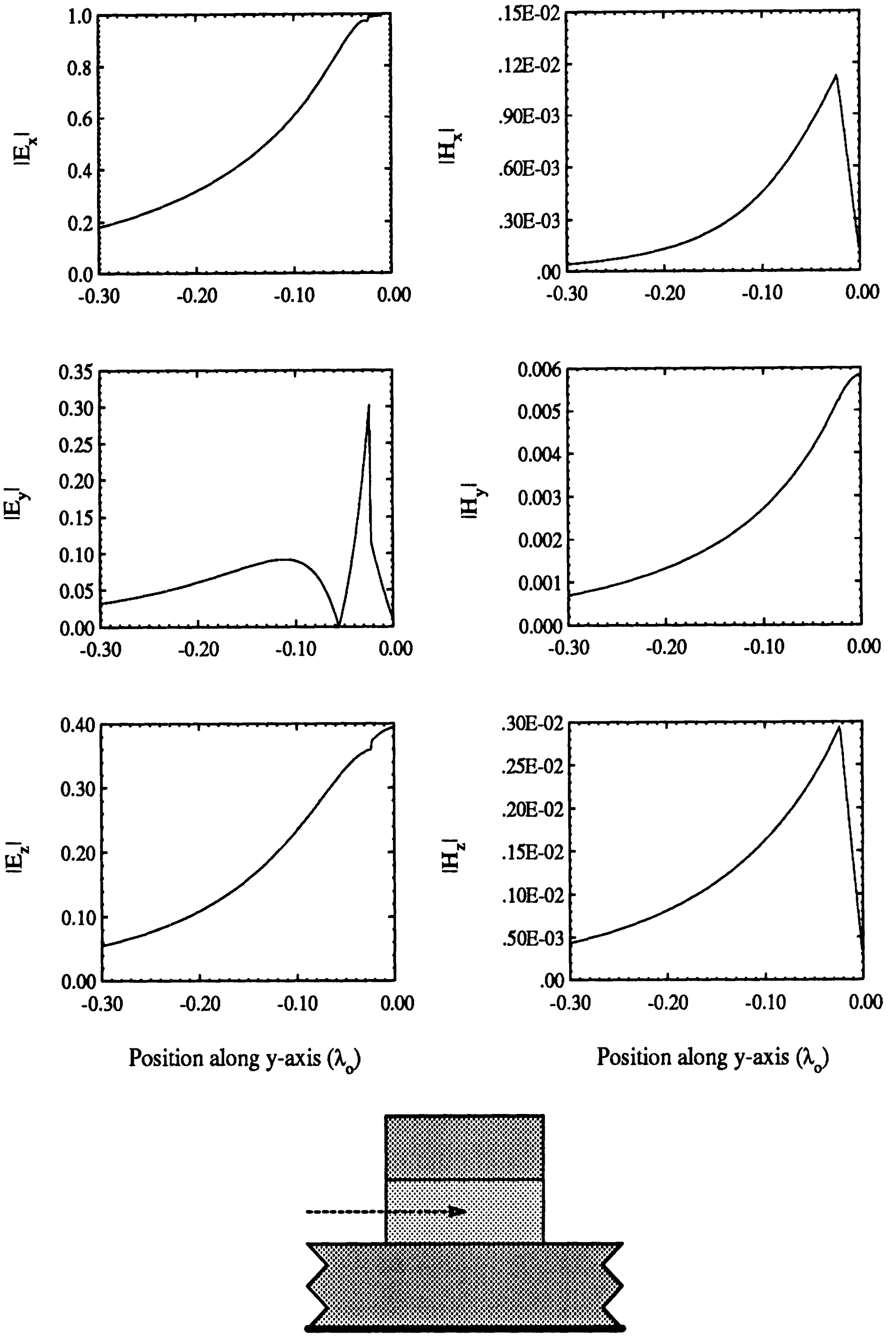

Figure 5.13: Field plots for the 490 GHz waveguide at 490 GHz along the y-axis through the middle of the propagation layer, as shown by the arrow. The geometry is described in figure 5.6.

in the respective propagation layers (figures 5.14–5.15). The power is better concentrated in the propagation layer in the latter example due to the larger contrasts between permittivities in adjacent layers.

The variation of the power density distribution with frequency is important because the advantages of the layered structure are lost when the propagation layer no longer contains a large majority of the power. The dominant mode power densities are shown at various frequencies in figures 5.16–5.17. In the 94 GHz waveguide, the power density concentrates markedly in the top layer as the frequency increases above 160 GHz. In the 490 GHz waveguide, the power density spreads into the substrate layer as the frequency increases, and, in practice, increased propagation losses due to the finite conductivity of the ground plane will result. The power density distributions set the upper limits of the useful bandwidths at lower frequencies than the limits set by higher order modes.

5.3 Summary

Low-loss monolithic waveguides have been proposed for sub-mm and THz frequency applications. Design examples for nominal frequencies of 94 GHz and 490 GHz were shown to have low losses, excellent power confinement in the propagation layer and wide unimodal bandwidth. The design examples demonstrated a general characteristic of this type of structure; namely, that the materials and structures available in monolithic technology allow the propagating power to be confined in a convenient region at a given frequency. A wide range of designs is available; a different choice of materials, dimensions and layer arrangement could yield waveguides with better power confinement and lower losses than the examples which have been presented.

An important aspect of integrating the new waveguides in monolithic circuits is the design of an active device-to-waveguide transition, and this topic is addressed in the next chapter.

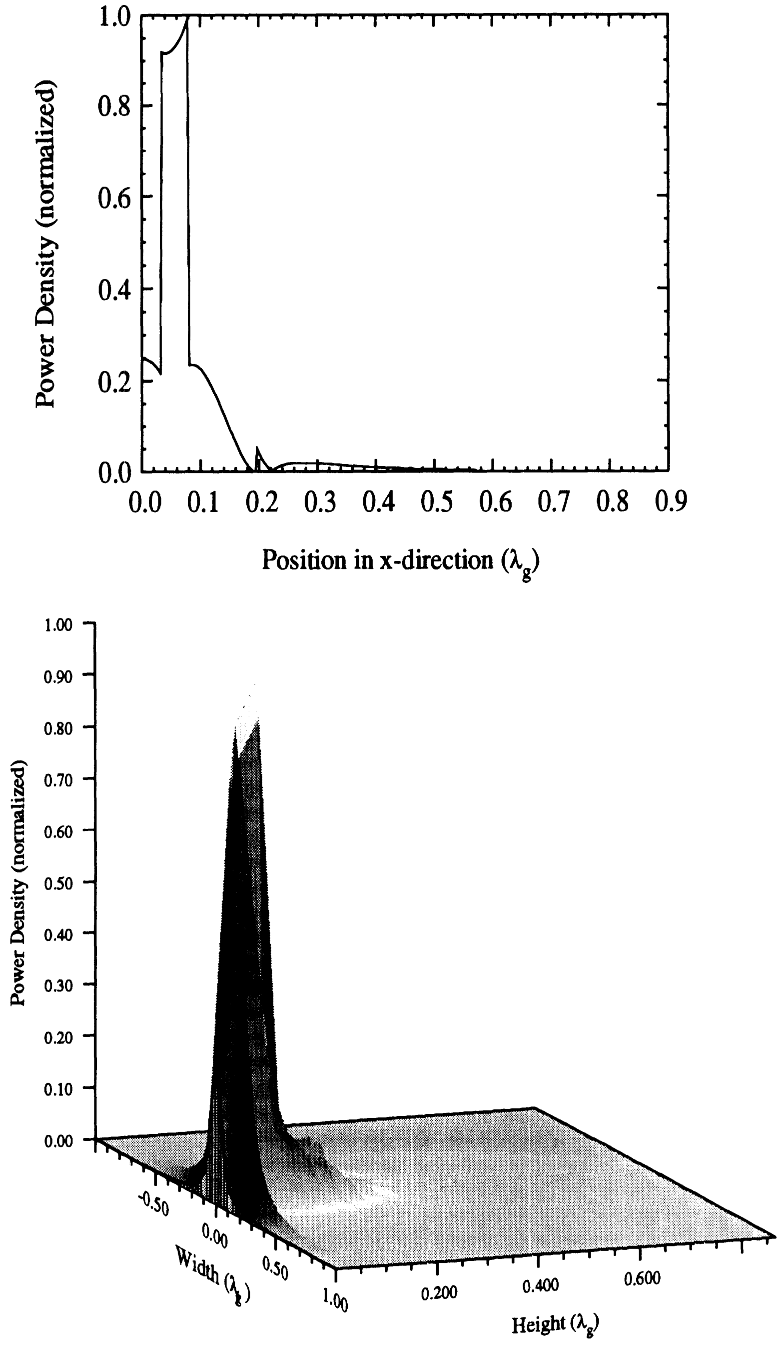

Figure 5.14: Power density of the dominant mode of the 94 GHz waveguide at 94 GHz. The geometry is described in figure 5.5. Top: power density along the x-axis at $y = 0$. Bottom: power density over the cross-section of the waveguide.

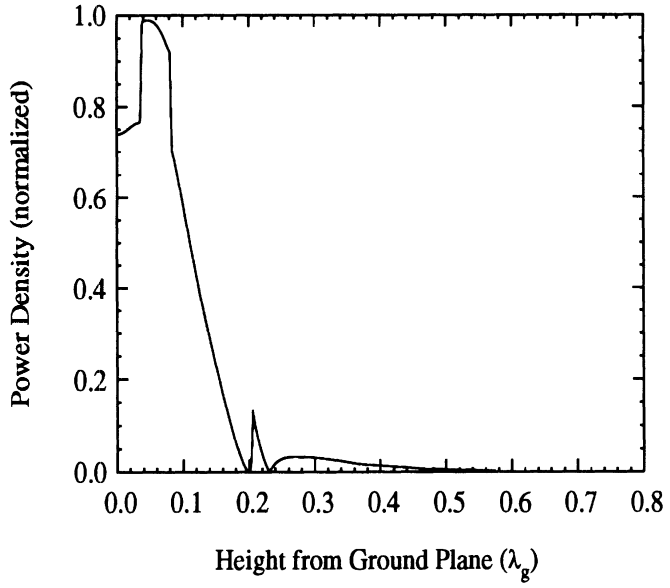

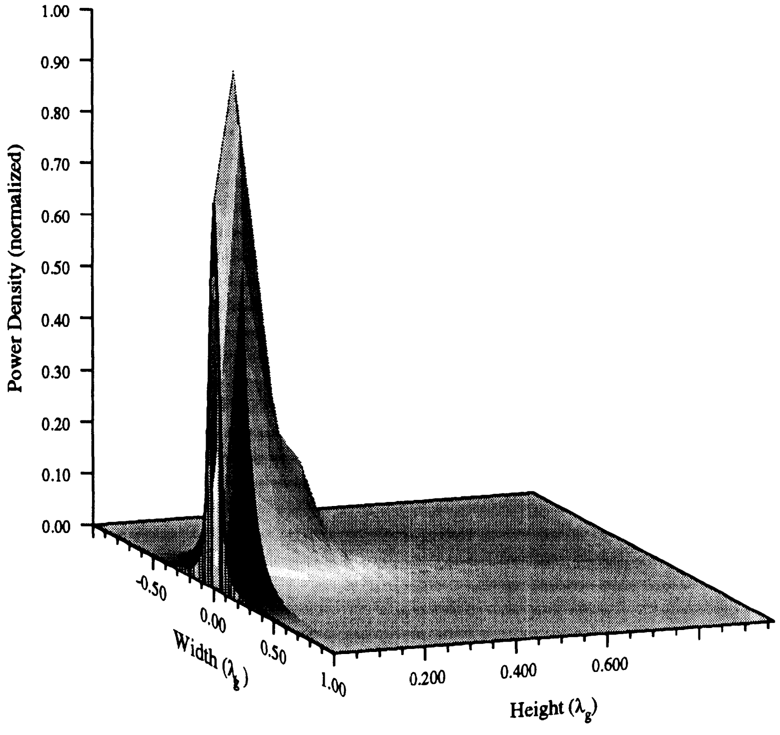

Figure 5.15: Power density of the dominant mode of the 490 GHz waveguide at 490 GHz. The geometry is described in figure 5.6. Top: power density along the x-axis at $y = 0$. Bottom: power density over the cross-section of the waveguide.

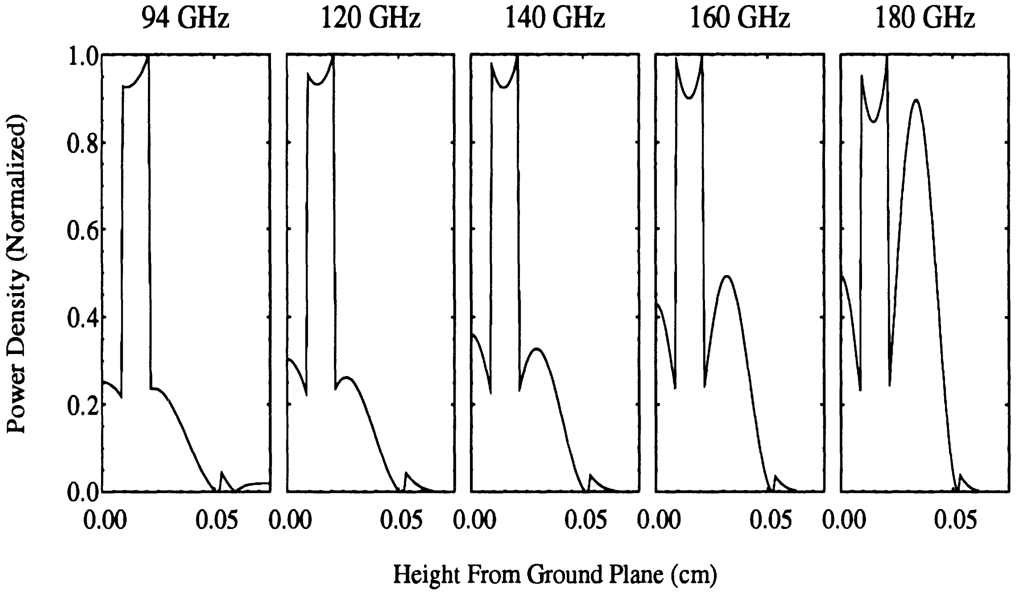

Figure 5.16: Power density of the dominant mode of the 94 GHz waveguide at various frequencies. The geometry is described in figure 5.5. The power density is plotted along the x-axis at $y = 0$.

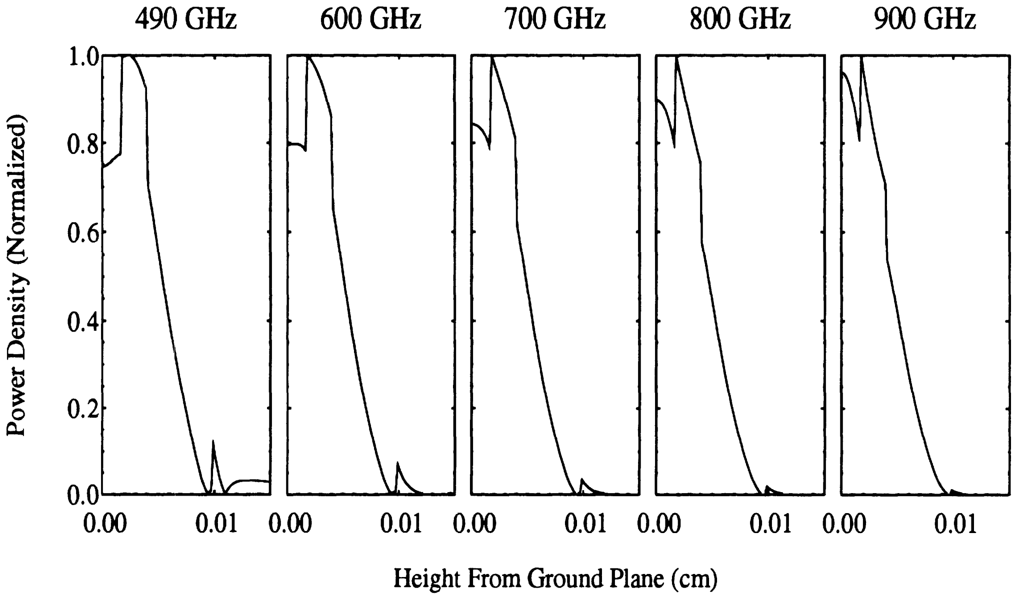

Figure 5.17: Power density of the dominant mode of the 490 GHz waveguide at various frequencies. The geometry is described in figure 5.6. The power density is plotted along the x-axis at $y = 0$.

CHAPTER VI

A SHIELDED TRANSITION TO LAYERED RIDGED DIELECTRIC WAVEGUIDE

The successful integration of dielectric waveguides and power sources into a sub-millimeter-wave or terahertz monolithic circuit relies on the design of an effective transition. In particular, when the layered ridged dielectric waveguides of chapter V are used, a transition to the waveguide is realized with a short length of conductor on top of the ridge (figures 6.1–6.2). The waveguides are often used in open environments, but, with the steadily increasing variety of applications for sub-mm and THz monolithic circuits in hermetically sealed packages, shielded environments must also be considered. In some instances, the shielding structure can support higher order modes which have significant effects on a transition's performance and add considerable complexity to characterization efforts.

Of primary interest in evaluating a transition is the power transferred from the dominant mode in the strip-ridge structure to the dominant mode in the dielectric waveguide. If only the guiding properties of either region are desired, then two-dimensional analysis is sufficient and higher order modes are easily taken into account. A propagating mode which is bound to the dielectric waveguide has a phase constant $\beta/k_o > 1$ and is not affected by the shielding as long as the shielding is far enough from the waveguide. Higher order propagating modes which are affected by the shielding correspond to modes in the open case which are either evanescent ($\beta/k_o < 1$) or leaky ($\beta/k_o > 1$, $\alpha \neq 0$). If the properties

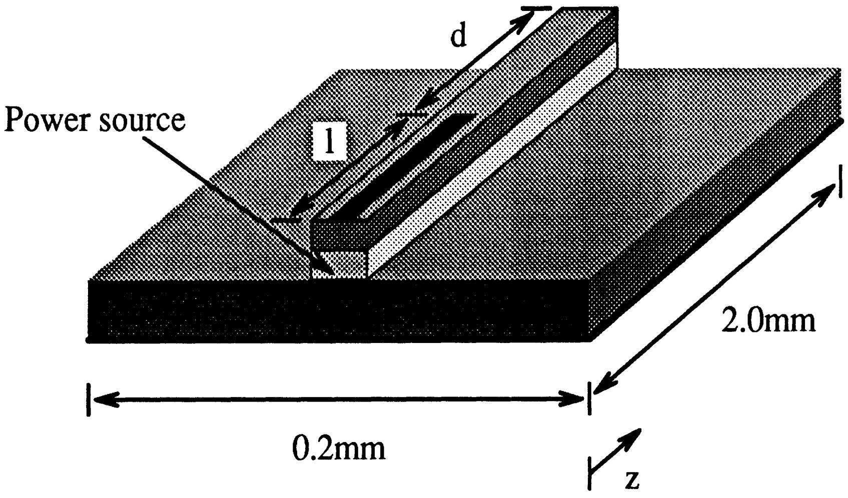

Figure 6.1: A transition between a power source and a layered ridged dielectric waveguide. The strip-ridge region has length l and the dielectric waveguide region has length d. The structure is contained in a cavity with length and width as shown; other dimensions are given in figure 6.2.

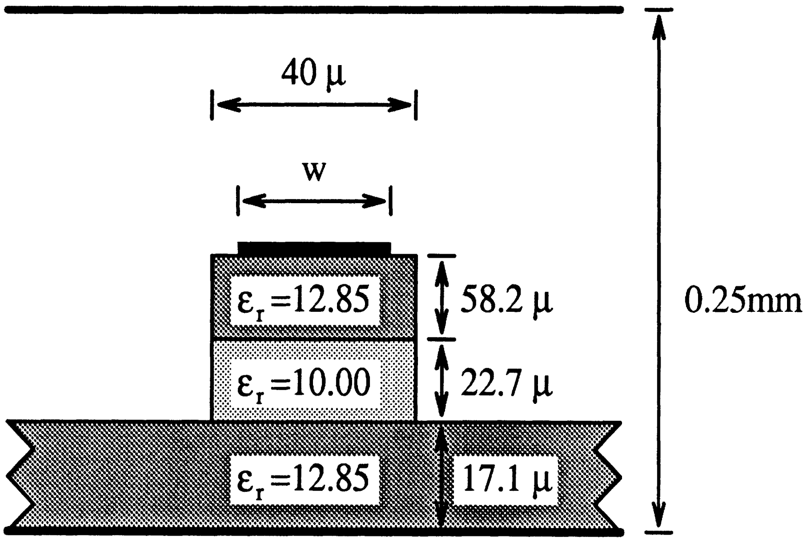

Figure 6.2: Cross-section of the strip-ridge structure. The dielectric waveguide structure is the same except there is no strip on the ridge ($w = 0$).

of a transition are desired, then three-dimensional analysis is necessary and accounting for higher order modes is difficult. An optimum shielding structure is small enough so that no higher order modes propagate in either the dielectric waveguide or the strip-ridge regions, yet large enough so that the shielding does not affect the guiding properties of the dominant modes. The two dominant modes are very similar in field distribution, but the strip-ridge dominant mode is a quasi-TEM microstrip-like mode, and, just as the first higher order mode of shielded microstrip corresponds to the dominant mode of the inhomogeneous shielding waveguide [88], the dominant mode of the dielectric waveguide corresponds to the first higher order mode of the strip-ridge structure. Difficulties arise in designing a shielding structure in which the dominant dielectric waveguide mode propagates and the first higher order strip-ridge mode does not.

A thorough characterization of a transition is presented in this chapter by employing all three of the numerical methods which were described in chapter II. Specifically, while higher order modes are considered, a simple method for determining the transition's circuit model (i.e., two-port scattering matrix) from the full-wave results is implemented and the electrical performance is studied as frequency and conductor width are varied.

6.1 Determining the Circuit Model from the Strip Currents

Two-port discontinuities in high-frequency guiding structures can be divided into two categories: those with like guiding structures at each port, as in microstrip or coplanar waveguide gap and step discontinuities, a waveguide step discontinuity, or a dielectric obstacle in a waveguide; and those with unlike guiding structures at each port, as in the transition of figure 6.1 where a microstrip-like structure is at one port and a dielectric waveguide is at the other. When the lines at each port are microstrip or coplanar waveguide, a common approach is to characterize the two-port from the currents on the strips or the fields in the slots using even and odd excitations [20, 43]. When the lines at each port are waveguides, the fields in the entire structure are used in the characterization, either by exciting one port and directly examining the fields at each port [85] or by placing a short at one port at various distances away from the discontinuity, exciting the other port, finding the nulls in the standing wave and applying the tangent method [15, ch. 5]. Since the strip currents are determined directly from the IEMM method (chapter II) and the IEMM method does not allow for convenient excitation of the dielectric waveguide port, a practical characterization technique is similar to the tangent method.

6.1.1 Input Reflection Coefficient

The transition's circuit model depends on the input reflection coefficient Γ_{in} of the dominant mode of the strip current. The structure consists of three parts: the strip-ridge transmission line, the discontinuity, and the dielectric waveguide which is terminated by a short at the end of the cavity. All power which flows from the strip-ridge structure into the dielectric waveguide is reflected at the end of the cavity, so if the dominant mode of current is the only propagating mode on the strip-ridge structure, then $|\Gamma_{\text{in}}| = 1$. The existence of higher-order evanescent modes is not excluded by this assumption; these modes are excited at both the discontinuity and the generator and distort the standing wave pattern from its classical form. The dominant mode's contribution to the standing wave pattern consists of two oppositely directed waves, a^+ and a^-, given by

$$a^+ = |a|\, e^{-j(\beta(z-l)-\theta^+)} \tag{6.1}$$

$$a^- = |a|\, e^{j(\beta(z-l)+\theta^-)} \tag{6.2}$$

where the waves are of equal magnitude, β is the dominant mode strip-ridge phase constant and l is the length of the conducting strip. These waves are extracted from the standing wave pattern with the least squares Prony's method [49]. Since each mode's propagation constant is determined from the two-dimensional IEMM method, an appropriate version of Prony's method uses this *a priori* knowledge to generate an overdetermined system of linear equations which are solved for the amplitudes and phases of the two waves associated with each mode. The dominant mode input reflection coefficient is then determined from basic transmission line theory to be

$$\Gamma_{\text{in}} = -e^{j(\theta^{-}-\theta^{+})} \tag{6.3}$$

6.1.2 S-Parameter Model

The circuit model of the transition consists of a two-port scattering matrix S_{mn}. The tangent method in its original form provides a graphical solution to this type of characterization problem; a numerical version of the technique is adapted here. If only the dominant modes propagate in the strip-ridge and dielectric waveguide, then S_{mn} and Γ_{in} are related by [16]

$$\Gamma_{\text{in}} = S_{11} - \frac{S_{12}\,\Gamma_D\,S_{21}}{\Gamma_D S_{22} - 1} \tag{6.4}$$

where $\Gamma_D = e^{-j2\beta_D d}$, d is the length of dielectric waveguide from the discontinuity to the end of the cavity, the S-parameters are of the form $S_{mn} = |S_{mn}|e^{j\theta_{mn}}$, and β_D is the propagation constant of the dielectric waveguide's dominant mode. The mode matching technique of section 2.7 is used to determine β_D. Again, the presence of evanescent higher order modes in the dielectric waveguide is not excluded, but these modes must decay sufficiently over the length $2d$ for equation 6.4 to be valid. Reciprocity and power conservation can be used to show that the three quantities $|S_{11}|$, θ_{11}, and θ_{22} completely determine the S-parameters [16] by

$$|S_{11}| = |S_{22}| \tag{6.5}$$

$$|S_{12}|^2 = 1 - |S_{11}|^2 \tag{6.6}$$

$$\theta_{12} = \frac{1}{2}(\theta_{11} + \theta_{22} + \pi) \tag{6.7}$$

$$S_{21} = S_{12} \tag{6.8}$$

A non-linear system of three equations is created from equation 6.4 by determining values of Γ_{in} at three dielectric waveguide lengths, d_1, d_2 and d_3. After choosing d_1 and d_2 such that $\Gamma_{\text{in}}(d_1) = 1$ and $\Gamma_{\text{in}}(d_2) = -1$, the first two equations can be used to derive the following expressions:

$$|S_{11}| = \frac{\sin(\theta_{11} + \theta_{22} + \theta_{D1})}{\sin \angle S_{11} + \sin(\theta_{22} + \theta_{D1})} \tag{6.9}$$

$$\cos \angle S_{11} = \frac{\sin(\theta_{22} + \frac{1}{2}(\theta_{D1} + \theta_{D2}))}{\sin \frac{1}{2}(\theta_{D1} - \theta_{D2})} \tag{6.10}$$

where $\Gamma_D(d_i) = e^{j\theta_{Di}} = e^{-j2\beta_D d_i}$. These equations are used to eliminate $|S_{11}|$ and $\angle S_{11}$, and Newton-Raphson iteration [60, ch. 9] is then used to determine $\angle S_{22}$ numerically from the third equation.

6.2 Mode Diagrams of the Strip-ridge and Dielectric Waveguide Regions

Before describing the performance of the transition, the mode diagrams of the strip-ridge and dielectric waveguide regions are presented so that the transfer of power between the two dominant modes can be accurately assessed. The dimensions of the structure are given in figures 6.1–6.2.

The mode diagram of the shielded dielectric waveguide (figure 6.3) shows a single propagating mode which is bound to the dielectric ridge in the range 500–525 GHz. The shielding has little effect on the dominant mode when $\beta/k_o > 1.1$; but the dominant mode drops off much more sharply than in the laterally open case (chapter V) as β/k_o approaches 1.0. A "backward mode" and a "complex mode pair" [56] also stem from the proximity of the enclosure. The backward mode, whose energy flows in a direction opposite to the direction of the wavefronts, exists from 475–500 GHz. The complex mode pair, which is characterized by complex conjugate propagation constants of opposite sign ($\gamma = \alpha \pm j\beta$) and carries only a net reactive power, exists from 475 GHz down to at least 400 GHz.

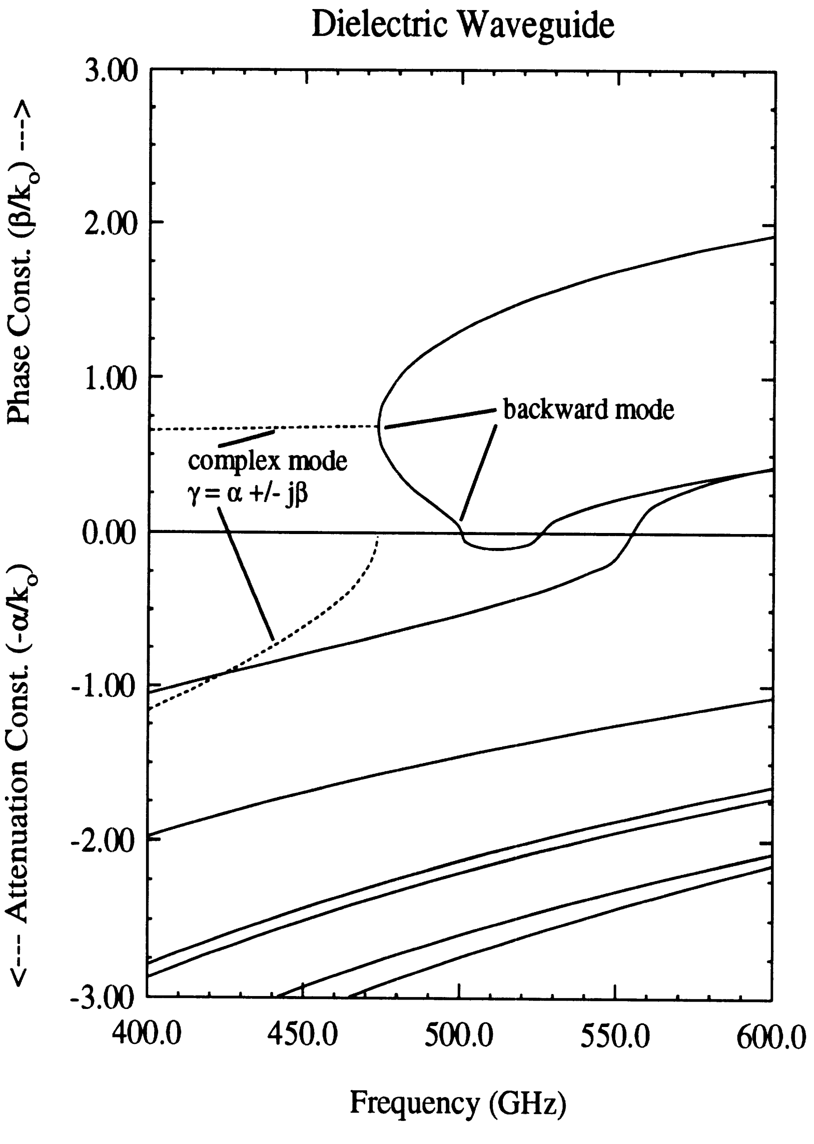

Figure 6.3: Modes of the layered ridged dielectric waveguide.

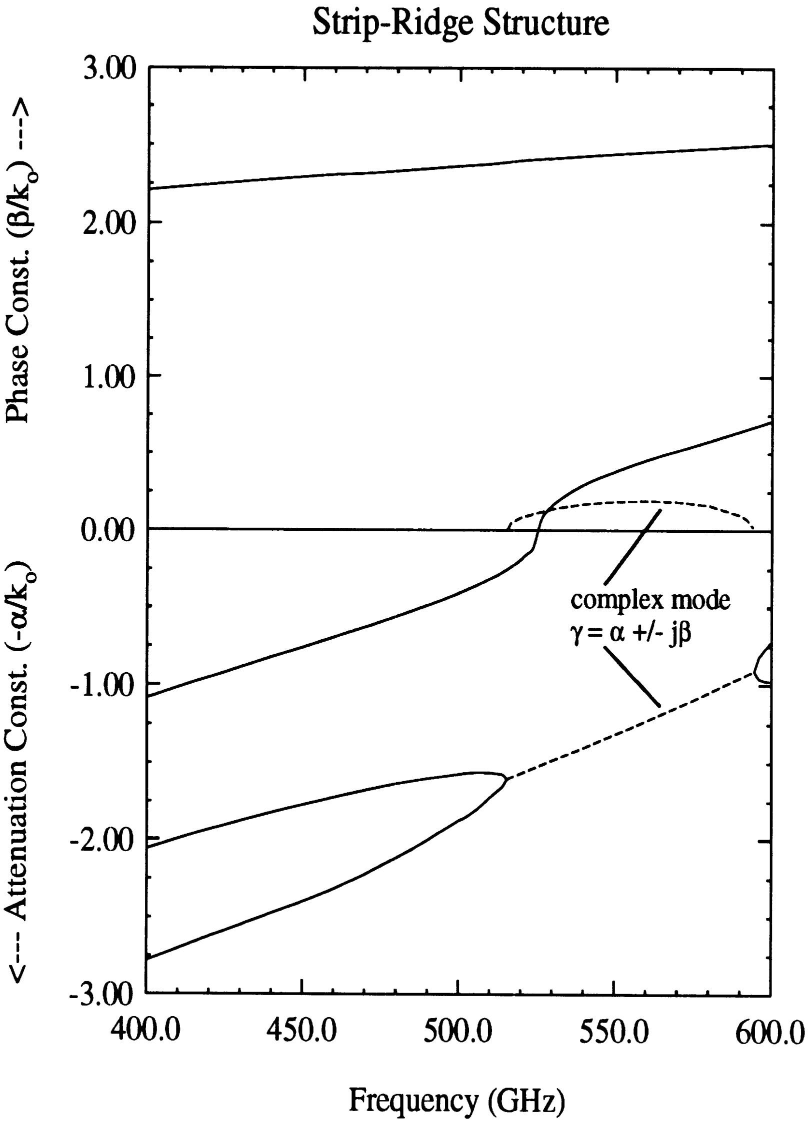

Figure 6.4: Modes of the strip-ridge structure.

The mode diagram of the strip-ridge structure (figure 6.4) was determined using the two-dimensional IEMM method. The dominant microstrip-like mode has no cut-off frequency. A complex mode exists from 510–595 GHz, and a second mode begins to propagate at 525 GHz.

Of particular importance in the mode diagrams is the range in which each structure propagates a single mode. The presence of higher order propagating modes can hinder the efficient transfer of power through the transition. Because of the strong similarity to the dominant dielectric waveguide mode, the first higher order propagating mode in the strip-ridge structure is not easily suppressed by reducing the shielding dimensions. Only a limited range of frequency and shielding dimensions exists in which only the dielectric waveguide mode is propagating in the ridge ($\beta/k_o > 1$) and the first higher order strip-ridge mode is evanescent ($\beta/k_o < 0$). The shielding dimensions were chosen to maximize the single-mode bandwidth, which, as shown in the mode diagrams, is 500–525 GHz. An example of the minimal interaction between the shielding and the dominant dielectric waveguide mode is given in figure 6.5; comparing this figure to the power density distribution of the laterally open waveguide (figure 5.15) and accounting for the differences in scale shows that the shielding causes negligible distortion in the dominant mode.

6.3 Results of the Input Reflection Coefficient Calculations and Validation of the S-Parameter Model

The accurate determination of the phase of the input reflection coefficient depends on an accurate fit to the strip currents. The strip currents which were calculated with the three-dimensional IEMM method are compared to the currents which were fitted to the IEMM values with Prony's method in figures 6.6 and 6.7. At the generator ($z = 0$) and the end of the strip ($z = l$), higher order modes are excited. Since Prony's method uses a least squares fit and only the dominant mode of current needs to be characterized, the fit has

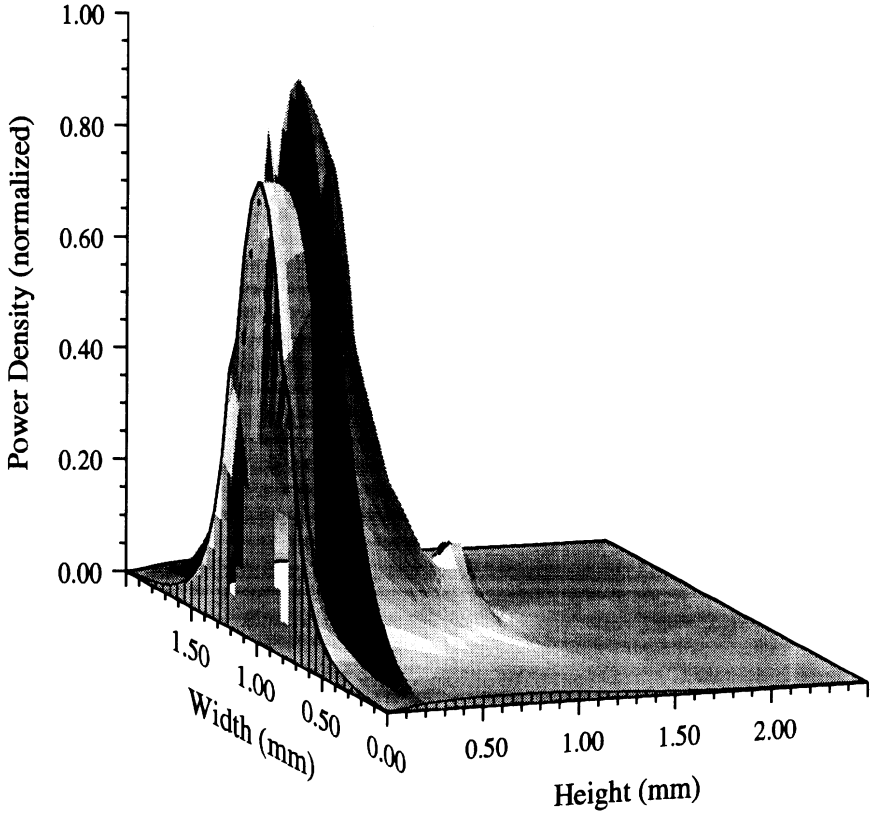

Figure 6.5: Power density distribution of the dominant mode of the dielectric waveguide at 510 GHz.

greater accuracy with fewer terms (i.e., strip-ridge modes) when Prony's method is applied away from the strip ends. In the figures, the fit from Prony's method was generated with only data points which were at least $0.11\lambda_o$ away from each end. Even so, fits using one to three modes yielded increasing degrees of accuracy. At this frequency (500 GHz), only the dominant mode is propagating and all other modes are evanescent. The two lowest order evanescent modes have a slight effect on the current fit at each end. The effect of the higher order modes on the quantity of interest, $\angle\Gamma_{\mathrm{in}}$, is also small but noticeable; $\angle\Gamma_{\mathrm{in}}$ is erroneous by about 5^o when only the dominant mode is used in the fit. Additional modes beyond the third mode do not change $\angle\Gamma_{\mathrm{in}}$ by more than $\pm 0.5^o$. The effect of the evanescent modes on the fit diminishes when larger distances are taken from the strip ends; however, when too much distance is taken, not enough of the waveform remains for an accurate fit. A short strip is advantageous for the IEMM method because discretization and cavity length are minimized—decreased discretization accelerates the method of moments solution and minimal cavity length decreases the required number of longitudinal modes.

The accurate values of Γ_{in} are used to determine S_{mn}. The S-parameter model is valid if, based on the three values of $\Gamma_{\mathrm{in}}(d)$, the model can predict Γ_{in} over a wide range of dielectric waveguide lengths d for a given cavity length. The available values of d are limited: if d is too short, the evanescent modes will not decay sufficiently and equation 6.4 will not be valid; if d is too long, the conducting strip is too short and the distortion of the strip current's standing wave pattern precludes accurate determination of Γ_{in}. For example, the S-parameter model is shown to predict Γ_{in} very accurately at 510 GHz in figure 6.8 for $1.0\mathrm{mm} < d < 1.5\mathrm{mm}$. Similar results are found whenever a single mode propagates in each region (500–525 GHz). In addition, the model was found to accurately predict Γ_{in} in the ranges 480–500 GHz and 525–540 GHz; in these ranges, the higher order propagating modes are evidently not strongly excited.

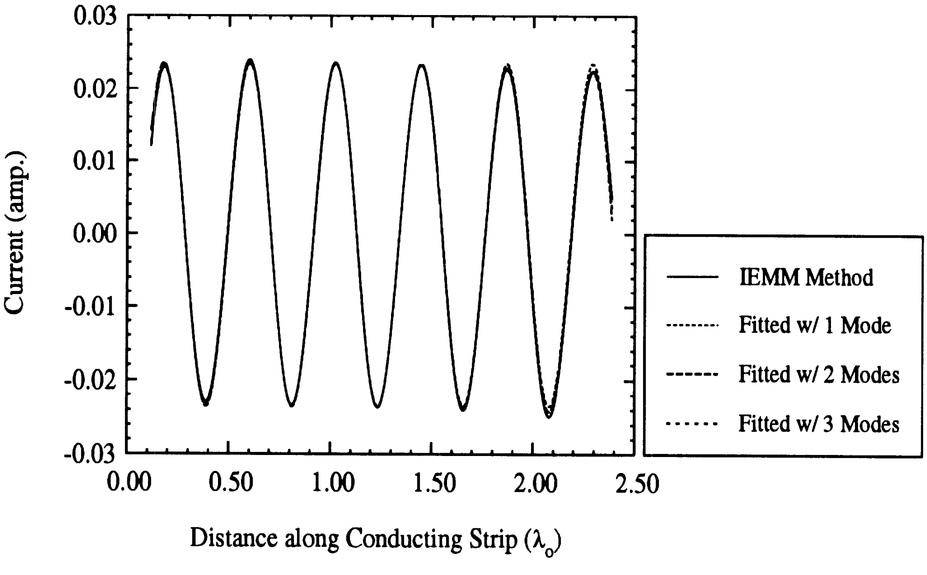

Figure 6.6: Currents on the conducting strip at 500 GHz. The strip length is 1.5mm ($= 2.5\lambda_o$), and the currents within 0.07mm ($= 0.11\lambda_o$) of each end are not shown.

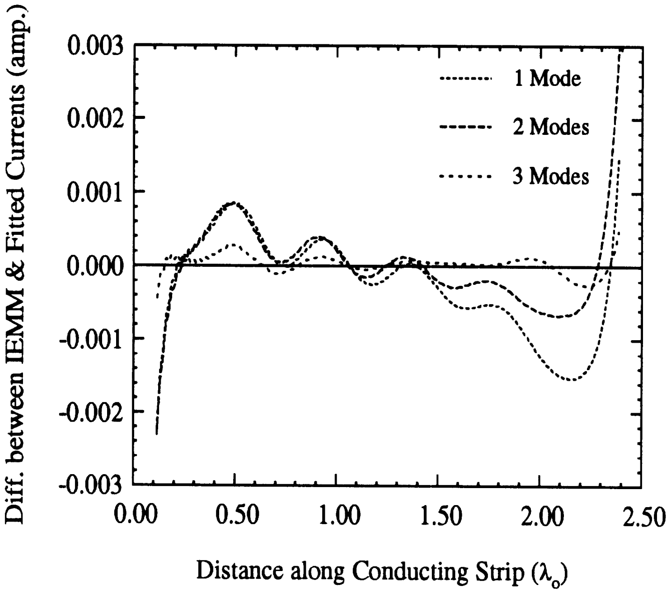

Figure 6.7: Difference between the IEMM and the fitted currents on the conducting strip at 500 GHz, determined from the results of figure 6.6.

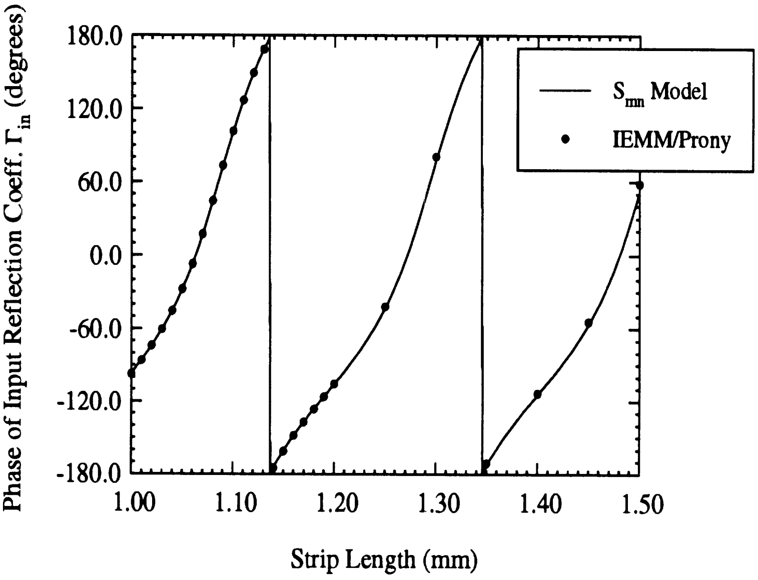

Figure 6.8: Validation of the S-parameter model at 510 GHz.

6.4 Electrical Performance of the Transition

The magnitudes and phases of the S-parameters for frequencies 480–540 GHz are shown in figures 6.9–6.10. As the frequency increases from 480 GHz, the phase constant of the guided mode in the dielectric waveguide increases from $\beta/k_o = 1.0$, and the amount of power $|S_{12}|$ transferred to the dielectric waveguide increases. In general, the transition is very efficient over a broad frequency range.

The effects of varying the width at 510 GHz are shown in figures 6.11–6.12. Since these data were generated when the conductor geometry was varied while the dielectric support structure and frequency remained constant, the decoupling property of the IEMM method was applied to substantially reduce computer run-times. At this frequency, the width has only a very small effect on $|S_{12}|$, $|S_{11}|$, and $\angle S_{12}$, but $\angle S_{11}$ and $\angle S_{22}$ vary by 40° over the range of widths.

The characteristic impedance Z_c of the strip-ridge structure is important when designing a matching network for the power source, and Z_c is plotted versus conductor width at 510 GHz in figure 6.13. As the conductor width increases to 3/4 of the ridge width,

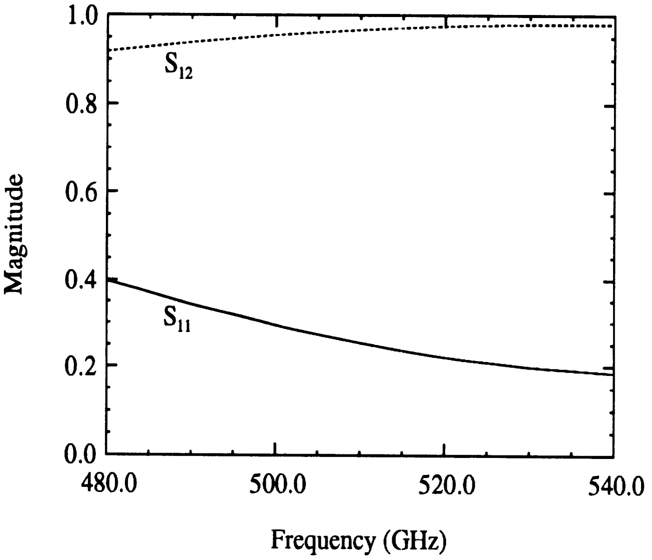

Figure 6.9: Magnitude of the S-parameters vs. frequency with conducting strip width w = 35 μm.

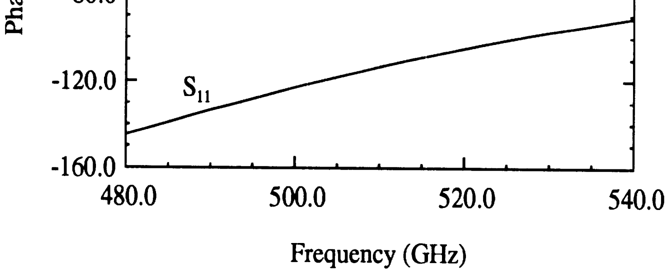

Figure 6.10: Phase of the S-parameters vs. frequency with conducting strip width w = 35 μm.

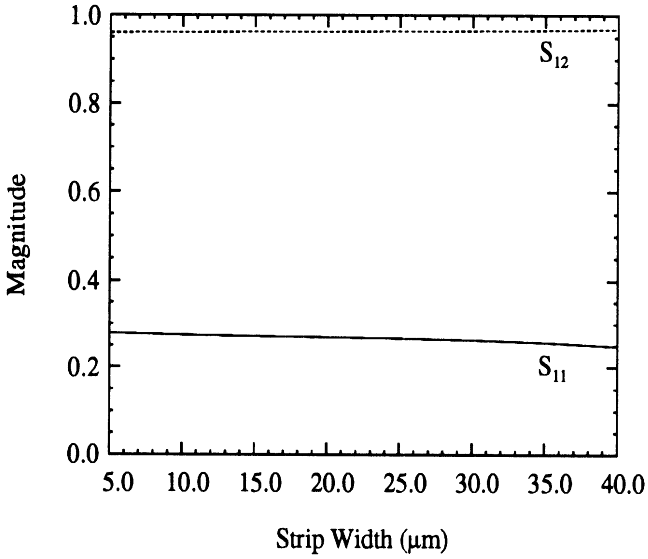

Figure 6.11: Magnitude of the S-parameters vs. the width of the conducting strip at 510 GHz.

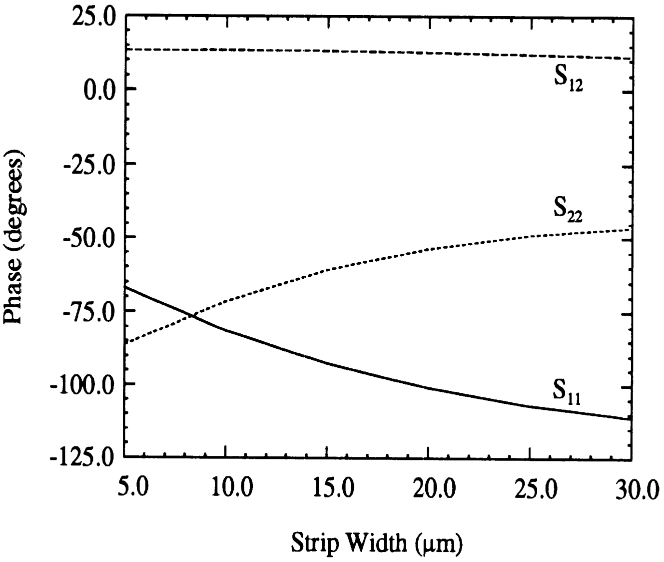

Figure 6.12: Phase of the S-parameters vs. the width of the conducting strip at 510 GHz.

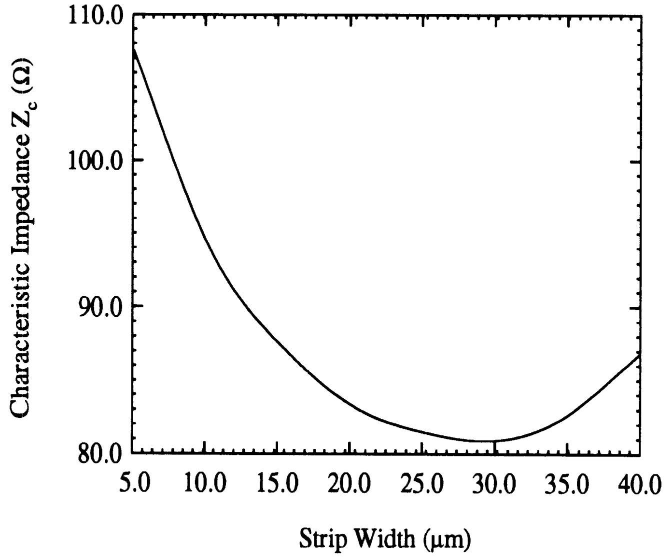

Figure 6.13: Characteristic impedance of the strip-ridge structure vs. the width of the conducting strip at 510 GHz.

Z_c decreases from 108Ω to 81Ω. This behavior is similar to the decrease in conventional microstrip characteristic impedance with increasing strip width. As the strip width increases further, the fringing fields are significantly affected by the edge of the ridge and Z_c increases to 87Ω when the strip completely covers the ridge. The variation of Z_c and the consistency of $|S_{21}|$ with strip width is useful when matching to the power source; the strip width at which Z_c is optimal can be chosen without concern for adverse affects on $|S_{21}|$.

6.5 Summary

A shielded transition from a power source to a layered ridged dielectric waveguide has been characterized. The presence of higher order modes due to the shielding was considered while a simple model was applied to determine the transition's S-parameters. The variation of the S-parameters over frequency and conductor width was presented, and the transition was found to be very efficient over a wide frequency band and a broad range of widths. The characteristic impedance of the strip-ridge structure was found to vary considerably with conductor width, thus allowing some design latitude when matching to a power source.

CHAPTER VII

CONCLUSIONS AND RECOMMENDATIONS FOR FUTURE WORK

7.1 Conclusions

The contribution of this work to the field of high frequency numerical modeling of passive components has three main aspects: the development of the IEMM method, the study of strip-ridge structures, and the design of low-loss layered ridged dielectric waveguides for monolithic sub-millimeter wave and terahertz frequency applications.

The successful development of the IEMM method is notable for several reasons:

- Unlike previous formulations of full-wave integral equation methods which solve for the currents on the conducting strips, the IEMM method is capable of characterizing nonplanar strip-ridge structures.

- The hybrid nature of the IEMM technique allows for the analytical decoupling of a nonplanar structure into its constituent conducting strips and supporting dielectrics, and, because of this decoupling, the IEMM method is especially appropriate for the characterization of three-dimensional structures in which the uniformity of the dielectric support structure along the longitudinal direction is preserved. When these structures are analyzed, the dielectric support structure is taken into account by the mode matching portion of the technique, and the integral equation can then be efficiently solved with the method of moments for any configuration of conductors.

- The IEMM method is versatile—any dielectric support structure which can be modeled with rectangular step-inhomogeneities can be combined with any variety of nonplanar conducting strips.
- The IEMM method requires that only the conducting strips be discretized, and this area usually represents only a small portion of the structure. Many other techniques which are capable of characterizing nonplanar strip-ridge structures require the discretization of all of the interfaces between regions or, in some cases, the entire structure.

The IEMM method was applied to the frequency and time domain characterization of a variety of nonplanar two-dimensional structures, namely, coupled microstrip on dielectric ridges, coupled microstrip with an etched groove, microstrip with finite substrate and ground plane, coupled multilevel microstrip with a finite intermediate dielectric layer, and an integrated electro-optic modulator. Grooves, ridges and layers in the dielectric support structure were shown to affect the coupling between conducting strips, depending greatly on the geometry. The results introduced new methods for increasing packing density, decreasing crosstalk and enhancing coupling in VLSI, monolithic and hybrid applications.

Low-loss monolithic waveguides were proposed for sub-mm and THz frequency applications. Design examples for nominal frequencies of 94 GHz and 490 GHz were shown to have low losses, excellent power confinement in the propagation layer and wide unimodal bandwidth. The design examples demonstrated that the materials and structures available in monolithic technology allow the propagating power to be confined in a convenient region at a given frequency.

An effective shielded transition between the layered ridged dielectric waveguides and power sources for a sub-millimeter-wave or terahertz monolithic circuit was shown to consist of a short length of conductor on top of the ridge. The shielding dimensions proved to be critical in minimizing the effects of higher order modes. While these effects were considered, a simple model was developed and applied to determine the transition's S-parameters. The transition was found to be very efficient over a wide frequency band and a broad range of widths. The characteristic impedance of the strip-ridge structure was found to vary considerably with conductor width, thus allowing some design latitude when matching to a power source.

7.2 Possibilities for Future Work

7.2.1 Further Development of the IEMM Method and Applications to Other Nonplanar Structures

The IEMM method can be improved and its versatility enhanced by increasing efficiency and allowing for the characterization of an expanded class of nonplanar structures.

Based on the discussions in chapters II and III, decreases in run-times can be realized by considering methods to accelerate the convergence of the infinite summations and by improving the algorithms. Specific areas in the formulation which might be addressed include the field normalizations, since a normalization choice might exist which enables the generalized scattering matrices to be computed more swiftly; further optimization of the procedure for determining the transverse eigenvalues; and the expressions for the Green's function matrix (appendix C), which might be written and coded in a form which is more conducive to efficiency. Before the IEMM method can be properly compared to other well-established techniques which are applicable to strip-ridge structures, the fundamental limits of the method's efficiency must be known.

An expanded class of nonplanar structures includes a number of physical effects which were not of primary concern in this work but are of great importance in other selected applications. One such effect, conductor loss, is especially relevant to some of the structures which were characterized in the previous chapters.

Conductor losses are included in the conducting strips by a method which was originally applied in conjunction with a planar integral equation formulation [78]. In this method, the field behavior inside the conducting strip is described by a quasi-TEM analysis which relates the magnetic vector potential to the unknown current distribution by a static Green's function. The resistance and internal inductance per unit length as a function of frequency are then calculated for each strip. These quantities are used to define an equivalent surface impedance which describes in a physically equivalent way the frequency-dependent field penetration in the lossy strips. The tangential electric field on the equivalent strip is related to the total strip current by the surface impedance via

$$\bar{E} \;=\; \hat{n} \times \overline{\overline{Z}}_s \cdot \bar{J} \tag{7.1}$$

where the $\overline{\overline{Z}}_s$ is dyadic surface impedance and $\hat{n}$ is the normal to the conducting strip. The integral equation is written by combining the above equation with equation 2.94 and is again solved with the method of moments.

Conductor losses are also present in the shielding. Losses in the ground plane and the upper wall ($y = 0$ and $y = b$ in figure 2.1) can be taken into account with an impedance boundary condition [78], which is included in the IEMM method by appropriately altering the matrix reflection coefficients of equation 2.67. Losses in the sidewalls ($x = 0$ and $x = a$) are more difficult to model—the mode matching formulation is based on the field orthogonality properties given in equations 2.40–2.43, which require that these walls be perfect conductors. In many cases, the circuits are far away from the sidewalls, and only the ground plane losses are significant.

The IEMM method can be applied to an even broader class of structures by considering additional components of current, anisotropic materials, and coplanar waveguide structures in the presence of arbitrary dielectric support structures. The structures considered in this work included only narrow conducting strips with longitudinal currents. By appropriately modifying the calculation of the primary field mode amplitudes and determining all nine components of the dyadic electric field Green's function, structures which contain arbitrarily oriented, wide conducting strips can be characterized. One strongly anisotropic material is $LiNbO_3$, which is used in electro-optic modulators [33]; when a nonplanar modulator (such as the one in chapter IV) is used, the structure can be analyzed by adapting the IEMM method to account for anisotropic materials. Other structures of interest include the coplanar waveguide analog of strip-ridge structures—i.e., coplanar waveguides in the presence of arbitrary dielectric support structures. To analyze these structures, the electric field integral equation must be replaced with the magnetic field integral equation [20], and the result can be combined with the mode matching method to determine the electric fields in the slots between conductors.

7.2.2 Further Development of Monolithic Dielectric Waveguides

Many possibilities exist for the continued development of the monolithic sub-millimeter-wave and terahertz frequency dielectric waveguides of chapters V and VI. Three areas are identified: expanded study of the propagation characteristics of the waveguides; further examination of the transition between an integrated power source and a waveguide; and fabrication and experimental characterization of monolithic circuits in which the dielectric waveguides are the primary form of transmission line.

The characterization of the electrical performance of the waveguides can be broadened to include the effects of ridge width and height. The ridge width was chosen to be about one-tenth of a guided wavelength at the nominal design frequency, and the layer dimensions were chosen from among a large number of test cases for optimal power confinement in

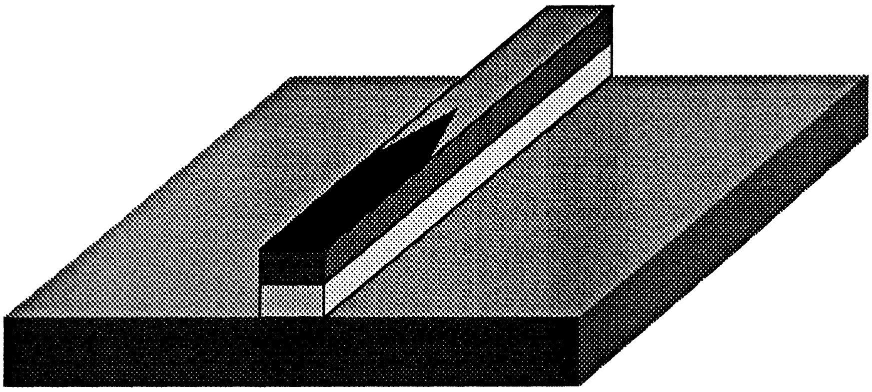

Figure 7.1: Example of a transition with a tapered conductor.

the propagation layer. What are the effects of varying these dimensions? At what width will higher order modes propagate? Does there exist a combination of layer dimensions at which power confinement is improved? If the available materials are specified, can a method be developed which will analytically determine the optimal layer configuration and ridge width?

Both shielded and open (unshielded) transitions are in need of extended study. The future development of a shielded transition might include the use of a lossy damping layer in the cavity to reduce the influence of higher order modes [42]. An open transition requires an alternate analysis technique, such as the generalized integral equation [79]. In both cases, the effects of altering the conductor geometry need to be explored and quantified. What are the effects of adding a taper to the conductor (figure 7.1)? Does an optimal taper exist? Is performance improved by placing the conductor between the top two layers, rather than on top of the ridge? In some instances, the former configuration might be easier to fabricate.

The most important and expansive aspects of the future development of the dielectric waveguide are fabrication and experimental characterization. Some very general fabrication issues were addressed in chapter V, but many other practical considerations and details will arise when the waveguides are actually built. Measurements of the waveguides will begin with scale models, and will become increasingly difficult as the frequency increases. The integration of active devices will evoke a whole new set of concerns centered around maintaining the integrity of the active device while the waveguides are fabricated. The creation of passive circuit elements with the waveguides will also be necessary if the waveguides are to function effectively as monolithic transmission lines.

APPENDICES

APPENDIX A

On the Orthogonality of the Fields

The field orthogonality properties listed in equations 2.40–2.43 are derived from the general reciprocity principle for a source-free waveguide with perfectly conducting walls [15, ch. 6]. The total fields in the structure are linear combinations of plane waves moving in the $\pm\hat{y}$ direction (section 2.4.1). Fields traveling in the $\pm y$ direction which satisfy Maxwell's equations are $\pm\bar{E}^{E\prime}_{tln}$, $\bar{E}^{E\prime}_{yln}$, $\bar{H}^{E\prime}_{tln}$, $\pm\bar{H}^{E\prime}_{yln}$ with eigenvalue $\pm k^{E}_{yln}$ and $\bar{E}^{M\prime}_{tln}$, $\pm\bar{E}^{M\prime}_{yln}$, $\pm\bar{H}^{M\prime}_{tln}$, $\bar{H}^{M\prime}_{yln}$ with eigenvalue $\pm k^{M}_{yln}$. The t indicates fields tangential to the xz-plane and the prime is added to distinguish these fields from the total fields. The reciprocity principle is

$$(k_{yln} + k_{yl'n'}) \int_0^c \int_0^a (\bar{E}'_{tln} \times \bar{H}'_{tl'n'} - \bar{E}'_{tl'n'} \times \bar{H}'_{tln}) \cdot \hat{y}\, dx\, dz \;=\; 0 \qquad \text{(A.1)}$$

For the TE$_x$ fields traveling in the $+\hat{y}$ direction, the above equation is

$$(k^{E}_{yln} + k^{E}_{yl'n'}) \int_0^c \int_0^a \left(\bar{E}^{E\prime}_{tln} \times \bar{H}^{E\prime}_{tl'n'} - \bar{E}^{E\prime}_{tl'n'} \times \bar{H}^{E\prime}_{tln}\right) \cdot \hat{y}\, dx\, dz \;=\; 0 \qquad \text{(A.2)}$$

Replacing $\bar{E}^{E\prime}_{tl'n'}$, $\bar{E}^{E\prime}_{yl'n'}$, $\bar{H}^{E\prime}_{tl'n'}$, $\bar{H}^{E\prime}_{yl'n'}$, $k^{E}_{yl'n'}$ by $-\bar{E}^{E\prime}_{tl'n'}$, $\bar{E}^{E\prime}_{yl'n'}$, $\bar{H}^{E\prime}_{tl'n'}$, $-\bar{H}^{E\prime}_{yl'n'}$, $-k^{E}_{yl'n'}$ in the above equation gives

$$(k^{E}_{yln} - k^{E}_{yl'n'}) \int_0^c \int_0^a \left(\bar{E}^{E\prime}_{tln} \times \bar{H}^{E\prime}_{tl'n'} + \bar{E}^{E\prime}_{tl'n'} \times \bar{H}^{E\prime}_{tln}\right) \cdot \hat{y}\, dx\, dz \;=\; 0 \qquad \text{(A.3)}$$

Combining the previous two equations, assuming $l, n \neq l', n'$ and dividing by $k^{E}_{yln} + k^{E}_{yl'n'}$ gives

$$\int_0^c \int_0^a \bar{E}^{E\prime}_{tln} \times \bar{H}^{E\prime}_{tl'n'} \cdot \hat{y}\, dx\, dz \;=\; 0 \qquad l, n \neq l', n' \qquad \text{(A.4)}$$

Since the total fields consist of linear combinations of the $\pm\hat{y}$-traveling fields, the previous equation can be used to easily derive the total TE$_x$ field orthogonality property:

$$\int_0^c \int_0^a \bar{E}^E_{tln} \times \bar{H}^E_{tl'n'} \cdot \hat{y}\, dx\, dz \;=\; 0 \qquad l,n \neq l',n' \tag{A.5}$$

which is equation 2.40. Similarly, for the TM$_x$ fields,

$$(k^M_{yln} + k^M_{yl'n'}) \int_0^c \int_0^a \left(\bar{E}^{M\prime}_{tln} \times \bar{H}^{M\prime}_{tl'n'} - \bar{E}^{M\prime}_{tl'n'} \times \bar{H}^{M\prime}_{tln} \right) \cdot \hat{y}\, dx\, dz \;=\; 0 \tag{A.6}$$

Replacing $\bar{E}^{M\prime}_{tl'n'}$, $\bar{E}^{M\prime}_{yl'n'}$, $\bar{H}^{M\prime}_{tl'n'}$, $\bar{H}^{M\prime}_{yl'n'}$, $k^M_{yl'n'}$ by $\bar{E}^{M\prime}_{tl'n'}$, $-\bar{E}^{M\prime}_{yl'n'}$, $-\bar{H}^{M\prime}_{tl'n'}$, $\bar{H}^{M\prime}_{yl'n'}$, $-k^M_{yl'n'}$ gives

$$(k^M_{yln} - k^M_{yl'n'}) \int_0^c \int_0^a \left(\bar{E}^{M\prime}_{tln} \times \bar{H}^{M\prime}_{tl'n'} + \bar{E}^{M\prime}_{tl'n'} \times \bar{H}^{M\prime}_{tln} \right) \cdot \hat{y}\, dx\, dz \;=\; 0 \tag{A.7}$$

and the TM$_x$ orthogonality property is

$$\int_0^c \int_0^a \bar{E}^M_{tln} \times \bar{H}^M_{tl'n'} \cdot \hat{y}\, dx\, dz \;=\; 0 \qquad l,n \neq l',n' \tag{A.8}$$

which is equation 2.41.

A general orthogonality relationship like A.5 or A.8 cannot be derived for $\bar{E}^E_{tln}$, $\bar{H}^M_{tln}$ or $\bar{E}^M_{tln}$, $\bar{H}^E_{tln}$; only a limited orthogonality relationship exists between these fields. Using equations 2.14–2.15, 2.16–2.17 and 2.26–2.27, the z-dependencies of the tangential the TE$_x$ and TM$_x$ fields can be shown to vary as $\cos n\pi(z-c)/c$ or $\sin n\pi(z-c)/c$. The TE$_x$ and TM$_x$ fields are thus orthogonal over z, as reflected in equations 2.42–2.43.

APPENDIX B

Elements of the Scattering Matrix

The scattering matrix $S^{(j)}$ for an interface between two sections at $y = b_j$ is defined by either equation 2.51 or 2.52. The elements of $S^{(j)}$ are determined from the interface transmission matrix $T^{(j)}$, which is defined by

$$\begin{bmatrix} L^{(j)-1}C^{(j)} \\ L^{(j)}D^{(j)} \end{bmatrix} = \left[T^{(j)}\right] \begin{bmatrix} C^{(j+1)} \\ D^{(j+1)} + \Lambda^{(j+1)}(b^{(j)} - y')\, C_P^{<(j+1)} \end{bmatrix} \qquad b_j < y' \tag{B.1}$$

$$\begin{bmatrix} C^{(j)} + \Lambda^{(j)-1}(b^{(j)} - y')\, C_P^{>(j)} \\ D^{(j)} \end{bmatrix} = \left[T^{(j)}\right] \begin{bmatrix} L^{(j+1)}C^{(j+1)} \\ L^{(j+1)-1}D^{(j+1)} \end{bmatrix} \qquad b_j > y' \tag{B.2}$$

The elements of $T^{(j)}$ for $b_j > y'$ are given by

$$\left[T^{(j)}\right] = \begin{bmatrix} T_{11} & T_{12} \\ T_{21} & T_{22} \end{bmatrix} = \frac{1}{2} \begin{bmatrix} \mathcal{T}_1 + \mathcal{T}_2 & \mathcal{T}_1 - \mathcal{T}_2 \\ \mathcal{T}_1 - \mathcal{T}_2 & \mathcal{T}_1 + \mathcal{T}_2 \end{bmatrix} \tag{B.3}$$

where

$$[\mathcal{T}_1] = \begin{bmatrix} T_2^M & 0 \\ T_3^{ME} & T_1^E \end{bmatrix} \tag{B.4}$$

$$[\mathcal{T}_2] = \begin{bmatrix} T_1^M & T_3^{EM} \\ 0 & T_2^E \end{bmatrix} \tag{B.5}$$

and

$$T_1^M = \frac{N_{l'n}^{(j)M}}{N_{ln}^{(j+1)M}} K_x^M(l,l') I_1^M(l,l') \tag{B.6}$$

$$T_2^M = \frac{N_{l'n}^{(j)M}}{N_{ln}^{(j+1)M}} K_y^M(ln,l'n) I_2^M(l,l') \tag{B.7}$$

$$T_3^{EM} = \frac{I_{zn}^{EM}\, N_{l'n}^{(j)M}}{k_{yl'n}^{(j)M}\, N_{ln}^{(j+1)E}} \left(I_3^{EM}(l,l') - \sum_{l''} K_x^E(l,l'') I_4^{EM}(l'',l') I_1^E(l,l'') \right) \tag{B.8}$$

$$T_1^E = \frac{N_{l'n}^{(j)E}}{N_{ln}^{(j+1)E}} K_x^E(l,l') I_1^E(l,l') \tag{B.9}$$

$$T_2^E = \frac{N_{l'n}^{(j)E}}{N_{ln}^{(j+1)E}} K_y^E(ln,l'n) I_2^E(l,l') \tag{B.10}$$

$$T_3^{ME} = -\frac{I_{zn}^{ME}\, N_{l'n}^{(j)E}}{k_{yl'n}^{(j)E}\, N_{ln}^{(j+1)M}} \left(I_3^{ME}(l,l') - \sum_{l''} K_y^M(l,l'') I_4^{ME}(l'',l') I_1^M(l,l'') \right) \tag{B.11}$$

In the above set of equations,

$$I_1^E(l,l') = \frac{1}{I_0^E(l')} \int_0^a \frac{X_l^{(i,j+1)E}(x)\, X_{l'}^{(ij)E}(x)}{\epsilon^{(ij)} \epsilon^{(i,j+1)} \mu^{(i,j+1)}}\, dx \tag{B.12}$$

$$I_2^E(l,l') = \frac{1}{I_0^E(l')} \int_0^a \frac{X_{l'}^{(ij)E}(x)\, X_l^{(i,j+1)E}(x)}{\epsilon^{(ij)} \epsilon^{(i,j+1)} \mu^{(ij)}}\, dx \tag{B.13}$$

$$I_3^{ME}(l,l') = \frac{1}{I_0^E(l')} \int_0^a \frac{1}{j\omega \epsilon^{(ij)} \mu^{(ij)} \epsilon^{(i,j+1)} \mu^{(i,j+1)}} \frac{dX_l^{(i,j+1)M}}{dx} X_{l'}^{(ij)E}(x)\, dx \tag{B.14}$$

$$I_4^{ME}(l,l') = \frac{1}{I_0^E(l')} \int_0^a \frac{1}{j\omega (\epsilon^{(ij)} \mu^{(ij)})^2} \frac{dX_l^{(ij)M}}{dx} X_{l'}^{(ij)E}(x)\, dx \tag{B.15}$$

$$I_1^M(l,l') = \frac{1}{I_0^M(l')} \int_0^a \frac{X_l^{(i,j+1)M}(x)\, X_{l'}^{(ij)M}(x)}{\epsilon^{(i,j+1)} \mu^{(ij)} \mu^{(i,j+1)}}\, dx \tag{B.16}$$

$$I_2^M(l,l') = \frac{1}{I_0^M(l')} \int_0^a \frac{X_{l'}^{(ij)M}(x)\, X_l^{(i,j+1)M}(x)}{\epsilon^{(ij)} \mu^{(ij)} \mu^{(i,j+1)}}\, dx \tag{B.17}$$

$$I_3^{EM}(l,l') = \frac{1}{I_0^M(l')} \int_0^a \frac{1}{j\omega \epsilon^{(ij)} \mu^{(ij)} \epsilon^{(i,j+1)} \mu^{(i,j+1)}} \frac{dX_l^{(i,j+1)E}}{dx} X_{l'}^{(ij)M}(x)\, dx \tag{B.18}$$

$$I_4^{EM}(l,l') = \frac{1}{I_0^M(l')} \int_0^a \frac{1}{j\omega (\epsilon^{(ij)} \mu^{(ij)})^2} \frac{dX_l^{(ij)E}}{dx} X_{l'}^{(ij)M}(x)\, dx \tag{B.19}$$

$$I_{zn}^{EM} = \frac{\int_0^c \frac{dZ_n^E}{dz} Z_n^M(z)\, dz}{\int_0^c (Z_n^M(z))^2\, dz} = -k_{zn} \tag{B.20}$$

$$I_{zn}^{ME} = \frac{\int_0^c \frac{dZ_n^M}{dz} Z_n^E(z)\, dz}{\int_0^c (Z_n^E(z))^2\, dz} = k_{zn} \tag{B.21}$$

where

$$I_0^E(l') = \int_0^a \frac{(X_{l'}^{(ij)E}(x))^2}{(\epsilon^{(ij)})^2\mu^{(ij)}}\,dx \tag{B.22}$$

$$I_0^M(l') = \int_0^a \frac{(X_{l'}^{(ij)M}(x))^2}{\epsilon^{(ij)}(\mu^{(ij)})^2}\,dx \tag{B.23}$$

and the factors K_x^E, K_x^M, K_y^E and K_y^M are

$$K_x^E(l,l') = \frac{(k^{(i,j+1)})^2 - (k_{xl}^{(i,j+1)E})^2}{(k^{(ij)})^2 - (k_{xl'}^{(ij)E})^2} \tag{B.24}$$

$$K_x^M(l,l') = \frac{(k^{(i,j+1)})^2 - (k_{xl}^{(i,j+1)M})^2}{(k^{(ij)})^2 - (k_{xl'}^{(ij)M})^2} \tag{B.25}$$

$$K_y^E(ln,l'n) = \frac{k_{yln}^{(j+1)E}}{k_{yl'n}^{(j)E}} \tag{B.26}$$

$$K_y^M(ln,l'n) = \frac{k_{yln}^{(j+1)M}}{k_{yl'n}^{(j)M}} \tag{B.27}$$

All other relevant quantities are defined in chapter II.

The elements of the transmission matrix for $b_j < y'$ are determined from the above equations by replacing the section index $j+1$ by $j-1$.

The scattering matrix is partitioned as

$$[S] = \begin{bmatrix} S_{11} & S_{12} \\ S_{21} & S_{22} \end{bmatrix} \tag{B.28}$$

and the elements of the scattering matrix are obtained from the transmission matrix elements using the well-known relations

$$S_{21} = T_{11}^{-1} \tag{B.29}$$

$$S_{11} = T_{21}T_{11}^{-1} \tag{B.30}$$

$$S_{22} = -T_{11}^{-1}T_{12} \tag{B.31}$$

$$S_{12} = T_{22} - T_{21}T_{11}^{-1}T_{12} \tag{B.32}$$

APPENDIX C

Expression for the Green's Function

The Green's function is determined by the vectors $U_{\nu 1}^{(j)}(x,y,z)$ and $U_2^{(j)}(x',y',z')$ and by the matrix $R^{(j)}$, where $\nu = x,y,z$ (equation 2.74). For $\nu = x,z$, the vector $U_{\nu 1}^{(j)}(x,y,z)$ is

$$U_{\nu 1}^{(j)}(x,y,z) \;=\; \begin{bmatrix} \Lambda^{(j)}(d^{\lessgtr(j)-1}(y))\;\; U_\nu^{(j)}(x,z) \\ \Lambda^{(j)}(d^{\lessgtr(j)-1}(y))\;\; U_\nu^{(j)}(x,z) \\ \Lambda^{(j)}(d^{\lessgtr(j)}(y))\;\; U_\nu^{(j)}(x,z) \\ \Lambda^{(j)}(d^{\lessgtr(j)}(y))\;\; U_\nu^{(j)}(x,z) \end{bmatrix} \qquad y \lessgtr y' \tag{C.1}$$

and for $\nu = y$

$$U_{\nu 1}^{(j)}(x,y,z) \;=\; \begin{bmatrix} \Lambda^{(j)}(d^{\lessgtr(j)-1}(y))\;\; U_\nu^{(j)}(x,z) \\ \Lambda^{(j)}(d^{\lessgtr(j)-1}(y))\;\; U_\nu^{(j)}(x,z) \\ -\Lambda^{(j)}(d^{\lessgtr(j)}(y))\;\; U_\nu^{(j)}(x,z) \\ -\Lambda^{(j)}(d^{\lessgtr(j)}(y))\;\; U_\nu^{(j)}(x,z) \end{bmatrix} \qquad y \lessgtr y' \tag{C.2}$$

where the ln^{th} element of the vector $U_\nu^{(j)}(x,z)$ is

$$U_{x(ln)}^{(j)}(x,z) \;=\; \begin{cases} \dfrac{-j\omega}{\left(k^{(ij)}\right)^2} \left(\left(k^{(ij)}\right)^2 - \left(k_{xl}^{(ij)M}\right)^2 \right) X_l^{(ij)M}(x)\, Z_n^M(z) \\ \qquad\qquad\qquad \text{if } ln \text{ denotes a TM}_x \text{ mode} \\[2ex] 0 \\ \qquad\qquad\qquad \text{if } ln \text{ denotes a TE}_x \text{ mode} \end{cases} \tag{C.3}$$

$$U^{(j)}_{y(ln)}(x,z) = \begin{cases} \dfrac{\omega k^{(j)M}_{yln}}{\left(k^{(ij)}\right)^2} \dfrac{dX^{(ij)M}_l}{dx} Z^M_n(z) & \text{if } ln \text{ denotes a TM}_x \text{ mode} \\ \\ \dfrac{1}{\epsilon^{(ij)}} X^{(ij)E}_l(x) \dfrac{dZ^E_n}{dz} & \text{if } ln \text{ denotes a TE}_x \text{ mode} \end{cases} \tag{C.4}$$

$$U^{(j)}_{z(ln)}(x,z) = \begin{cases} \dfrac{-j\omega}{\left(k^{(ij)}\right)^2} \dfrac{dX^{(ij)M}_l}{dx} \dfrac{dZ^M_n}{dz} & \text{if } ln \text{ denotes a TM}_x \text{ mode} \\ \\ \dfrac{-jk^{(j)E}_{yln}}{\epsilon^{(ij)}} X^{(ij)E}_l(x)\, Z^E_n(z) & \text{if } ln \text{ denotes a TE}_x \text{ mode} \end{cases} \tag{C.5}$$

and $d^{<(j)}(y) = b^{(j-1)} - y$ and $d^{>(j)}(y) = y - b^{(j)}$. The vector $U^{(j)}_2(x',y',z')$ is

$$U^{(j)}_2(x',y',z') = \begin{bmatrix} \Lambda^{(j)}(d^{\lessgtr(j)}(y'))\ C^{\lessgtr(j)}_P(x',z') \\ \Lambda^{(j)}(d^{\gtrless(j)}(y'))\ C^{\lessgtr(j)}_P(x',z') \\ \Lambda^{(j)}(d^{\lessgtr(j)}(y'))\ C^{\lessgtr(j)}_P(x',z') \\ \Lambda^{(j)}(d^{\gtrless(j)}(y'))\ C^{\lessgtr(j)}_P(x',z') \end{bmatrix} \qquad y \lessgtr y' \tag{C.6}$$

The matrix $R^{(j)}$ is written in terms of the matrices R_1 and R_2, which are defined by writing equations 2.72–2.73 as

$$C^{>(j)} = \left(R^{\gtrless(j)}_1 \Lambda^{(j)}(y' - b^{(j)}) + R^{\gtrless(j)}_2 \Lambda^{(j)}(b^{(j-1)} - y')\right) C^{\lessgtr(j)}_P \tag{C.7}$$

$$D^{<(j)} = \left(R^{\lessgtr(j)}_1 \Lambda^{(j)}(b^{(j-1)} - y') + R^{\lessgtr(j)}_2 \Lambda^{(j)}(y' - b^{(j)})\right) C^{\gtrless(j)}_P \tag{C.8}$$

where

$$R^{\lessgtr(j)}_1 = \left(I - L^{(j)-1}\Gamma^{\gtrless(j)}L^{(j)-1}\Gamma^{\lessgtr(j)}\right)^{-1} L^{(j)-1}\Gamma^{\gtrless(j)}L^{(j)-1}\Gamma^{\lessgtr(j)} \tag{C.9}$$

$$R^{\lessgtr(j)}_2 = \left(I - L^{(j)-1}\Gamma^{\gtrless(j)}L^{(j)-1}\Gamma^{\lessgtr(j)}\right)^{-1} L^{(j)-1}\Gamma^{\gtrless(j)} \tag{C.10}$$

With this notation, the matrix $R^{(j)}$ is

$$R^{(j)} = \begin{bmatrix} I + R_1^{\lessgtr(j)} & 0 & 0 & 0 \\ 0 & R_2^{\lessgtr(j)} & 0 & 0 \\ 0 & 0 & \Gamma^{\lessgtr(j)}\left(I + R_1^{\lessgtr(j)}\right) & 0 \\ 0 & 0 & 0 & \Gamma^{\lessgtr(j)} R_2^{\lessgtr(j)} \end{bmatrix} \quad y \lessgtr y' \tag{C.11}$$

APPENDIX D

Differences between the Two- and Three-dimensional IEMM Formulations

The Fourier transform of section 2.6.1 causes the two- and three-dimensional derivations of the Green's function to differ as follows:

1. The transformed expressions for $\tilde{f}$ and $\tilde{a}$ (equations 2.16–2.17) do not include any z or n dependencies.

2. The transformed orthogonality relations (equations 2.40–2.43) do not involve z-integrals so that

$$N_{zn}^{E}, N_{zn}^{M}, N_{zn}^{EM}, N_{zn}^{ME} \longrightarrow 1 \tag{D.1}$$

   and the integrals I_{zn}, I_{zn}^{EM} and I_{zn}^{EM} (in equations 2.60–2.62 and appendix B) are transformed by

$$I_{zn} \longrightarrow 1 \tag{D.2}$$

$$I_{zn}^{EM}, I_{zn}^{ME} \longrightarrow -jk_z \tag{D.3}$$

3. The current source is transformed from a point source to a line source. The boundary condition for H_x (equation 2.57) is transformed by

$$\begin{aligned} H_x^{>} - H_x^{<} &= -\delta(x-x')\delta(z-z') \longrightarrow \\ \tilde{H}_x^{>} - \tilde{H}_x^{<} &= -\delta(x-x')e^{jk_z z'} \end{aligned} \tag{D.4}$$

so that the quantity $Z_n^E(z')$ in the expression for the TE$_x$ primary field mode amplitudes (equation 2.60) is replaced as

$$Z_n^E(z') \longrightarrow e^{jk_z z'} \tag{D.5}$$

4. The quantities $Z_n(z)$ and $\frac{dZ_n}{dz}$ in the vector $U_\nu^{(j)}$ in appendix C (equation C.5) are transformed by

$$Z_n(z) \longrightarrow 1 \tag{D.6}$$

$$\frac{dZ_n}{dz} \longrightarrow -jk_z \tag{D.7}$$

By combining the transformed versions of equation 2.14, sections 2.4.1–2.4.5, and appendices B–C, the transformed Green's function can be expressed as

$$\tilde{\overline{\overline{G}}}_E(x, y, k_z; x', y', z') = \tilde{\overline{\overline{g}}}_E(x, y, k_z; x', y')e^{jk_z z'} \tag{D.8}$$

BIBLIOGRAPHY

BIBLIOGRAPHY

[1] S. Adachi, "GaAs, AlAs, $Al_xGa_{1-x}As$: material parameters for use in research and device applications," *J. Appl. Phys.*, vol. 58, pp. R1–R29, 1 Aug. 1985.

[2] M. N. Afsar and K. J. Button, "Precise millimeter-wave measurements of complex refractive index, complex dielectric permittivity and loss tangent of GaAs, Si, SiO_2, Al_2O_3, BeO, macor, and glass," *IEEE Trans. Microwave Theory Tech.*, vol. MTT-31, pp. 217–223, Feb. 1983.

[3] R. C. Alferness, S. K. Korotky and A. J. Marcatili, "Velocity-matching techniques for integrated optic traveling wave switch/modulators," *IEEE J. of Quantum Elec.*, vol. QE-20, pp. 301–309, Mar. 1984.

[4] A. Asi and L. Shafai, "Dispersion analysis of anisotropic inhomogeneous waveguides using compact 2D-FDTD," *Elect. Lett.*, vol. 28, 16 July 1992.

[5] J. S. Bagby, C. Lee, Y. Yuan and D. P. Nyquist, "Entire-domain basis MOM analysis of coupled microstrip transmission lines," *IEEE Trans. Microwave Theory Tech.*, vol. MTT-40, pp. 49–57, Jan. 1992.

[6] C. A. Balanis, *Advanced Engineering Electromagnetics.* New York: John Wiley & Sons, 1989, ch. 8.

[7] R. A. Bell, "IBM RISC System/6000 performance tuning for numerically intensive Fortran and C programs," IBM ITSC Technical Bulletin GG24-3611, Oct. 1990.

[8] K. Bierwirth, N. Schulz, and F. Arndt, "Finite-difference analysis of rectangular dielectric waveguide structures," *IEEE Trans. Microwave Theory Tech.*, vol. MTT-34, pp. 1104–1114, Nov. 1986.

[9] J. Bornemann and R. Vahldieck, "Characterization of a class of waveguide discontinuities using a modified TM^x_{mn} mode approach," *IEEE Trans. Microwave Theory Tech.*, vol. MTT-38, pp. 1816–1822, Dec. 1990.

[10] J. Bornemann and F. Arndt, "Modal S-matrix design of optimum stepped ridged and finned waveguide transformers," *IEEE Trans. Microwave Theory Tech.*, vol. MTT-35, pp. 561–567, Jun. 1987.

[11] J. R. Brews, "Characteristic impedance of microstrip lines," *IEEE Trans. Microwave Theory Tech.*, vol. MTT-35, pp. 30–34, Jan. 1987.

[12] L. Carin and K. J. Webb, "Characteristic impedance of multilevel, multiconductor hybrid mode microstrip," *IEEE Trans. Magn.*, vol. 25, pp. 2947–2949, Jul. 1988.

[13] L. Carin and K. J. Webb, "An equivalent circuit model for terminated hybrid-mode multiconductor transmission lines," *IEEE Trans. Microwave Theory Tech.*, vol. MTT-37, pp. 1784–1793, Nov. 1989.

[14] D. H. Choi and W. J. R. Hoefer, "The finite-difference–time-domain method and its application to eigenvalue problems," *IEEE Trans. Microwave Theory Tech.*, vol. MTT-34, pp. 1464–1470, Dec. 1986.

[15] R. E. Collin, *Field Theory of Guided Waves.* New York: IEEE Press, 1991.

[16] —, *Foundations for Microwave Engineering.* New York: McGraw-Hill, Inc., 1966, ch. 4.

[17] U. Crombach, "Analysis of single and coupled rectangular dielectric wave-guides," *IEEE Trans. Microwave Theory Tech.*, vol. MTT-29, pp. 870–874, Sept. 1981.

[18] G. Dahlquist and A. Björck, and translated by N. Anderson, *Numerical Methods.* Englewood Cliffs, NJ: Prentice-Hall, Inc., 1974, ch. 5.

[19] N. K. Das and D. M. Pozar, "A generalized spectral-domain green's function for multilayer dielectric substrates with application to multilayer transmission lines," *IEEE Trans. Microwave Theory Tech.*, vol. MTT-35, pp. 326–335, Mar. 1987.

[20] N. I. Dib and P. B. Katehi, "Modeling of shielded CPW discontinuities using the space domain integral equation method (SDIE)," *J. of Electromagnetic Waves and Applications*, vol. 5, pp. 503–523, Apr. 1991.

[21] N. I. Dib, personal communication, 20 Dec. 1992.

[22] L. P. Dunleavy, "Discontinuity Characterization in Shielded Microstrip: A Theoretical and Experimental Study." Ph.D. Dissertation, The University of Michigan, Ann Arbor MI, 1988.

[23] G. V. Eleftheriades, W. Y. Ali-Ahmad, L. P. B. Katehi and G. M. Rebeiz, "Millimeter-wave integrated-horn antennas: part I—theory," *IEEE Trans. Antennas Propagat.*, vol. AP-39, pp. 1575–1581, Nov. 1991.

[24] G. V. Eleftheriades, "Analysis and design of integrated-circuit horn antennas for millimeter and sub-millimeter applications." Ph.D. Dissertation, The University of Michigan, 1993.

[25] A. G. Engel, Jr., and L. P. B. Katehi, "Analysis of microstrip structures on and near dielectric ridges using an integral equation-mode matching technique," *1991 IEEE MTT-S Intl. Microwave Symp. Dig.*, vol. 1, pp. 135–138, 1991.

[26] —, "Low-loss monolithic transmission lines for submillimeter and terahertz frequency applications," *IEEE Trans. Microwave Theory Tech.*, vol. MTT-39, pp. 1847–1854, Nov. 1991.

[27] —, "On the analysis of a transition to a layered ridged dielectric waveguide," *1992 IEEE MTT-S Intl. Microwave Symp. Dig.*, vol. 2, pp. 983–986, 1992.

[28] —, "Frequency and Time Domain Characterization of Microstrip-Ridge Structures," Accepted for publication by *IEEE Trans. Microwave Theory Tech.*, 1993.

[29] F. E. Gardiol, "Higher-order modes in dielectrically loaded rectangular waveguides," *IEEE Trans. Microwave Theory Tech.*, vol. MTT-16, pp. 919–924, Nov. 1968.

[30] W. J. Getsinger, "Measurement and modeling of the apparent characteristic impedance of microstrip," *IEEE Trans. Microwave Theory Tech.*, vol. MTT-31, pp. 624–632, Aug. 1983.

[31] J. P. Gilb and C. A. Balanis, "Pulse distortion on multilayer coupled microstrip lines," *IEEE Trans. Microwave Theory Tech.*, vol. MTT-37, pp. 1620–1628, Oct. 1989.

[32] K. C. Gupta, R. Garg, and I. J. Bahl, *Microstrip Lines and Slotlines.* Dedham MA: Artech House, Inc., 1979, ch. 8.

[33] H. Haga, M. Izutsu and T. Sueta, "$LiNbO_3$ traveling-wave light modulator/switch with an etched groove," *IEEE J. of Quantum Elec.*, vol. QE-22, pp. 902–906, June 1986.

[34] L. J. Harding, "Numerical Analysis and Applications Software Abstracts," Computing Center Memo 407, The University of Michigan Computing Center, ch. 9, Sept. 1979.

[35] R. F. Harrington, *Time-Harmonic Electromagnetic Fields.* New York: McGraw-Hill, Inc., 1961, ch. 4.

[36] H. Hasegawa, M. Furukawa and H. Yanai, "Properties of microstrip line on Si-SiO_2 system," *IEEE Trans. Microwave Theory Tech.*, vol. MTT-19, pp. 367–379, Nov. 1971.

[37] H. Haskal, "Matrix description of waveguide discontinuities in the presence of evanescent modes," *IEEE Trans. Microwave Theory Tech.*, vol. MTT-12, pp. 184–188, Mar. 1964.

[38] W. Heinrich and H.L. Hartnagel, "Wave propagation on MESFET electrodes and its influence on transistor gain," *IEEE Trans. Microwave Theory Tech.*, vol. MTT-35, pp. 1–8, Jan. 1987.

[39] W. J. R. Hoefer, "The transmission-line matrix method—theory and applications," *IEEE Trans. Microwave Theory Tech.*, vol. MTT-33, pp. 882–893, Oct. 1985.

[40] T. Itoh, "Inverted strip dielectric waveguide for millimeter-wave integrated circuits," *IEEE Trans. Microwave Theory Tech.*, vol. MTT-24, pp. 821–827, Nov. 1980.

[41] T. Itoh and B. Adelseck, "Trapped image guide for millimeter-wave circuits," *IEEE Trans. Microwave Theory Tech.*, vol. MTT-28, pp. 1433–1436, Dec. 1980.

[42] R. W. Jackson, "Removing package effects from microstrip moment method calculations," *1992 IEEE MTT-S Intl. Microwave Symp. Dig.*, vol. 3, pp. 1225–1228, 1992.

[43] P. B. Katehi and N. G. Alexopoulos, "Frequency-dependent characteristics of microstrip discontinuities in millimeter-wave integrated circuits," *IEEE Trans. Microwave Theory Tech.*, vol. MTT-33, pp. 1029–1035, Oct. 1985.

[44] M. Kirschning and R. H. Jansen, "Accurate wide-range design equations for the frequency-dependent characteristics of parallel coupled microstrip lines," *IEEE Trans. Microwave Theory Tech.*, vol. MTT-32, pp. 83–90, Jan. 1984.

[45] T. G. Livernois and P. B. Katehi, "A generalized method for deriving the space-domain Green's function in a shielded, multilayer substrate structure with applications to MIS slow-wave transmission lines," *IEEE Trans. Microwave Theory Tech.*, vol. MTT-37, pp. 1761–1767, Nov. 1989.

[46] —, "Characteristic impedance and electromagnetic field distribution in metal-insulator-semiconductor microstrip," *IEEE Trans. Microwave Theory Tech.*, vol. MTT-38, pp. 1740–1743, Nov. 1990.

[47] R. R. Mansour and R. H. MacPhie, "Scattering at an n-furcated parallel-plate waveguide-junction," *IEEE Trans. Microwave Theory Tech.*, vol. MTT-33, pp. 830–835, Sept. 1985.

[48] —, "An improved transmission matrix formulation of cascaded discontinuities and its application to E-plane circuits," *IEEE Trans. Microwave Theory Tech.*, vol. MTT-34, pp. 1490–1498, Dec. 1986.

[49] S. L. Marple, *Digital Spectral Analysis with Applications.* Englewood Cliffs NJ: Prentice-Hall, Inc., 1987.

[50] W. V. McLevige, R. Mittra, and T. Itoh, "New waveguide structures for millimeter-wave and optical integrated circuits," *IEEE Trans. Microwave Theory Tech.*, vol. MTT-23, pp. 788–794, Oct. 1975.

[51] J. Meixner, "The behaviour of electromagnetic fields at edges," *IEEE Trans. Antennas Propagat.*, vol. AP-20, pp. 442–446, July 1972.

[52] R. Mittra, Y. Hou and V. Jamnejad, "Analysis of open dielectric waveguides using mode-matching techniques and variational methods," *IEEE Trans. Microwave Theory Tech.*, vol. MTT-28, pp. 36–43, Jan. 1980.

[53] K. Ogusu, "Numerical analysis of the rectangular dielectric waveguide and its modifications," *IEEE Trans. Microwave Theory Tech.*, vol. MTT-25, pp. 874–885, Nov. 1977.

[54] A. A. Oliner and S. Peng, "Guidance and leakage properties of a class of open dielectric waveguides: part II—new physical effects," *IEEE Trans. Microwave Theory Tech.*, vol. MTT-29, pp. 855–869, Sept. 1981.

[55] A. S. Omar and K. Schünemann, "Transmission matrix representation of finline discontinuities," *IEEE Trans. Microwave Theory Tech.*, vol. MTT-33, pp. 765–770, Sept. 1985.

[56] —, "Complex and backward-wave modes in inhomogeneously and anisotropically filled waveguides," *IEEE Trans. Microwave Theory Tech.*, vol. MTT-35, pp. 268–275, Mar. 1987.

[57] P. H. Pathak, "On the eigenfunction expansion of electromagnetic dyadic Green's functions," *IEEE Trans. Antennas Propagat.*, vol. AP-31, pp. 837–846, Nov. 1983.

[58] H. Patzelt and F. Arndt, "Double-plane steps in rectangular waveguides and their application in for transformers, irises, and filters," *IEEE Trans. Microwave Theory Tech.*, vol. MTT-30, pp. 771–776, May 1982.

[59] S. Peng and A. A. Oliner, "Guidance and leakage properties of a class of open dielectric waveguides: part I—mathematical formulations," *IEEE Trans. Microwave Theory Tech.*, vol. MTT-29, pp. 843–855, Sept. 1981.

[60] W. H. Press, B. P. Flannery, S. A. Teukolsky and W. T. Vetterling, *Numerical Recipes.* Cambridge: Cambridge University Press, 1986.

[61] B. M. A. Rahman, F. A, Fernandez and J. B. Davies, "Review of finite element methods for microwave and optical waveguides," *Proc. IEEE*, vol. 79, pp. 1442–1448, Oct. 1991.

[62] P. A. Rizzi, *Microwave Engineering.* Englewood Cliffs NJ: Prentice-Hall, Inc., 1988, ch. 8.

[63] R. Safavi-Naini and R. H. MacPhie, "On solving waveguide junction scattering problems by the conservation of complex power technique," *IEEE Trans. Microwave Theory Tech.*, vol. MTT-29, pp. 337–343, Apr. 1981.

[64] —, "Scattering at rectangular-to-rectangular waveguide junctions," *IEEE Trans. Microwave Theory Tech.*, vol. MTT-30, pp. 2060–2063, Nov. 1982.

[65] W. Schroeder and I. Wolff, "A new hybrid mode boundary integral method for analysis of MMIC waveguides with complicated crossection," *1989 IEEE MTT-S Intl. Microwave Symp. Dig.*, vol. 2, pp. 711–714, 1989.

[66] C. E. Smith and R. Chang, "Microstrip transmission line with finite-width dielectric," *IEEE Trans. Microwave Theory Tech.*, vol. MTT-28, pp. 90–94, Feb. 1980.

[67] —, "Microstrip transmission line with finite-width dielectric and ground plane," *IEEE Trans. Microwave Theory Tech.*, vol. MTT-33, pp. 835–839, Sept. 1985.

[68] K. Solbach and I. Wolff, "The electromagnetic fields and the phase constants of dielectric image lines," *IEEE Trans. Microwave Theory Tech.*, vol. MTT-26, pp. 266–274, Apr. 1978.

[69] W. L. Stutzman and G. A. Thiele, *Antenna Theory and Design.* New York: John Wiley & Sons, Inc., 1981, ch. 7.

[70] T. Sueta and M. Izutsu, "Integrated optic devices for microwave applications," *IEEE Trans. Microwave Theory Tech.*, vol. MTT-38, pp. 477–482, May 1990.

[71] C. T. Tai, *Generalized Vector and Dyadic Analysis.* New York: IEEE Press, 1992, p. 104.

[72] —, "Equivalent layers of surface charge, current sheet, and polarization in the eigenfunction expansions of Green's functions in electromagnetic theory," *IEEE Trans. Antennas Propagat.*, vol. AP-29, pp. 733–739, Sep. 1981.

[73] *Symposium Proceedings, Third Intl. Symp. on Space Terahertz Tech.,* Univ. of Michigan, Ann Arbor MI, 1992.

[74] M. Thorburn, A. Agoston, and V. K. Tripathi, "Computation of frequency-dependent propagation characteristics of microstriplike propagation structures with discontinuous layers," *IEEE Trans. Microwave Theory Tech.*, vol. MTT-38, pp. 148–153, Feb. 1990.

[75] C. C. Tzuang and J.-D. Tseng, "A full-wave mixed potential mode-matching method for the analysis of planar or quasi-planar transmission lines," *IEEE Trans. Microwave Theory Tech.*, vol. MTT-39, pp. 1701–1711, Oct. 1987.

[76] F. T. Ulaby, ed., "Special issue on terahertz technology," *Proc. IEEE*, vol. 80, Nov. 1992.

[77] N. L. VandenBerg, "Full-wave analysis of microstrip-fed slot antennas and couplers." Ph.D. Dissertation, The University of Michigan, 1991.

[78] T. E. van Deventer, P. B. Katehi, and A. Cangellaris, "An integral equation method for the evaluation of conductor and dielectric losses in high frequency interconnects," *IEEE Trans. Microwave Theory Tech.*, vol. MTT-37, pp. 1964–1972, Dec. 1989.

[79] T. E. van Deventer and L. P. B. Katehi, "A study of sub-millimeter wave coupled dielectric waveguides using the GIE method," *1992 IEEE MTT-S Intl. Microwave Symp. Dig.*, vol. 3, pp. 1115–1118, 1992.

[80] A. T. Villeneuve, "Equivalent circuits of junctions of slab-loaded rectangular waveguides," *IEEE Trans. Microwave Theory Tech.*, vol. MTT-33, pp. 1196–1203, Nov. 1985.

[81] J. J. H. Wang, *Generalized Moment Methods in Electromagnetics.* New York: John Wiley & Sons, Inc., 1991, p. 91–2.

[82] S. Y. Wang and S. H. Lin, "High speed III-V electrooptic waveguide modulators at $\lambda = 1.3\mu m$," *J. of Lightwave Tech.*, vol. 6, pp. 758–771, June 1988.

[83] T. Wang and S. E. Schwarz, "Design of dielectric ridge waveguides for millimeter-wave integrated circuits," *IEEE Trans. Microwave Theory Tech.*, vol. MTT-31, pp. 128–134, Feb. 1983.

[84] W. Wertgen and R. H. Jansen, "Efficient direct and iterative electrodynamic analysis of geometrically complex MIC and MMIC structures," *Int. J. of Numerical Modelling: Electronic Networks, Devices and Fields*, vol. 2, pp. 153–186, 1989.

[85] A. Wexler, "Solution of waveguide discontinuities by modal analysis," *IEEE Trans. Microwave Theory Tech.*, vol. MTT-15, pp. 508–517, Sept. 1967.

[86] L. Wiemer and R. H. Jansen, "Reciprocity related definition of strip characteristic impedance for multiconductor hybrid-mode transmission lines," *Microwave and Opt. Tech. Letters*, vol. 1, pp. 22–25, Mar. 1988.

[87] K. Wu and R. Vahldieck, "Comprehensive MoL analysis of a class of semiconductor-based transmission lines suitable for microwave and optoelectronic application," *Intl. J. of Numerical Modelling: Electronic Networks, Devices and Fields*, vol. 4, pp. 45–62, 1991.

[88] E. Yamashita and K. Atsuki, "Analysis of microstrip-like transmission lines by nonuniform discretization of integral equations," *IEEE Trans. Microwave Theory Tech.*, vol. MTT-24, pp. 195–200, Apr. 1976.

[89] E. Yamashita, K. R. Li, and Y. Suzuki, "Characterization method and simple design formulas of MCS lines proposed for MMIC's," *IEEE Trans. Microwave Theory Tech.*, vol. MTT-35, pp. 1355–1362, Dec. 1987.

[90] E. Yamashita, H. Ohashi, and K. Atsuki, "Characterization of microstrip lines near a substrate edge and design formulas of edge-compensated microstrip lines," *IEEE Trans. Microwave Theory Tech.*, vol. MTT-37, pp. 890–896, May 1989.

[91] B. Young and T. Itoh, "Analysis and design of microslab waveguide," *IEEE Trans. Microwave Theory Tech.*, vol. MTT-35, pp. 850–857, Sept. 1987.

[92] —, "Analysis of coupled Microslab$^{\mathrm{TM}}$ lines," *IEEE Trans. Microwave Theory Tech.*, vol. MTT-36, pp. 616–619, Mar. 1988.

[93] G. W. Zheng and K. S. Chen, "Effects of substrate anisotropy on the dispersion of transient signals in microstrip lines," *Intl. J. of Infrared and Millimeter Waves*, vol. 11, no. 4, pp. 489–498, 1990.